PhD degree in Systems Medicine (curriculum in Molecular Oncology)

European School of Molecular Medicine (SEMM),

University of Milan and University of Naples “Federico II”

Cellular and molecular mechanisms of chemo-resistance in Acute Myeloid Leukemia

Settore disciplinare: MED/04

Simone Frascolla

Tutor: Prof. Pier Giuseppe Pelicci, MD, PhD

European Institute of Oncology (IEO), Milan

PhD Coordinator: Prof. Diego Pasini

Anno accademico 2023-2024

Table of Contents

LIST OF ABBREVIATIONS

AML	Acute Myeloid Leukemia
AML9	Acute Myeloid Leukemia model 9
AMLIEO20	Acute Myeloid Leukemia model IEO20
AraC	Cytarabine arabinoside
BCL-2	B-cell leukemia/lymphoma 2 protein
BFP	Blue Fluorescent Protein
BM	Bone Marrow
BrdU	Bromodeoxyuridine
CD33	Cluster of Differentiation 33
CD34	Cluster of Differentiation 34
CD38	Cluster of Differentiation 38
CD45-APC	Cluster of Differentiation 45 - Allophycocyanin
cGAS	cyclic GMP-AMP synthase
CR	Complete Remission
CSC	Cancer Stem Cell
DNA	Deoxyribonucleic Acid
Doxo	Doxorubicin
DTPs	Drug tolerant persister cells
ELDA	Extreme Limiting Dilution Analysis
ELN	European Leukemia Net
ER	Endoplasmatic Reticulm
ERGIC	Endoplasmic-reticulum–Golgi intermediate compartment
FAB	French-American-British Classification
FACS	Fluorescence-activated cell sorting
FLT3	Fms-like tyrosine kinase 3
GBC	Guide Barcode
GBP1	Guanylate Binding Protein 1
GBP4	Guanylate Binding Protein 4
GFP	Green Fluorescent Protein
GMP	Granulocyte-monocyte Progenitors
GO Term	Gene Ontology term
H2B	Histone 2 B
HSC	Hematopoietic Stem Cell
HSCT	Hematopoietic stem-cell transplantation
IC50	Half-maximal inhibitory concentration
IDH1	Isocitrate dehydrogenase 1
IDH2	Isocitrate dehydrogenase 2
IFI44	Interferon-Induced Protein 44
IFI44L	Interferon Induced Protein 44 Like
IFI6	Interferon-alpha inducible protein 6
IFIT1	Interferon Induced Protein With Tetratricopeptide Repeats 1
IFITM1	Interferon-induced transmembrane protein 1
IFN	Interferon

IP	Intraperitoneal
IRDS	IFN-related DNA damage resistance signature
IRF7	Interferon regulatory factor 7
ISG	Interferon Stimulated Gene
ISG15	Interferon Stimulated Gene 15
IV	Intravenously
KD	Knock-Down
KEEG	Kyoto Encyclopedia of Genes and Genomes
LIC	Leukemia Initiating Cell
LMAN1	Lectin, Mannose Binding 1
LR	Label retaining
LSC	Leukemia Stem Cell
LY6E	Lymphocyte Antigen 6 Family Member E
MOI	Multiplicity of infection
MX1	MX Dynamin Like GTPase 1
NDUFA13	NADH:Ubiquinone Oxidoreductase Subunit A13)
NGS	Next Generation Sequencing
NMP1	Nucleophosmin 1
NSG	NOD SCID IL2RG null
OXPHOS	Oxidative Phosphorylation
PARP9	Poly(ADP-Ribose) Polymerase Family Member 9
PB	Peripheral Blood
PDX	Patient Derived Xenograft
qPCR	Quantitative polymerase chain reaction
RBC	Red Blood Cell
RFP	Red Fluorescent Protein
RNA	Ribonucleic acid
ROS	Oxygen reaction species
RPM	Reads per milion
RTN3	Reticulon 3
SCR	Scramble
scRNAseq	Single Cell RNA sequencing
SPL	Spleen
STING	Stimulator of Interferon Genes
TBK1	TANK Binding-kinase 1
TIC	Tumor Initiating Cell
TGCA	The Cancer Genome Atlas Program
TRIM22	Tripartite Motif Containing 22
TRIM38	Tripartite Motif Containing 38
USP18	Ubiquitin specific peptidase 18
VAF	Variant Allele Frequency
VWCE	Von Willebrand Factor C And EGF Domains
WES	Whole Exome Sequencing
WHO	World Health Organization

FIGURES INDEX

TABLES INDEX

ABSTRACT

Acute Myeloid Leukemia (AML) remains an incurable disease, with a 5-year survival rate below 30%. While the introduction of new therapeutic approaches, such as targeted therapies and immunotherapy, has had a modest impact on AML prognosis, the standard treatment of AML is still based on chemotherapy regimens (like "7+3") that have been in use for over 50 years. Approximately 20% of patients do not respond to standard chemotherapy, and even among those who initially respond, around 50% eventually relapse due to the development of chemotherapy resistance. Chemoresistance is the cause of death for over 90% of AML patients.

The mechanisms underlying chemoresistance in AML are not yet fully understood, and targeted therapies aimed at preventing chemoresistance are not currently available. Chemoresistance in AML is primarily driven by non-genetic mechanisms. While leukemic stem cells (LSCs) have been implicated, recent studies suggest that AML blasts that survive chemotherapy, known as Chemotherapy Persistent Blasts, enter a senescence-like and diapause state. Though they can contribute to disease recurrence, these Persistent Blasts are not inherently therapy-resistant as they revert to a drug-sensitive state upon drug withdrawal. However, a lack of robust in vivo models of clinical chemoresistance in human AML hinders our understanding of these mechanisms. To address this, I aimed to generate in vivo models of truly chemoresistant AML to investigate non-genetic mechanisms of chemotherapy resistance.

I utilized mouse models of human AML, specifically Patient-Derived Xenografts (PDXs), to establish treatment protocols mimicking the standard "7+3" chemotherapy regimen used clinically. One model (AML9) mirrored the behavior of most patients treated with standard chemotherapy, exhibiting clinical remission followed by relapse. In contrast, the other model (AML20) showed a modest response to chemotherapy with rapid leukemia re-expansion. Notably, relapsed leukemias in both models were completely resistant to retreatment with the same chemotherapy regimen, and this resistant phenotype persisted even after re-transplantation. Extensive genomic profiling revealed that chemoresistance in relapsed leukemias was not associated with the emergence of de novo DNA mutations. AML9 and AML20 represent the first two available AML models of true clinical chemoresistance, mirroring primary and secondary resistance, respectively.

To investigate mechanisms of chemoresistance in these models, I characterized the cellular and molecular properties of Chemotherapy Persistent Blasts isolated at the end of the chemotherapy regimen. To monitor and isolate quiescent blasts during leukemia growth and after chemotherapy treatment, I incorporated a label-retaining (LR) assay into the PDX models, enabling cell division tracking through inducible expression of H2B-GFP. I found that: i) in vitro, Persistent Blasts from both models exhibited significantly higher IC50 values compared to non-treated blasts, suggesting the induction or selection of a stable and cell-autonomous chemoresistant phenotype; ii) Quiescent blasts were slightly enriched among Persistent Blasts, but a portion of leukemia cells continued to proliferate during treatment, generating a population of Persistent Blasts of both proliferating and quiescent cells; iii) Persistent Blasts retained regenerative potential in vivo, primarily attributed to persistent quiescent blasts, suggesting that quiescence, while not a specific trait of chemoresistance, is integral to the relapsing properties of these cells; iv) the AML clonal structure remained unchanged after chemotherapy treatment, as determined by lineage tracing of Persistent Blasts and relapsed leukemias, suggesting that chemotherapy does not select specific cellular lineages; v) Persistent Blasts exhibited distinct transcriptional features compared to untreated leukemias, characterized by stem-cell signatures and activation of the Interferon (IFN) signaling pathway. Notably, IFN signaling activation was a distinguishing feature of both quiescent and proliferating blasts and was predictive of clinical response to standard chemotherapy in AML patients.

To investigate the contribution of the activated IFN signaling pathway to chemoresistance, I examined the effect of silencing IFI6, the top upregulated gene in the IFN signature. IFI6 silencing prolonged latency and reduced engraftment frequency in AMLs, due to its detrimental effect on leukemia-initiating cells (LICs). However, IFI6 silencing did not impact leukemia outgrowth kinetics. Strikingly, IFI6 silencing completely reversed the chemoresistant phenotype in both AML models in vivo and increased the chemosensitivity of established AML cell lines in vitro.

To further explore mechanism of IFI6-mediated chemo-sensitization, I investigated the interaction between IFI6 and STING. I found that IFI6 is upregulated upon chemotherapy treatment and relocates to the ERGIC compartment in proximity to STING, where STING activation by chemotherapy-induced DNA damage initiates a cascade leading to IFN signaling and cell death. Based on these findings, I initiated experiments to determine

whether IFI6-mediated chemoresistance is due to its ability to downregulate STING activation, thereby preventing the execution of IFN-induced cell death.

1 INTRODUCTION

1.1 Acute Myeloid Leukemia

1.1.1 General Overview

Acute Myeloid Leukemia (AML) is the most common type of hematological malignancy in adults [1] with an estimated incidence of 8.8 cases *per* 100,000 men and women in Europe for the year 2012 [2]. It is a malignant clonal disorder of the blood characterized by aberrant proliferation of abnormal and, often, poorly differentiated myeloid progenitors (blasts), which primarily accumulate in the bone marrow (BM), invade the peripheral blood (PB) and occasionally infiltrate other extramedullary tissues. It is characterized by the expansion of blasts blocked at different stages of differentiation, leading to ineffective normal haematopoiesis, and resulting in life-threatening cytopenias and transfusion dependency. AML accounts for over 80,000 deaths globally per annum, with this number expected to double over the next two decades [3].

AML incidence increases in patients aged 65 years old or older [4,5]. Noteworthy, AML has an explicitly poor outcome in the elderly, with less than 5% of the patients being alive 5 years after the diagnosis. Conversely, youthful patients' long-term survival stands at approximately 40-50%. However, despite the initial response to chemotherapy and the improvement in the therapeutic regimens for some AML subtypes, 50% of younger patients relapse and succumb to the disease within 5 years from diagnosis [6].

The diagnosis of AML has historically been confirmed in over 30%, and more recently over 20%, of blasts of the myeloid lineage identified in the BM, or the presence of specific AML-defining genomic abnormalities regardless of blast percentage [7]. Once AML diagnosis is confirmed, a series of diagnostic evaluations is carefully performed and this includes: morphological assessment, immunophenotyping by flow cytometry, and genomic analysis including conventional karyotype and DNA profiling.

An accurate clinical, pathophysiological, cytogenetic and molecular classification of such assorted profiles is fundamental for proper diagnosis, risk classification and choice of the best therapeutic approach.

The classification of AML has been constantly updated and changed since the first French-American-British (FAB) classification back in 1976, which was based only on the morphology of leukemic blasts. Nowadays, this type of classification is considered not adequate of AML disease risk. Indeed, most recently, AML classification has been updated

by both the World Health Organization (WHO) and the International Consensus Classification (ICC), highlighting increased reliance on cytogenetic and molecular features of the tumor [8,9,10]. The WHO classification divides AML into several groups: AML with certain genetic abnormalities (gene or chromosome changes), AML with myelodysplasia-related changes, AML related to previous chemotherapy or radiation, AML not otherwise specified, myeloid sarcoma, Down syndrome-related myeloid proliferations [11].

However, this classification fails in pondering the impact on the prognosis of the multiple genetic abnormalities characterizing leukemic blasts. The European LeukemiaNet (ELN) released the first genetic-based stratification system for AML in 2010, with the final version revised in 2022 [12]. This classification allows for the allocation of patients into three different prognostic groups: favorable, intermediate and adverse; thanks to the consideration of both karyotype assessment and the presence of mutations.

Favorable-risk leukemias include the core-binding factor leukemias associated with t(8;21) and inv(16) or t(16;16), and acute promyelocytic leukemia (t[15;17]). The t(8;21) and t(15;17), which are responsible for the expression of the AML1-ETO and PML-RARα fusion proteins, respectively, and are the only translocations indicative of favorable prognosis, while complex and/or monosomal karyotype are usually associated with a higher probability of therapy failure. AML with NPM1 mutation (in the absence of FLT3–ITD), or in-frame CEBPA mutations within the basic leucine zipper region are more sensitive to chemotherapy treatment, and are now categorized as favorable-risk in the updated ELN 2022 recommendations [10]. In the ELN 2022 recommendations, adverse risk disease now includes two additional entities: AMLs with myelodysplastic syndrome- related gene mutations (ASXL1, RUNX1, BCOR, EZH2, SF3B1, SRSF2, STAG2, U2AF1, and ZRSR2) and cytogenetic fusion t(8;16) (KAT6A::CREBBP). Intermediate-risk leukemias represent the remaining approximate 40% of patients with AML, and often include patients with normal diploid cytogenetics. Importantly, the updated ELN 2022 recommends that all FLT3–ITD mutated AML is considered intermediate risk; neither the FLT3–ITD allelic ratio nor the presence or absence of NPM1 mutations affect risk classification [10].

Despite this classification helped to organize AMLs based on different markers, contributing to patient risk stratification and facilitating the choice of personalized therapy (whenever possible), the major obstacle in AML eradication is still represented by the extensive genomic and biological inter- and intra-tumoral heterogeneity.

Indeed, recent advances in NGS and single-cell technologies have revealed the complex mutational landscape of AML: over 200 recurrent mutations have been identified, many of which co-exist in a single patient (80% of the patients have three or more recurrent

mutations) and are associated with different transcriptional and epigenetic features [13,14]. Indeed, AML is a complex and heterogeneous ecosystem of genetic clones and sub-clones that evolves over time under natural or therapeutic selection and pressure, and is becoming more and more evident that the complete understanding of the molecular mechanisms underlying each genetic combination and the relationship with tumor microenvironments are required to define new therapeutic intervention [13,14,15].

Risk category†	Genetic abnormality
Favorable	• t(8;21)(q22;q22.1)/*RUNX1*::*RUNX1T1*†,‡ • inv(16)(p13.1q22) or t(16;16)(p13.1;q22)/*CBFB*::*MYH11*†,‡ • Mutated *NPM1*†,§ without *FLT3*-ITD • bZIP in-frame mutated *CEBPA*‖
Intermediate	• Mutated *NPM1*†,§ with *FLT3*-ITD • Wild-type *NPM1* with *FLT3*-ITD (without adverse-risk genetic lesions) • t(9;11)(p21.3;q23.3)/*MLLT3*::*KMT2A*†,¶ • Cytogenetic and/or molecular abnormalities not classified as favorable or adverse
Adverse	• t(6;9)(p23.3;q34.1)/*DEK*::*NUP214* • t(v;11q23.3)/*KMT2A*-rearranged# • t(9;22)(q34.1;q11.2)/*BCR*::*ABL1* • t(8;16)(p11.2;p13.3)/*KAT6A*::*CREBBP* • inv(3)(q21.3q26.2) or t(3;3)(q21.3;q26.2)/*GATA2, MECOM(EVI1)* • t(3q26.2;v)/*MECOM(EVI1)*-rearranged • −5 or del(5q); −7; −17/abn(17p) • Complex karyotype,** monosomal karyotype†† • Mutated *ASXL1*, *BCOR*, *EZH2*, *RUNX1*, *SF3B1*, *SRSF2*, *STAG2*, *U2AF1*, and/or *ZRSR2*‡‡ • Mutated *TP53*[a]

Figure 1 2022 ELN risk classification by genetics at AML diagnosis.

Adapted from Dohner et al., Blood, 2022

In the absence of treatment, patients succumb to the disease, usually within one year after diagnosis, due to fatal complications associated with the BM failure (hemorrhage and infection)[16]. Despite recent advances in AML treatment, the therapeutic intervention has remained essentially unaltered for the last 50 years; indeed, anthracycline-based chemotherapy remains the principal option for treatment. For adult AML patients, standard induction therapy consists of *"7+3"* regimen (7 days of continuous infusion cytarabine (100-200 mg/m^2) and 3 days of intravenous administration of anthracycline (daunorubicin at least 60 mg/ m^2 or idarubicin 12 mg/ m^2 or mitoxantrone 12 mg/m^2). Around 60-80% of younger patients (< 60 years) respond to induction therapy and initially achieve complete remission (CR), which is defined by a blast count <5% in the BM and an increase in the neutrophil

(>100) and platelet (>100,000) counts [16,17]. However, 20% of them do not respond and among older individuals (>60 years), the percentage of patients who respond is lower, (40-60%). Regardless, 40–60% of AML patients will relapse, due to the emergence of cellular resistance to anti-leukemic drugs [17] and there is no specific therapy of choice for patients with relapse, thus, there is a compelling need to identify novel strategies to reverse drug resistance.

1.1.2 AML Therapy

Intensive AML therapy is administered with curative intent. The notion for treatment includes induction (with a goal of morphological remission), followed by post-remission consolidation therapy to reduce or eliminate residual disease. The goal of treatment is control and, whenever possible, the eradication of disease. This outcome is accomplished ideally by inducing a CR with initial therapy, followed by consolidation and/or maintenance efforts to deepen the remission and maximize response duration.

The most common intensive chemotherapy regimen has remained unchanged since the last 50 years and is the induction chemotherapy called *"7+3"* regimen. Indeed, starting in the 1970s, *"7+3"* (cytarabine + daunorubicin) treatment regimen became the standard of care for patients with AML. It incorporates cytarabine (100–200 mg/m2/day) for 7 days via continuous infusion), and an anthracycline (idarubicin or daunorubicin) for 3 days [18]. Consolidation can include intermediate or high-dose cytarabine-based consolidation (ELN 2022 guidelines recommend three to four cycles of cytarabine 1000–1500 mg/m2 intravenously over 3 h, ever 12 h for 3 days, or 500–1000 mg/m^2 intravenously over 3 h q12 for 3 days if >60 years), allogeneic hematopoietic stem-cell transplantation (HSCT), and maintenance therapy.

Several practice-changing improvements to intensive AML chemotherapy have occurred over the past decade, which have reinforced the importance of rapid cytogenetic and molecular characterization of AML for timely initiation of optimal treatment. For example, the addition of the multikinase inhibitor midostaurin to the *"7+3"* induction was shown to improve long-term survival (RATIFY trial) with a 4-year overall survival of 51%with midostaurin compared with 44% with placebo [19]; another example is the addition of selective FLT3-ITD inhibitor quizartinib in combination with "*7+3"* demonstrating an improvement in complete remission and overall survival compared with intensive *"7+3"* chemotherapy alone (Erba H, EHA2022; June 9–17, 2022 (abstr S100)). For 20% of patients presenting with IDH1 or IDH2 mutations, a placebo-controlled randomized frontline clinical

trial of standard induction with the addition of the targeted IDH1 inhibitor (ivosidenib) or the targeted IDH2 inhibitor (enasidenib), followed by HSCT or IDH inhibitor maintenance, is ongoing (NCT03839771) [20]. The liposomal daunorubicin-cytarabine formulation CPX-351 is recommended for newly diagnosed AML patients, on the basis of results of the randomized phase 3 study showing improved remission rates and prolonged overall survival of CPX-351 compared with standard *"7+3"* chemotherapy in patients between 60 and 75 years of age [21]. Additionally, gemtuzumab ozogamicin, the CD33 monoclonal antibody linked to a calicheamicin warhead, was reapproved in 2017, to be used alone or in combination with conventional chemotherapy for patients with AML expressing CD33 [22].

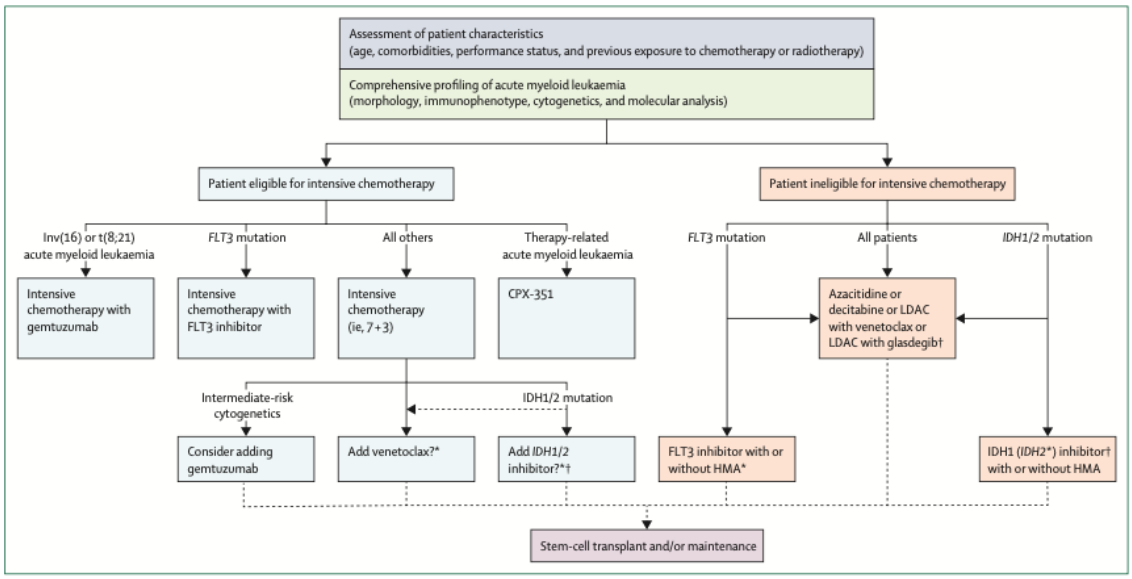

Figure 2 Treatment for newly diagnosed Acute Myeloid Leukemia

Adapted from DiNardo et al., The Lancet, 2023.

Moreover, in the last years, Venetoclax has emerged as an important treatment option for AML patients, particularly in older patients or those who are not candidates for intensive chemotherapy [23]. It is an oral targeted therapy and it functions as a B-cell lymphoma 2 (BCL-2) inhibitor, promoting apoptosis (programmed cell death) in cancer cells by neutralizing BCL-2. Venetoclax is often used in combination with hypomethylating agents like azacitidine or decitabine, or with low-dose cytarabine. Clinical trials have demonstrated that these combinations can lead to significant response rates and prolonged survival compared to traditional treatments, particularly in patients with newly diagnosed AML who are over 75 years old or have comorbidities that preclude the use of standard chemotherapy [24]. However, venetoclax therapy requires careful management due to potential side effects, such

as tumor lysis syndrome and myelosuppression. Its introduction has expanded therapeutic options for patients with AML, particularly those with limited treatment avenues, offering a more targeted and potentially less toxic approach to managing the disease. [25]

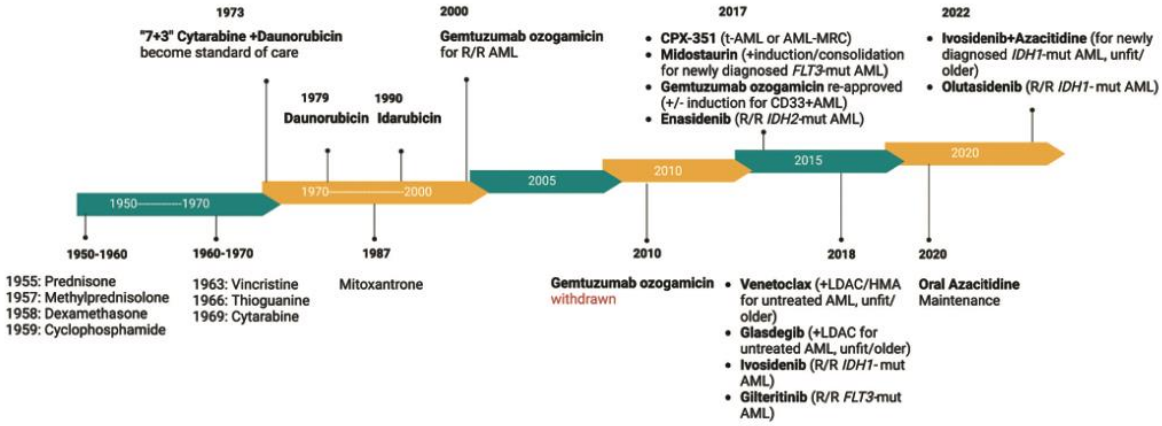

Figure 3 Time line of Acute Myeloid Leukemia therapy

Adapted from Venugopal et al., Expert Review of Hematology, 2023

1.2 AML Chemoresistance

Emerging evidence suggests that drug resistance in cancer cells, including AMLs, is a consequence of intratumor heterogeneity [26,27]. Two levels of intratumor heterogeneity are generally recognized: genetic and phenotypic. Intratumor genetic heterogeneity is defined by the presence of multiple cellular sub-clones with different genotypes and is the consequence of the progressive accumulation of mutations during leukemogenesis. Intratumor phenotypic heterogeneity (also referred to as non-genetic heterogeneity) instead represents specific transcriptional, translational and metabolic traits acquired by cancer cells as a consequence of the phenotypic adaptation to the changing tumor microenvironment, and the exposure to external stresses, including therapies, or to specific metabolic requirements of cancer cells, as those induced by oncogene expression and hyper-proliferation [28]. Such adaptations are critical for tumor development/maintenance, and might contribute to resistance to therapy, independently of (or in addition to) the acquisition of novel DNA mutations.

A further level of phenotypic heterogeneity is represented by the presence, within tumors, of rare cancer cells with the unique property of propagating tumors in model

systems, so-called tumor initiating cells (TICs) in solid tumors, or leukemia initiating cells (LICs) in leukemia [29].

Leukemic cells quiescence is a further level of phenotypic heterogeneity and a putative mechanism of drug resistance, due to the intrinsic resistance of non-proliferating cells to chemotherapy treatment. In AMLs, a large fraction within individual samples is not actively cycling and remains in a non- dividing state. These cells show limited sensitivity to conventional cell cycle-active chemotherapeutic drugs and may repopulate tumors after treatments [30,31]. However, the biological significance of leukemia cell quiescence, underlying molecular mechanisms and its contribution to the emergence of resistance in AMLs, are currently unknown.

The mechanisms underlying chemoresistance in AML are not yet fully understood and characterized. Though a few detailed studies are available using patient samples, some studies provide insights into possible causes and mechanisms of chemoresistance. For decades, chemoresistance was known to be the consequence of genetic alterations which give an advantage to some leukemic blasts, so they can survive chemotherapy and eventually relapse [17,32,33]. Furthermore, there is increasing evidence that non-genetic processes drive drug resistance, representing a major hurdle to successful cancer therapy. Chemo-persistent cells, (cells that survive at the end of treatment), are emerging key players of drug resistance and are identified across a wide range of tumors in response to chemotherapy and targeted agents [34,35,36] Recently, epigenetic/phenotypic changes were recognized over genetic changes as the main cause of survival of leukemic blasts after chemotherapy treatment and subsequent relapse development.

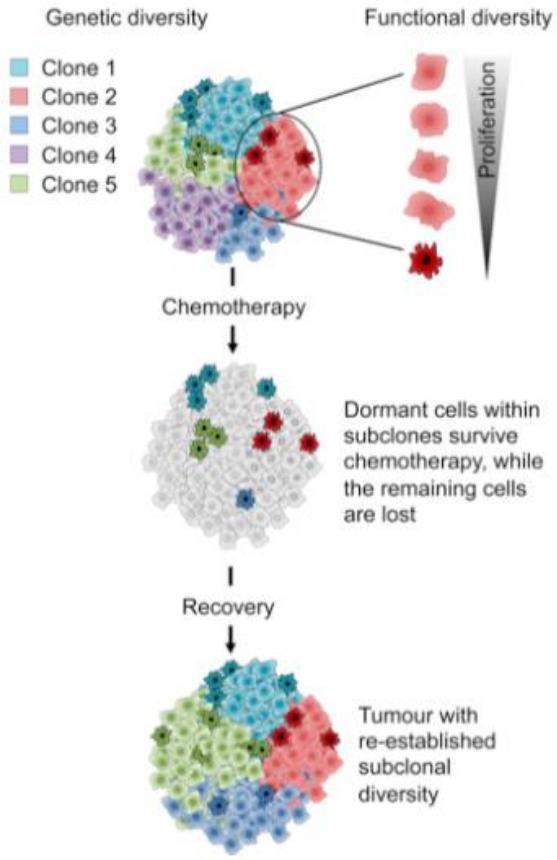

Figure 4 Impact of intratumor heterogeneity on AML treatment response

Each genetic clone is characterized by a heterogeneous population of cells with different phenotypic properties, such as proliferation, quiescence, dormancy…. Quiescent cells within each clone may persist during chemotherapy treatment and generate the relapse clones. Adapted from Cell Stem Cell (Kreso and Dick, 2014).

An open question is whether chemotherapy-persistent blasts are drug-resistant or not, and if their survival is related to their intrinsic chemoresistant features, related to their quiescence, or to a protective microenvironment. In both patients and models systems, post-chemotherapy there is an evident drop in the percentage of leukemic blasts in BM (in humans, less than 5% of leukemic blasts in BM are considered complete remission, CR). Instead, in model systems, remission represents a significant drop in the percentage of leukemic blasts in BM.

Current literature provides robust evidence suggesting that relapse originates from rare persistent AML cells which survive chemotherapy [37]. Remarkably, however, it is not clear whether persistent cells are drug resistant or not. Clinical data suggest true drug resistance (*e.g.*, patients who relapse after chemotherapy are resistant to next round of

chemotherapy). Model systems, instead, provided conflicting results, with part of data suggesting drug resistance, while others drug sensitivity, even after several rounds of chemotherapy [38]. In the latter the selection of cell cycle-restricted (diapaused) cells was proposed as the mechanism underlying the emergence of drug-sensitive disease. Diapause is a reversible physiological state of suspended development of an embryo (in insects, invertebrates and certain mammals) triggered by adverse conditions. Although experimental evidence is only just emerging for the potential of human embryos to enter diapause, human cancer cells (breast, prostate and colon cancer and AML) in the DTP state were shown to acquire this transient diapause-like gene expression profile to survive chemotherapy and targeted therapy. Selection of specific drug-resistant genotypes or phenotypes, instead, has not been yet explored. Finally, it's still unknown if persistent cells are LIC-enriched or not [39,40].

1.2.1 Chemoresistance in AML patient

Mechanisms of chemoresistance in AML are not fully understood and existing data cover only small pieces in a big picture of cancer resistance. Patient data are not thoroughly described in literature, however there are studies which give an insight into possible causes and mechanisms.

For decades, chemoresistance has been known/accepted to be the consequence of genetic alterations which give advantage to some leukemic cells, so they can survive chemotherapy and eventually relapse [32,17,33]. Some mutations are found to be commonly present in patients with leukemia, such are NPM1, FLT3, CEBPA, DNMT3A, IDH1, and IDH2, and more recently found EZH2, U2AF1, SMC1A, and SMC3 [41]. Mutations involved in epigenetic regulation are found to show up early in development of leukemia, and they are most commonly found to be the founder event. Such mutations are DNMT3A, ASXL1, TET2, IDH1, and IDH2 [42,43,44]. Instead, mutations like NPM, FLT3, RAS are found to appear later in leukemia development and they represent secondary events. Whole genome sequencing analysis showed that relapse can rise either from the founder clone which gained new mutations and became a relapse clone, or from subclone with acquisition of additional mutations [45,46]. Moreover, it has been shown that relapse samples, compared to primary ones contain new mutations, suggesting that chemotherapy, possibly by cytotoxic effect, induces appearance of new mutations [45]. Instead Shlush et al. give an opposite view, suggesting that chemotherapy doesn't influence mutagenesis, but only selects the cells who carry genetic predisposition to cause the future relapse [27].

Recently, not just genetic changes are recognized as the main cause of survival and relapse of leukemic cells, but also epigenetic/phenotypic changes. Epigenetic changes comprise all non-genetic changes, among which we can include epigenetic modifications (e.g., methylation), transcriptional and translational modifications, as well as extracellular modifications (niche signaling, chemotherapy etc.).

Fugureoa et al. discovered that AMLs have common aberrant DNA methylation signature consisting of 45 genes, out of which most were hypermethylated. These genes are likely to be part of a common epigenetic pathway which is involved in leukemic transformation of hematopoietic cells [47]. Landau et al. suggested a model in which methylation pattern of genes coincides with novel somatic mutations in order to propagate new genotype to the progeny populations [48]. Li et al. explored the influence of epigenetic modifications on disease progression and relapse. They observed variable epiallele modifications during disease progression. Opposite to previous studies, they discovered that epiallele diversity don't always follow changes of somatic mutation burden and they suggest a model in which disease has two different kinetics, genetic and epigenetic, which in some cases might be related one to another, but in most cases, they follow two independent kinetics. Moreover, they noticed that shifts in epiallele frequency occur in early time points of disease progression, instead increase in abundance of somatic mutations was observed at late time points, suggesting that epigenetic modifications can anticipate genetic modifications during disease progression [49].

Furthermore, phenotypic states, like stemness and quiescence can also influence how disease will progress or relapse. Stemness is a property of a cell, defined by immature phenotypic profile similar to that found in stem cells. Leukemia stem cells (LSCs), as expected, have immature phenotypic profile, however, other, more mature cells, can also express more primitive transcriptional profiles. Above mentioned, Slush et al. showed that relapse can be caused by both LSCs and lineage committed cells, however in both cases, relapse is due to cells who posses stem cell properties [44]. Many studies tried to explore the role of LSCs on survival and relapse. Ho et al. demonstrated 9-90 -fold increase in frequency of LSCs from primary tumor to relapse, however, this study also raised the question of correct detection of LSCs, considering that unique markers for LSCs are still unknown [50] Instead, Boyd et al. observed that there is no preferential survival of LSCs and that these cells are eliminated equally post chemotherapy as more mature progenitors, leaving a question mark for the real cause of relapse [37]. Another study established LSC17- list of 17 genes preferentially expressed in populations with high LSC content (CD34, LAPTM4B, ARHGAP22, LOC284422, KIAA0125, MMRN1, DNMT3B, SOCS2, CDK6, NGFRAP1,

CPXM1, ZBTB46, DPYSL3, NYNRIN, GPR56, AKR1C3, EMP1). They demonstrated that expression of these genes can highly predict disease relapse, lower response rates to standard induction chemotherapy, shorter survival and higher rates of chromosome aberrations [51]. Van Galen et al. demonstrated that tumors consist of multiple cell populations (HSC-like, progenitor-like, GMP-like, promonocyte-like, monocyte-like, or cDC-like malignant cells), and that cell composition is greatly influenced by genetic background of the tumor. However, this study also confirms that tumors enriched in HSC/progenitor-like enriched cells have significantly worse outcome [52].

Stemness is commonly related to quiescence, which represents a pause in cell-cycle, and it can be found in normal, as well as in cancer cells. Both, stemness and quiescence are found to be responsible for leukemia cell survival and relapse [53,54]. In most cases, this is explained by mechanism of action of chemotherapy drugs, which mostly act on dividing cells by eliminating them. Quiescent state of cells protect them from these chemotherapeutical agents, thus supporting their survival and following relapse [55]. Wang et al. investigated influence of quiescence to disease outcome and chemotherapy resistance. They showed that patients with higher percentage of quiescent cells predict worse outcome. Moreover, they demonstrated preferential survival of quiescent cells after chemotherapy, suggesting that quiescence might be the protective mechanism against chemotherapy [56]. Yilmaz et al. demonstrated the importance of long-term quiescence in relapse in patents by presenting cases of patients who had late relapse (after more than 5 years). They showed by Whole Exome Sequencing analysis that in most of these patients, relapse was caused by a founder clone, which evolved to relapse clone, suggesting that these cells were in quiescent state for prolonged time, meanwhile acquiring new mutations which enabled them to relapse [57].

Another important factor for leukemia development, survival and relapse is the BM niche, which represents the microenvironment in which healthy hematopoietic, and later malignant AML cells reside. BM stromal cells are found to be the one of the most important cells for maintenance of hematopoietic niche, as well as the major support for development and differentiation of hematopoietic cells. They also have immunomodulatory effect in BM, creating immunosuppressive niche which has positive effect for inducing self-tolerance in cells. However, this feature can also create a niche permissive for development and maintenance of AML [58]. Van Galen highlighted the importance of BM niche in AML, which is found to have fewer numbers of T cells and cytotoxic T cells, and increased numbers of regulatory T cells, making immunosuppressive environment for leukemia growth. Monocyte like cells are found to be the most important immunomodulatory cells, since they are found

to inhibit T cell activation [52]. Wang at al. described the influence of human mesenchymal cells (hMSC) in leukemia survival by inducing quiescence in leukemic cells, and this way protecting AML cells from chemotherapy [56]. Several studies highlighted the importance of endosteal and vascular niche for AML survival, mostly by induction of quiescence and stimulation of LSC self-renewal and proliferation [59,60,61]. Normal, preleukemic HSC are found to localize in endosteal niche, as well as around arterioles and sinusoids [62,63]. In AML, blasts create proinflammatory environment which leads to decrease in numbers of osteoblasts or inhibit their differentiation, and subsequentially, decrease the number of non-malignant HSC, which can't survive in this, newly created niche. In this way AML cells get advantage over HSCs and expand [60]. During leukemia development, remodeling of vascular niche leads to increase in number of BM vessels. Moreover, endothelial cells are found to support AML cells by inducing proliferation and pro-survival signals [61].

Finally, another study suggested the use of leukemia associated plasma membrane (PM) proteins to detect leukemia associated phenotypes, which could be detected in over 90% of patients and could also predict the disease outcome. They showed that PMs can be used to identify genetic clones and also to perform longitudinal tracking of clonal evolution (primary vs relapse) [63].

1.2.2 Chemoresistance in model systems

In recent years, several studies and progresses have been made in order to better characterized the mechanisms of chemoresistance, using mice as principal animal model. Patient-derived Xenografts (PDX) models become an extraordinary tool in cancer research, especially in the context of AML disease. They are used to model the progression of the disease and are extremely useful in the context of studying drug resistance mechanisms *in vivo*. In particular it is possible to study human tumor, from human cancer cells obtained directly form patient's biopsy. Through serial transplantations of human primary tumor cells, it is possible to obtain a tumor which resemble the integrity of the patient's tumor. Furthermore, PDX models can be used to model the therapy regimens used in the clinics, in order to obtain a model that robustly and significantly correlates with the clinical outcome of respective patients.

The nonobese diabetic/severe combined immunodeficient (NOD/ SCID) xenotransplantation assay is currently/nowadays the model of choice for assessment of transplantable human hematopoietic stem cells (HSCs). This approach has been crucial to the understanding of human hematopoiesis, providing reliable determination of the

phenotypes of repopulating cells [64] and elucidating previously undescribed HSCs populations [65]. Moreover, a novel mouse strain has been developed by backcrossing B2 microglobulin–null (B2m-/-) mice onto the NOD/SCID background. The resulting B2m-/-NOD/SCID strain, in addition to the B-cell, T-cell, complement, and partial natural killer (NK) defects that define the NOD/SCID model, has a complete lack of NK cell activity [66] Hence, this model is more permissive to xenotransplantation than the original NOD/SCID strain [67]. Therefore, the NOD/SCID assay appears to reproduce an AML disease very similar and comparable to the patients' disease.

The molecular mechanisms at the basis of relapse in AML are nowadays still not fully understood. While chemotherapy can achieve complete remission in most of AML patients (70-80%), the majority of them (almost two-third) develop relapse within 18 months [68,69]. One of the most accepted and prevalent models of chemoresistance is that AML relapse emerges from the persistence of the so-called Leukemic stem cells (LSCs) or Leukemia initiating cells (LICs) subpopulation [70]. It has been proposed that LCSs preferentially resist chemotherapy, thus providing a cellular reservoir that is thought to form the basis of relapse [71].

Defining and characterizing these cells is particularly challenging in patients, as the number of residual leukemic cells is dramatically reduced post chemotherapy treatment due to the cytoreductive nature of the therapy itself. *In vitro* clonogenic assays and *in vivo* transplantation assays paved the way for the identification of tumoral cells populations with variable tumorigenic potential and the designation of CSCs as the only cells able to sustain tumor initiation and progression *in vivo*.

The majority of CSC research has been derived from the previous ‘‘gold standard’’ assay, which involves FACS-sorting to isolate cell populations based on specific surface markers, followed by inoculation of sorted cells at limited dilutions in serial xenotransplantation assay to assess the tumor-initiating cell (TIC) frequency. In the context of CSC, tumor initiation capacity typically refers to their ability to initiate tumor formation upon transplantation, often in immunodeficient mouse models, rather than their ability to directly induce oncogenic transformation [72].

Pioneering studies in John Dick's lab demonstrated the existence of such a population in AML by the prospective isolation and xenotransplantation into immunocompromised mice of leukemic blasts with different combinations of CD34 and CD38 expression. These studies demonstrated for the first time that only the CD34+CD38- compartment is able to preserve/maintain tumorigenic capacity *in vivo* [73,74].

Therefore, the LSCs concept derived from the observation that only a subpopulation of AML cells with an immature immunophenotype (CD34+, CD38−) can reconstitute leukemia in engraftment experiments using NOD/SCID mice [75]. These cells represent a rare and poorly characterized population of quiescent cells with stem cell features, as self-renewal capacity and drug resistance, and are thought to be responsible for the maintenance of the disease as well as for relapse, as a result of their resistance to traditional therapies that are active against the bulk leukemic cells [76]. Indeed, classic chemotherapy regimens primarily target actively cycling "blast" cells and initially lead to remission. Since quiescent or protected LSCs often avoid eradication, relapse rates are high with 5-year survival rates below 15% for patients over the age of 60. An LSC-like gene signature is detectable at the time of relapse compared to diagnosis, highlighting the central role of LSCs in drug resistance and consequent relapse development [77,78]. However, in other studies the enrichment of LSCs after chemotherapy treatment was not found at nadir (remission phase of AML disease), pointing out the exceeding need to better characterize their role in drug resistance and relapse development.

Furthermore, the existence of CSCs, or otherwise stated, tumor initiating cell (TIC) populations has been since demonstrated also in numerous solid tumors, including breast cancer [79], glioblastoma [80] and colorectal cancer [81].

While advancements have being made to target particular driver mutations in AML, there is less focus on how to tackle the drug resistance mechanisms of quiescent LSCs and how to model chemoresistance and relapse in AML.

There is increasing evidence that non-genetic processes drive drug tolerance, presenting a major hurdle to successful cancer therapy [82]. Drug-tolerant persistent cells are emerging to be key players of non-genetic heterogeneity of tumors and have been identified across a wide range of tumors in response to chemotherapy and targeted agents [83,84,85]. Genotoxic stress induced by chemotherapy, besides apoptosis, promotes senescence [86,87], a conserved cellular stress response mechanism characterized by aberrant metabolic activity in the absence of proliferation [88]. It is initiated by a wide range of stimuli including DNA damage, oncogene activation, telomere erosion, protein misfolding, oxidative damage, extracellular signaling by mitogens or cytokines, and high-fat diet [88].

Duy et al., [89], using both human AML samples and PDX models, hypothesized that AML relapse is dependent on the persistence of a subset of resistant cells undergoing a senescence-like resilient state, potentially mimicking a diapause state, to survive genotoxic stress caused by chemotherapy and eventually be able to reconstitute the entire disease. The embryonic diapause is an evolutionary conserved strategy that describes a reversible growth

arrest (up to many months) of blastocysts [90,91], allowing survival during stressful environmental conditions. Diapause is defined as a reversible state of suspended embryonic development triggered by unfavorable environmental conditions [92]. It also been demonstrated that drug resistant persistent cells share a diapause-like dormancy signature in solid tumors (e.g., Colorectal Cancer), [93] evidencing emerging role of this embryonic state in the context of chemoresistance which need to be better characterized.

Furthermore, Farge et al., [94], showed that persisting chemo-resistant cells compared to chemo-sensitive cells exhibited an enriched high OXPHOS gene signature, high ROS levels and increased mitochondrial mass with active and polarized mitochondria, all characteristics that are consistent with a high OXPHOS signature. Strikingly, they found that residual AML cells are not enriched in immature, quiescence cells or LSCs. Using PDX models, they instead demonstrated that the high OXPHOS status is peculiar of AML resistant cells *in vivo*, and that it is also found and enriched at diagnosis in the transcriptomes of AML patients who show low response to standard induction chemotherapy regimens (AraC, IDO…) correlating with negative prognosis index in TCGA [95]. Their results strongly suggested that mitochondrial and OXPHOS activities greatly influence the sensitivity and *in vivo* efficacy of chemotherapeutic agents, by a shift of human AML cells from a high- to a low- OXPHOS status. They finally propose that metabolic flexibility as well as mitochondrial dependency are two crucial requirements of chemotherapy resistance of AML cells *in vivo* thus proposing mitochondrial OXPHOS as a pivotal factor in AML chemoresistance, and high OXPHOS signature and metabolism as key hallmarks of *in vivo* chemoresistance.

Recently, Sauvageau et al. [96] revealed the presence of metabolic differences between chemotherapy-resistant AML cell subpopulation and chemotherapy-sensitive AML subpopulation. They found that chemotherapy-sensitive AML cell subgroups did not require mitochondrial respiration to produce energy, while the chemotherapy-resistant AML cell subgroups were shown to be highly dependent on NADH dehydrogenase activity for survival.

Moreover, in the context of metabolism, it is well known and accepted that AML cells have immense metabolic plasticity that enables them to use different sources of energy such as fatty acids and amino acids to support mitochondrial metabolism [97]. In particular oxidative phosphorylation has been demonstrated to be essential for blasts to become drug resistant [3998], using cells form matched patient treatment-naïve and post-treatment BM samples, showed that LICs became less dependent on glycolysis while upregulating mitochondrial metabolism. During AML development they found that LICs increased both

fatty acid oxidation and amino acid metabolism (in particular branched chain amino acids metabolism), both of which are known to supply the Krebs cycle with intermediates and upregulate the expression of key transporters of fatty and amino acid such as CD36 and a large number of solute carriers (SLCs) [99,100] Furthermore, they identified several pathways commonly modulated during disease progression including signaling networks involving metabolism, apoptosis (upregulation of anti-apoptotic genes as BCL2, c-FLIP, SOCS3, MCL1) and chemokine signaling (heterogeneous expression of CXCR4), suggesting curative treatment will require the simultaneous targeting of multiple pathways in order to fully eradicate LICs.

It has been proposed that the microenvironment in the BM niche could also affect drug resistance in AML providing a protective shelter to promote chemotherapy resistance. The surrounding microenvironment temporarily protect blasts from apoptosis, thus leading to the preservation and even expansion of resistant adaptive tumor cell subsets [101]. This microenvironment induced resistance could be regulated by soluble factors (e.g., CXCL12, VEGF, IL-6, G-CSF) and/or cell-adhesion-mediated (selectins, integrins, cadherins, fibronectin, laminin, osteopontin, collagen). IL-6, an important cytokine mediating proliferation and differentiation of HSCs, is primarily secreted by BM stromal cells and various hematological malignancy cells [102]. Aberrant activation of STAT3 has been found to induce anti-apoptosis by up-regulation of BCL-2 family in a wide range of malignances including AML [103]. Moreover, Erbani et al. [104] demonstrated that CD162, a key E-selectin receptor involved in AML progression, is also involved in chemoresistance *in vitro* and *in vivo*. They showed that AML blasts with deleted CD162 gene expression, isolated from transplanted mice, have a significant increase in chemosensitivity (2.5-fold increase) compared to WT AML *in vivo*. Moreover, CD162 depleted AML cells have a marked loss of blast quiescence and a strong increase in cycling AML blasts in the BM.

1.3 IFN and cancer: the outstanding paradox

Chronic activation of interferon signaling is emerging as a general mechanism underlying therapy resistance in cancer. While acute exposure of cancer cells to high concentrations of type I interferon (IFN-I) can induce growth arrest and apoptosis, chronic exposure to low concentrations paradoxically confers significant pro-survival advantages. Accordingly, constitutive activation of IFN-I in cancer cells promotes pro-survival responses and is thought to be involved in the establishment of resistance to both DNA-damaging therapies and checkpoint inhibitors.

In the context of cancer, IFNγ has established a reputation for being an immunologic guardian against neoplastic disease and it has historically been considered a central player in antitumor immunity playing a pivotal role in cancer immunology. It has been a cornerstone in antitumor immunity largely due to its ability to modulate both the intrinsic properties of tumor cells and the activity of immune effector cells. Specifically, IFNγ induces the upregulation of the MHC class I molecules in tumor cells thus enhancing their antigenicity due to increased antigen presentation [105]. Additionally, IFNγ enhances the cytotoxic activities of natural killer (NK) cells and cytotoxic T Lymphocytes (CTLs), which are critical for effective antitumor responses [106] [107]. These dual effects of IFNγ synergize to make the tumor cells more susceptible to recognition and destruction by IFNγ-activated immune effector cells by virtue of enhanced presentation of tumor-associated antigens [105] [108]. Moreover, IFNγ has direct tumor cell-specific antitumor effects; it can inhibit tumor cell proliferation through the induction of cell cycle arrest mediated by the activation of tumor suppressor proteins p21 and p27 [109] and it is also known to play antitumor role by inducing apoptotic cell death of multiple cancer cell types [110].

Although IFNγ quickly developed a conventional, well-recognized, and well-characterized reputation as an antitumor immune factor, its potential as a protumor factor also has a long history [111]. Emerging evidences suggest IFNγ to play a role in promoting tumor progression, thus generating a paradox in its function. One common theme that seems to emerge from the studies that show pro-tumorigenic effects of IFNγ is that tumors that are exposed to IFNγ show greater immunoevasive capabilities.

For instance, continuous exposure to prolonged and/or elevated IFNγ levels can lead to selective immune pressure on the tumor cells, ultimately resulting in the downregulation or loss a of MHC class I molecules and other genes involved in the antigen presentation machinery, thereby decreasing the immune system's ability to recognize and eradicate tumor cells [112] [113]. Such a mechanism/phenomenon has been observed in various cancer cell lines, including M14 melanoma and CT26 colon cancer, where IFNγ exposure resulted in reduced antigen presentation and enhanced immune evasion [114] [115].

Emerging evidences suggest that cancer cells can respond in different ways to IFN. Indeed, it has been showed that acute exposure of cancer cells to high concentrations of type I Interferon (IFN-I) drives growth arrest and apoptosis, whereas chronic exposure to low concentrations provides important pro-survival advantages. Tyrosine-phosphorylated IFN-stimulated gene (ISG) factor 3 (ISGF3) drives acute deleterious responses to IFN-I, whereas

unphosphorylated (U-)ISGF3, lacking tyrosine phosphorylation, drives essential constitutive pro-survival mechanisms (10.1016/j.trecan.2022.09.003).

Therefore, IFN response has two separate and distinct phases: an acute in which ISGF3, formed from IFN response factor 9 (IRF9) and tyrosine-phosphorylated STAT1 and 2, drives the expression of the full set of ISGs. Since the maximal antiviral effects of the initially induced proteins cannot be sustained by cells for very long without causing damage, powerful negative regulatory mechanisms, especially those due to the IFN-I-induced protein SOCS1, suppress the continued phosphorylation of STAT1 and STAT2 within about 1 day.

During the second phase, the so-called chronic phase, STAT1, STAT2, and IRF9 are themselves ISGs, leading to a prolonged steady state in which these three proteins, now highly expressed but lacking tyrosine phosphorylation, form U-ISGF3, which continues to drive the expression of about a quarter of the initially induced ISGs for many days. The encoded proteins, well tolerated by the cells, continue to provide a substantial level of antiviral protection, albeit much less than in the initial, transient antiviral state. U-ISGF3, drives the expression of a subset of ISGs, the IFN-related DNA damage resistance signature (IRDS).

Recent studies continue to highlight the dualistic nature of IFNγ, with an increasing body of evidence supporting its protumorigenic role in cancer, underscoring a significant IFNγ paradox within the tumor microenvironment and the host immune response to tumor development. A flurry of recent reports has underscored the protumorigenic role of IFNγ in cancer, bringing the IFNγ paradox to the fore, thereby posing significant implications for the therapeutic targeting of IFNγ in oncology and necessitating an advanced understanding and characterization of its complex role in cancer biology [111 116 117 118 119 120].

AIM OF MY THESIS PROJECT

Accumulating experimental evidence suggests that the emergence of chemoresistance in AML is primarily driven by non-genetic mechanisms, which remain however largely uncharacterized. Leukemia stem cells (LSCs) are considered inherently resistant to cytotoxic drugs [121] and are therefore expected to be enriched following chemotherapy, providing a cellular reservoir for disease relapse [122]. This hypothesis is primarily based on the dormant cell-cycle status of LSCs [123] and is indirectly supported by findings that LSC gene expression signatures in primary leukemias are predictive of relapse [124]. Some studies analyzed samples at diagnosis and relapse and provided evidence that LSCs survive chemotherapy [125]. However, they do not provide a conceptual framework to explain why leukemia relapse is usually chemoresistant, as dormant LSCs must re-enter the cell cycle to repopulate leukemias.

More recently, various laboratories have attempted to characterize AML blasts that survive chemotherapy immediately after treatment (Persistent Blasts). Notably, these studies have not confirmed enrichment of LSCs in cells that survive chemotherapy [126 127 128]. Instead, these studies have shown that primary AML cells enter a senescence-like phenotype following chemotherapy, supported by senescence/inflammatory and embryonic diapause transcriptional programs, with downregulation of MYC and of leukemia stem cell genes. Notably, the authors have demonstrated that these senescence-like phenotypes are reversible, allowing cells to recover and restore the disease. Similar data have been found in solid tumors, where it has been shown that drug-persistent cells share a diapause-like dormancy signature [129]. Many other phenotypic states have been characterized in 'drug-persistent' cells in solid tumors. However, as in the case of AMLs, these drug-persistent cells spontaneously revert to the drug-sensitive state following drug withdrawal, arguing against the possibility that they are involved in the establishment of a therapy-resistant phenotype [130 131 132 133 129 98 134].

One of the limitations in studying mechanisms of chemoresistance establishment in AML is the lack of in vivo models of clinical resistance to standard chemotherapy using human AMLs (PDXs). Available PDX models have primarily focused on the use of Ara-C as a single agent. In these models, leukemias respond to chemotherapy and subsequently relapse. Whether the relapsing leukemias are clinically chemo-resistant, however, was not addressed directly [128 135]. The specific objective of my project is to generate in vivo models

of chemoresistance in human AML for subsequent analyses of genetic and non-genetic mechanisms of therapy resistance.

2. MATERIALS AND METHODS

2.1 AML patient-derived xenograft (PDX) models

2.1.1 Patient samples

Acute Myeloid Leukemia (AML) samples were collected from patient peripheral blood (PB), bone marrow (BM), or other tissues given their consent. Informed consent was obtained from all enrolled patients in compliance with the principles of the World Medical Association Declaration of Helsinki.

2.1.2 Generation of AML PDX models

To produce PDX models, human samples, freshly isolated from patients, were transplanted into murine experimental models, NOD SCID IL2 RG null mice, which were chosen as the optimal model based on their ability to support greater engraftment of human hematopoietic stem cells compared to other models. Successful engraftment was observed in 70% of the mice, while the latency was highly variable among different AML PDX models (showing a range from 4 to 8 weeks before the first visible engraftment).

2.2 Animal experimentation

All experiments including animals were conducted by the Italian Law (Legislative Decrees no. 116/92 and no. 26/2014), which enforces the EU Directives (86/609/EEC of 24 November 1986 and 2010/63/EU of 22 September 2010) on the approximation of laws, regulations and administrative provisions of the Member States regarding the protection of animals used for experimental and other scientific purposes. Mice were housed and taken care of accordingly to the guidelines set out in Commission Recommendation 2007/526/EC - June 18, 2007. At the end of the experiments, all mice were euthanized by inhalation of high concentrations of carbon dioxide (CO_2).

2.2.1 AML Transplantation

In my experiments, I used PDX models already established in the group, as previously mentioned (§3.1). In most cases, 10^6 cells were selected as the optimal

transplantation cell dose. This cell number was chosen to ensure positive engraftment in animals at optimal experimental timing (4-6weeks, depending on the model). AML cells were resuspended in 250 µl of phosphate-buffered saline (PBS and the mixture was kept on ice until transplantation. NSG mice were heated in their cages using infrared light lamps. Upon lateral tail vein dilatation, mice were transferred into lab animal restrainers, where transplantation via lateral tail vein injection was performed. Mice were monitored post-transplantation to ensure their well-being. Most of the animals would experience only mild discomfort during the procedure.

2.2.2 Limiting dilution and serial transplantation assay

Limiting dilution transplantation assays were used for LSC frequency estimation. The general transplantation protocol was used (§3.2.1), however, instead of using a single transplantation dose of 10^6 cells, scalar cell doses of 100, 500, 1,000, and 5,000 cells were used. Cell mixtures were prepared by serial dilution. The final volume for transplantation was 250 µl. Leukemia engraftment was observed 4-6 weeks post-transplantation, depending on the AML model used. All mice were monitored periodically and sacrificed by CO_2 inhalation when they reached 80% engraftment or, in the absence of positive engraftment in PB, at a maximum 6 months post-transplantation. Mice found dead without confirmed leukemia engraftment were excluded from the analysis. LSC frequency calculation was performed by ELDA (extreme limiting dilution analysis; http://bioinf.wehi.edu.au/software/elda/) software.

2.2.3 Engraftment tracking

Weekly bleedings were performed on transplanted mice to follow engraftment over time. NSG mice were heated by infrared light lamps and then transferred to laboratory animal restrainers. After a superficial cut on the tail, blood (35-140 µl) was collected from the lateral vein of the mice, mixed with the appropriate amount of ethylenediaminetetraacetic acid (EDTA; 0.5M, pH 8.0; 15 µl EDTA for 35 µl of blood, or 60 µl EDTA for 140 µl of blood), used as an anticoagulant, and kept on ice till red blood cell (RBC) lysis. A hypotonic solution (8.125 mg/ml NH4Cl, 1 mg/ml KHCO3, 0.13 mM EDTA in dH2O) was used for RBC lysis. In detail, 500 µl of RBC lysis were added to 50 µl of blood/EDTA, and samples were gently mixed by tube inversion and incubated for 10 min at 4 °C. After RBC lysis, cells were labeled with anti-human CD45 antibodies (1:100 dilution in PBS, 1h incubation at 4 °C). Antibodies

used are: humanCD45-APC (for general AMLIEO20 and AML9 models PB, BM and SPL FACS analysis) and humanCD45-BV711 (for IFI6 gene in vivo validation experiments in AMLIEO20 and AML9 models PB, BM and SPL FACS analysis). Analysis of engraftment was performed by flow cytometry (FACS-CelestaTM instrument).

2.2.4 Label retaining assay

To perform in vivo LR assay, two of our PDX models were infected with a lentivirus containing the histone 2B (H2B) – green fluorescent protein (GFP) vector95, which allows division tracking based on the inducible (tet-off) expression system. In absence of doxycycline, H2B-GFP is stably expressed in over 99% of the cells. Once doxycycline is added, it suppresses the expression of H2B-GFP, allowing the distinction of leukemic blasts into quiescent (those which have not divided and retain the full GFP signal, assigned as GFP-high) and proliferating (cells that have divided during the chasing period and, as a result, diluted the GFP signal). Cells that have undergone 1-8 divisions during the chasing period still retain a detectable signal (GFP-low). Cells that have divided more than 8 times lose completely the H2B-GFP-specific signal and become GFP-negative (GFPneg). Doxycycline is given to the mice via modified food pellets at a dose of 625 mg/kg. Chasing started upon visible engraftment (10-30% of human cells) and ended with the end of the experiment.

2.2.5 Chemotherapy treatment

Cytarabine (AraC) is a chemotherapeutical used in the treatment of leukemias and lymphomas. It belongs to the group of antimetabolite drugs, and as a pyrimidine analog, it integrates into the DNA, where it causes DNA replication block, specifically in the S phase of the cell cycle, making it a drug used for rapidly proliferating cells (96 sara thesis). Doxorubicin is part of the anthracycline group of chemotherapeutic agents. Doxorubicin is used to treat multiple cancer types, like soft tissue and bone sarcomas and cancers of the breast, ovary, bladder, and thyroid. It is also used to treat acute lymphoblastic leukemia, acute myeloblastic leukemia, Hodgkin lymphoma, and small cell lung cancer (97 sara thesis). The most commonly used treatment for induction therapy of AML in clinics is “7+3” combined regimen of cytarabine with anthracycline, where AraC is given for 7 days, while anthracycline is given for the first three days of treatment, overlapping with AraC (28,29 sara thesis). In murine models, AraC is used either as a single agent for 5 days or a modified “5+3” combined regimen of AraC and anthracycline is given (98 sara thesis). Both these two

chemotherapy regimens were used in the present study. Single treatment, with AraC only, was given for 5 consecutive days at 100 mg/kg intraperitoneally (IP). Combined treatment included AraC (50 mg/kg for 5 consecutive days IP) and doxorubicin (1.2 mg/kg for three consecutive days IP) with both drugs administered in the first three days of treatment and then AraC alone for the last 2 days. During chemotherapy, mice were monitored and their body mass was followed, in case of worsening of their overall condition or loss of body weight over 20%, mice were sacrificed.

2.2.6 Tissue processing for cell collection

After BM and SPL collection, any remaining fibrous tissue and muscle were removed mechanically from the surface of the bones, and both tissues were mechanically processed, and filtered through a 70 μm cell strainer. Cells were then, either frozen (in freezing media, consisting of 90% South American fetal bovine serum (SA-FBS, Euroclone) and 10% dimethyl sulfoxide (DMSO, Sigma-Aldrich) in a cryobox at – 80 oC) or purified by Ficoll-Paque Plus (GE Healthcare Cytiva Life sciences; 1:1 ratio between Ficoll and sample, centrifugation at 300 x g, 35 min, 16 °C, deceleration off). After centrifugation, the cell ring was collected, and cells were washed with PBS and further used for other procedures.

2.3 Flow cytometry analysis and fluorescence-activated cell sorting

Flow cytometry was used for engraftment and cell cycle analyses. The acquisition was performed on BD FACSCelestaTM instruments. Sorting was performed using BD FACSAriaTM and BD FACSMelodyTM instruments to isolate specific leukemic populations. Sorting was based on the signal of H2B- GFP reporter (GFP-high, -low, -negative) or blue fluorescent protein (BFP) signal (reporter in cells infected with high complexity libraries of expressed barcodes) or RFP signal in case of pRSI17-U6-sh-HTS6-UbiC-tagRFP-2A Puro Plasmid infected cells. Cells were resuspended in presorting media (PBS containing 2% SA- FBS, 2% penicillin/streptomycin (pen/strep) and 2 mM EDTA) at a concentration of 5 x 10^6 per ml. Sorted cells were collected in post-sorting media (RPMI containing 33% North- American FBS (NA-FBS)). Analysis was performed using the FlowJoTM software (BD; version 10.5.2 or higher).

2.3.1 Engraftment analysis

To determine the presence and relative representation of human leukemia cells in the murine PB, BM, and SPL, cells were labeled with anti-human CD45 antibodies. In detail, 106 cells were resuspended in 50 µl of antibody/PBS mix (antibody dilution 1:100) and incubated for 1 hour at 4 °C. Post incubation, cells were washed, fixed in 4% paraformaldehyde (PFA), and acquired by flow cytometry.

2.4 IC50 assay in vitro for chemotherapy drugs

To perform in vitro experiments on H2B-GFP AML PDX models, cells were cultured in RPMI-based media supplemented with 20% North-American FBS (FBS, NA), 1% of 5637 (bladder carcinoma cell line)-conditioned medium (5637 CM), and 2% pen/strep, and incubated in 37 °C 5% CO_2 incubators.

The half maximal inhibitory concentration (IC50) assay is an in vitro assay that calculates the concentration of a drug needed to cause 50% inhibition of a certain biological function or component. The IC50 assay was used in the present study to compare the effect of chemotherapy drugs (AraC and doxorubicin as single agents) on previously chemotherapy treated versus previously nontreated cells. A linearity test and growth curve analysis were performed prior to the IC50 assay to select optimal cell concentration.

2.4.1 Linearity test

A linearity test was performed to check which cell concentrations cells still followed linear growth. For this purpose, cells were plated in decreasing concentrations (from 500,000 to 0, diluting 1:2, in triplicates) in 50 µl of media. Cell luminescence was recorded every 24 hours, starting at 0 hours and ending at 72 hours. CellTiter-Glo ® Luminescent Cell Viability Assay kit (Promega) was used to determine cell luminescence. This method allows the estimation of cell numbers based on the luminescence they emit. CellTiter-Glo reagent (50 µl) was added to cells immediately before the acquisition, and cell luminescence was then recorded by GloMax® Plate Reader (Promega).

2.4.2 Growth curve

A growth curve analysis was conducted to follow the doubling time of cells. Concentrations between 1,000 and 10,000 cells in 50 µl of media were used. Cell luminescence was recorded every 24 hours, starting at 0 hours and ending at 72 hours. CellTiter-Glo reagent (50 µl) was

added to cells immediately before the acquisition, and cell luminescence was then recorded by GloMax®.

2.4.3 IC50 assay

Based on the linearity and growth curve tests, 4,000 cells in 50 µl of media were determined as the optimal cell concentration for the IC50 assay. For both AraC and doxorubicin IC50 assays, 4,000 cells were plated per well (96-well plate) in 50 µl of media, in triplicates. Cells were left to rest for 24 hours. For AraC, serial 1:10 dilution was performed starting from a 10mM stock solution until a final concentration of 0.001 nM, while for doxorubicin serial 1:5 dilution started from a 3.67 mM stock concentration up to a final concentration of 0.37 nM. An intermediate 1:100 dilution was prepared for both drugs before the addition to the cells. Cell luminescence was recorded every 24 hours, starting at 0 hours and ending at 72 hours. CellTiter-Glo reagent (50 µl) was added to cells immediately before the acquisition, and cell luminescence was then recorded by GloMax®. IC50 calculation was performed using GraphPad Prism software (version 9.2.0).

2.5 In vivo clonal tracking

Clonal tracking represents the tracking of the progeny of a single cell. Different barcode libraries have been developed to follow individual cells and their progeny. The idea of using molecular identifiers for clonal tracking was first established in the context of genetic analyses: endogenous (e.g. mutations) or exogenous (e.g. short barcoding sequences inserted in the human genome through retroviral or lentiviral transduction) elements would allow the identification of clones with a common cellular origin that could be followed by DNA sequencing. Novel types of clonal tracking approaches have been developed and, for the present study, the 3rd generation lentiviral Perturb-seq Guide Barcodes (GBC) library (Addgene #85968)102,103 was used. The GBC library contains approximately10 x 106 unique barcode sequences (18-nucleotide long), which can be expressed and followed by single-cell RNA sequencing, as well as puromycin resistance (PuroR) selection marker and the BFP fluorescence reporter. The experimental strategy consists in stably integrating unique Perturb-seq vector GBC barcodes in individual LSCs, whose progeny can then be followed by GBC barcode expression.

2.5.1 Lentivirus production- Packaging cell line and plasmids

The cell line of choice for viral transfection was HEK293T, also known as the 293 T cell line, derived from the human primary embryonic kidney 293 cell line. 293T cells are commonly used for lentiviral production due to their high transfection efficiency. 293T cells were cultured in DMEM (Lonza) supplemented with 10% FBS, SA (Microgem), 2 mM L-Glutamine (Lonza), 100 U/ml penicillin, and 100 U/ml streptomycin (Pen/Strep stock, Lonza).

To produce 3rd generation lentiviral particles, the following plasmids were used:

• pMD2.G VSV.G (Addgene #12259): encoding the G protein of vesicular stomatitis virus (VSV-G)

• pMDLg/RRE (Addgene #12251): encoding the gag and pol coding sequences and HIV-1 Responsive element (RRE)

• pRSV-REV (Addgene #12253): encoding HIV-1 Rev shuttle protein

• pBA571(Addgene #85968): containing 18 nucleotides-long barcode, BFP sequence and PuroR gene

2.5.2 Packaging plasmid DNA amplification and purification (maxiprep)

Top10 competent cells were used for packaging plasmid production. For the transformation, 100 ng (2 μl) of plasmid were added to the cells and the mixture was placed on ice for 2 min, then heat-shocked at 42 °C for 45 seconds, and then put back on the ice for an additional 2 min. Luria-Bertani (LB) medium (250 μl) was added to the mix and cells were incubated for 20-30 min at 37 °C, shaking at 180 rpm. 50 μl of the solution was spread on LB agar plates with a selection antibiotic and the cells were left to grow overnight. The next morning, single colonies were selected, put in 3 ml of LB medium with ampicillin (500x), and left shaking at 180 rpm at 37 °C for 8 hours. After incubation,1 ml of the pre- culture was transferred to 500 ml of LB medium with ampicillin (500x) and left shaking at 180 rpm at 37 °C overnight. NucleoBond® Xtra Maxi kit (MACHEREY-NAGEL) was used for plasmid DNA purification from bacterial cultures according to the manufacturer's instructions. Cells were resuspended, lysed, and subsequently neutralized with appropriate buffers. Lysates, containing the plasmid DNA, were then transferred to a NucleoBond® Xtra Column, included in the kit, and cleared by the specially designed column filter. Next, plasmid DNA was bound to the NucleoBond® Xtra Silica Resin and, after a washing step, eluted in a high-salt concentration buffer. DNA was precipitated with the addition of isopropanol and the

pellet re-dissolved in a low volume of dH_2O. Finally, purified plasmids were quantified on the NanoDrop 1,000 spectrophotometer (Thermo Scientific).

2.5.3 Transient transfection of 293T cells

To produce GBC libraries, a modified Packaging protocol for pooled lentiviral shRNA libraries (Cellecta) was used, adapted for 3rd generation vectors and 10 cm plates. Low passage 293 T cells were seeded in 10 cm plates to obtain sub-confluent (70-80%) cultures. Cells were kept in DMEM media supplemented with glutamine and 10% FBS without antibiotics. For each 10 cm plate the following mixes were prepared:

Mix1:
• pMD2.G VSV.G: 3µg
• pMDLg/RRE: 6µg
• pRSV-REV: 4µg
• pBA571: 2.66 µg
• PlusTM Reagent: 26.6 µl
• DMEM: 533 µl

Mix 2
• LipofectamineTM: 40 µl
• DMEM: 533µl

Mix 1 and Mix 2 were incubated for 15 minutes at room temperature, and then mixed, and incubated for another 15 minutes at room temperature. The mix was then added to the cells, which were then incubated at 37 °C for 24 hours. The virus was collected 24 and 48 hours later, filtered through a 0.22 µl filter unit, and concentrated 1,000x by ultracentrifugation at 53,550 x g, for 2 hours at 16 °C. Virus was then diluted in PBS and stored at -80 °C.

2.5.4 Virus titration

To determine the virus titer, 293T cells were infected with serial dilutions of the frozen virus stock. Cells were plated at a concentration of 2 x 105 cells/ ml in 1 ml of medium per well in a 12-well plate. Amounts of virus added were 1 µl, 0.1 µl, 0.01 µl, 0.001 µl, and 0.0001 µl (in duplicates). Cells were collected 72 hours after infection, fixed with 4% PFA, washed, and resuspended in PBS for FACS acquisition. Titer was calculated by the following

formula, taking into consideration virus dilutions that infected between 1% and 20% of the cells:

$$Viral\,Titer\left(\frac{particles}{\mu l}\right) = \frac{Number\ of\ plated\ cells \cdot \%\ of\ infected\ cells}{Volume\ of\ viral\ suspension(\mu l)}$$

2.5.5 Infection of human AML PDX models

Freshly isolated AML cells were plated at a density of 106 cells per ml in a 24-well plate precoated with Retronectin (Takara Bio). AML culture media was supplemented with polybrene (Sigma) at a final concentration of 8 μg/ml. 2 million viral particles were added per well to achieve an MOI 1 which ensures a good infection efficiency within the limits of the single-integration per cell requirement for clonal tracking experiments. The spin infection was performed at 435 x g, 45 min, room temperature (RT), after which cells were left to incubate for 16 hours. After incubation, half of the cells (5 x 105 cells) were transplanted into NSG mice, while the other half was frozen for DNA sequencing as a reference sample.

2.6 Single-cell RNA sequencing (scRNAseq)

2.6.1 Sample preparation for scRNAseq

Some samples were submitted as bulk population, while some were sorted for subpopulations (GFP-high). After sorting, samples were counted and resuspended in 100 μl of 0.04 % bovine serum albumin in PBS (BSA/PBS), centrifuged, the supernatant was removed and cells were resuspended in an appropriate volume of 0.04 % BSA/PBS (volume was decided based on the target number of cells to be sequenced and the corresponding optimal concentration of cells, based on 10x Genomics guidelines). Cells were counted again, taking note of the percentage of alive cells, and submitted for sequencing. For gene expression matrices processing, clustering, and visualization, sample cleaned GE matrices were log-normalized with the scran method, subset for common genes, and concatenated together. Hypervariable genes (HVG) were selected for each sample as top 5,000 genes ranked for their biological variation component after mean-variance trend modeling using the modelGeneVar() function from scran. After union of each of these sets, the top 2,000 occurring genes were used to subset the concatenated log-normalized matrix. Unwanted technical (number of UMIs and mitochondrial percentage) and biological (only in the alternate “no cc” workflow) sources of variation were regressed out from log-normalized

expression values with the sc.tl.regressOut() function from scanpy. Dimensionality was then reduced with principal component analysis (PCA). Batch (i.e., sequencing run) correction was performed using the Harmony algorithm. The resulting cell embeddings were finally used to construct the Shared Nearest-Neighbors graph that fed Louvain clustering.

2.6.2 Library preparation and sequencing

On average, 2,000-10,000 cells per sample were used for sequencing. Cells were processed and libraries were prepared with Chromium Single Cell 3' Reagent kit v2 (10x Genomics), Chromium Single Cell 3' Reagent kit v3 (10x Genomics), or Chromium Next GEM Single Cell 3' Reagent kit v3.1 (10x Genomics). Paired-end sequencing at high coverage (50,000 reads per cell) was performed on Illumina NovaSeq 6000 platform.

2.6.3 GBC library barcode amplification

Barcode amplification was required as an additional step for the clonal tracking analysis with the GBC library. A small aliquot of the cDNA PCR2 product prepared with the Chromium Single Cell 3' Reagent kits was used for this purpose. PCR1 product of the Chromium Single Cell 3' Reagent kits protocol contained the barcoded (10xBarcode, unique molecular identifier), full-length cDNA, attached to Illumina TruSeq Read1 and poly(dT) sequence while PCR2 product contained also Illumina TruSeq Read2 and P5 and P7 adaptors used in Illumina bridge amplification. Barcode enrichment was then used to specifically amplify barcode sequences. The amplified barcodes were then mixed with their respective samples and scRNAseq was performed. To perform barcode amplification, two rounds of PCR were performed, using semi-nested primers, which contained sequences complementary to the immobilized primers necessary to initiate amplification in the Illumina NovaSeq 6000 platform (Table 1).

Table 1 Primers used for barcode amplification and sequencing

Application	**Round**	**Name**	**Sequence**
Barcode amplification	1st	FWTTA5	AATGATACGGCGACCACCGAGATCTAC ACATAGATGCTCACACTCTTTCCCTACA CGACGCTCTTCCGATCT

		FWTTA6	AATGATACGGCGACCACCGAGATCTAC ACGAAGTTAGGGACACTCTTTCCCTAC ACGACGCTCTTCCGATCT
		FWTTA7	AATGATACGGCGACCACCGAGATCTAC ACAAAGGTAGTAACACTCTTTCCCTAC ACGACGCTCTTCCGATCT
		Reverse_SI-GA-G3	CAAGCAGAAGACGGCATACGAGATGA ATGAGGGTGACTGGAGTTCAGACGTGT GCTCTTCCGATCTTAGCAAAACTGGGG CACAAG
Barcode amplification	2nd	FWTTA5	AATGATACGGCGACCACCGAGATCTAC ACATAGATGCTCACACTCTTTCCCTACA CGACGCTCTTCCGATCT
		FWTTA6	AATGATACGGCGACCACCGAGATCTAC ACGAAGTTAGGGACACTCTTTCCCTAC ACGACGCTCTTCCGATCT
		FWTTA7	AATGATACGGCGACCACCGAGATCTAC ACAAAGGTAGTAACACTCTTTCCCTAC ACGACGCTCTTCCGATCT
		RVTA5	CAAGCAGAAGACGGCATACGAGATGTA GCCCTGTGTGACTGGAGTTCAGACGTG TGCTCTTCCGATCTTAGCAAACTGGGGC ACAAGC
		RVTA6	CAAGCAGAAGACGGCATACGAGATTAA CGCGTGAGTGACTGGAGTTCAGACGTG TGCTCTTCCGATCTTAGCAAACTGGGGC ACAAGC
		RVTA7	CAAGCAGAAGACGGCATACGAGATTCC CAAGGGTGTGACTGGAGTTCAGACGTG TGCTCTTCCGATCTTAGCAAACTGGGGC ACAAGC
Sequencing		PE Read 1 Sequencing Primer	ACACTCTTTCCCTACACGACGCTCTTCC GATCT

		PE Read 2 Sequencing Primer	CGGTCTCGGCA TTCCTGCTGAACCGCTC TTCCGATCT

The first round of PCR served to specifically select barcode sequences and distinguish them from genomic DNA, and to replace adaptor sequences at the ends of each read. Primers used for the first round of PCR contained the P5 (FWTTA5, FWTTA6, FWTTA7) and P7 (Reverse_SI-GA-G3) adaptor sequences for the Illumina flow cell. For the first round of PCR, 5 ng of cDNA was used and a master mix was prepared as described in table 2 below, while thermocycling conditions are reported in table 3.

Table 2 Master mix preparation for PCR1

Component	**Concentration**
NEBNext® UltraTM II Q5® Master Mix	2x
FW primer (10 μM)	0.125 μM
RV primer (10 μM)	0.125 μM
cDNA	5ng
dH2O	(to 30 μl)

Table 3 Thermocycling conditions for PCR 1

Process	**Temperature**	**Time**	**Cycles**
Initial denaturation	98	10 sec	1
Denaturation	98	5 sec	22
Annealing	72	5 sec	
Extension	72	10 sec	
Final extension	72	1 min	1

After the first round of PCR, 10 μl of each sample was analyzed by gel- electrophoresis in order to check if amplicons were of the correct size. Samples were loaded on a 2% agarose gel 1X TAE (1X Tris-acetate-EDTA buffer) and run until amplicon bands were well visible. Following that, samples were diluted 3,000x and 2 μl of diluted sample was used as template for the second round of PCR. The second PCR round has been designed to specifically select

for amplified barcode DNA and discard non-specific PCR products. The primers used for this second amplification contained the double index sequences used for the Illumina sequencing. Master mix for the second round PCR was prepared as described below (Table 4) and thermocycling conditions are described in the Table 5.

Table 4 Master mix preparation for PCR2

Component	**Concentration**
NEBNext® UltraTM II Q5® Master Mix	2x
FW primer (10 μM)	0.125 μM
RV primer (10 μM)	0.125 μM
cDNA	2 μl of diluted PCR1 product
dH2O	(to 30 μl)

Table 5 Thermocycling conditions for PCR2

Process	**Temperature**	**Time**	**Cycles**
Initial denaturation	98	10 sec	1
Denaturation	98	5 sec	20
Annealing	72	5 sec	
Extension	72	10 sec	
Final extension	72	1 min	1

After the second round of PCR, samples were analyzed by gel-electrophoresis in order to check if amplicons were of the correct size. Samples were loaded on a 2% agarose gel 1X TAE (1X Tris-acetate-EDTA buffer) and run until amplicon bands were well visible. PCR products were then purified using the QIAquick PCR purification kit (QIAGEN), according to instructions given by manufacturer. In detail, samples were mixed with high- salt binding buffer, which enables the binding of DNA to silica membrane, while other ingredients, like primers, nucleotides, enzymes, salts, agarose and others, were removed by centrifugation. At the end, DNA was eluted from the silica membrane in a low (30-50 μl volume of water in order to keep the DNA concentrated. DNA quantification was performed on Nanodrop or Qubit.

2.7 GBC library genomic DNA processing

GBC library genomic DNA was used to define the list of GBC barcodes found in each sample, which served as a reference for the analysis of transcriptional profiles of GBC clones. Genomic DNA was extracted from both reference samples (mentioned above) taken at the time of transplantation, as well as BM and PB samples. Spike-in controls were used to assign cell number to read number ratio for each sample.

2.7.1 Spike-in preparation

Separate preparations of Perturb-seq plasmids carrying single barcodes were used to produce virus and to infect NB4 cells. Cells were plated at a density of 5 x 105 cells per ml in media supplemented with 8 μg/ml polybrene and infected with variable MOIs (0.2- 1). Spin infection was performed at 435 x g, 45 min, RT, followed by 16 hours of incubation, after which media was changed and cells were left in a humidified incubator for another 72 hours, to allow for BFP expression. Infected cells were then sorted as BFP+, and aliquots containing predefined numbers of cells were prepared. Different spike-in controls were used to prepare aliquots of 10, 10^2, 10^3, 10^4, 5 x 10^4, 10^5 and 10^6 cells, each of them labeled with a unique barcode. Based on sample cellularity and the expected barcode distribution, an appropriate set of spike-in controls was added to each sample before DNA extraction.

2.7.2 DNA extraction

Cells were resuspended in lysis buffer (10 mM Tris-Cl pH 8.0, 0.5 mM EDTA, 0.2% SDS, 100mM NaCl and 0.1mg/ml proteinase K) and incubated overnight at 55 °C. Temperature was increased to 80 °C for 30min to inactivate proteinase K. Samples were then mixed with 1 volume of isopropanol in order to precipitate DNA and centrifuged at maximum speed (16,000 x g) for 1 hour at 4 °C. Pellets were then washed with 70% ethanol and left to dry. Dry pellets were resuspended in 20 μl of dH2O, and placed in thermomixer, shaking at 1,000 rpm, RT for 30 min for better rehydration. Quantification was performed on Nanodrop or Qubit.

2.7.3 Barcode amplification from genomic DNA

For barcode amplification up to 250 ng of genomic DNA was used as template for a single round of PCR. In case of non-specific amplification (observed after agarose gel-electrophoresis or a Bioanalyzer run), a second round of PCR can be performed. Primers used are shown on table 6 below. Master mix specifications and thermocycling conditions are shown on tables 7 and 8.

Table 6 Primers used for barcode amplification and sequencing

Application	**Name**	**Sequence**
Barcode amplification	F1	GGGTTTAAACGGGCCCTCTA
	R2	GGGAGCCA TCTGA TCGCAAA
Sequencing	PE Read 1 Sequencing Primer	ACACTCTTTCCCTACACGACG CTCTTCCGATCT
	PE Read 2 Sequencing Primer	CGGTCTCGGCA TTCCTGCTGA ACCGCTCTTCCGATCT

Table 7 Master mix preparation for PCR

Component	**Concentration**
NEBNext® UltraTM II Q5® Master Mix	2x
F1 new (10 μM)	0.125 μM
R2 new (10 μM)	0.125 μM
DNA template	200 – 300 ng
dH2O	(to 15 μl)

Table 8 Thermocycling conditions for PCR

Process	**Temperature**	**Time**	**Cycles**
Initial denaturation	98	30 sec	1
Denaturation	98	7 sec	30
Annealing	64	25 sec	
Extension	72	15 sec	
Final extension	72	1 min	1

In samples which had low DNA concentration, total DNA was split in 2 reactions. After the first round of PCR, all reactions per sample were mixed, and 10 μl of each sample was analyzed by gel-electrophoresis in order to check if amplicons are of the correct size. Samples were loaded on 2% agarose gel 1X TAE (1X Tris-acetate-EDTA buffer) and run until amplicon bands were well visible. PCR products were then purified using QIAquick PCR purification kit (QIAGEN), according to instructions given by manufacturer. In detail, samples were mixed with high-salt binding buffer, which enable binding of DNA to silica membrane, while other ingredients, like primers, nucleotides, enzymes, salts, agarose and other, are removed by centrifugation. In the end, DNA was detached from silica membrane by the addition of low-salt elution buffer or water. A small elution volume (30-50 μl) was used in order to keep the DNA content concentrated. DNA quantification was performed on Nanodrop or Qubit. Finally, the presence of a single 240bp band was confirmed on the Bioanalyzer (Agilent).

2.7.4 DNA sequencing

On average, 1-5 ng of amplicon DNA per sample were used for library preparation following the HT-ChIP-Seq Library preparation protocol. Paired-end sequencing with high coverage (30 x 106 reads per sample) was performed on the NovaSeq 6000 platform.

2.7.5 Barcode distribution analysis

The first step was to distinguish real barcode sequences from barcode sequences which were found as a consequence of sequencing error. 93% of total reads was selected as real barcodes, while 7% was excluded. This percentage was selected empirically, based on the expected numbers of barcodes in samples and references. We then used the number of cells that supported any GBC to derive the relative frequency of that GBC in the population. The relative frequencies were binned, and the binning size was determined by taking advantage of the Freedman-Diaconis rule as:

$$Binning\ size = 2 \cdot \frac{IQR}{\sqrt[3]{n}}$$

where IQR is the interquartile range of relative frequencies and n is the total number of different GBCs. We determined the number of GBCs that belonged to each bin and derived the distribution of GBCs in bins.

2.8 Cloning of shRNAs in pRSI16-U6-sh-HTS6-UbiC-TagRFP-2A-Puro Plasmid

Candidate genes for reverse genetics validation experiments were chosen as described in the Results section. For each shRNA two different copies of complementary oligonucleotides (sense and antisense strand) were ordered from SIGMA Aldrich. Sequences were either derived from the pre-existing literature or designed through the tool Genetic Perturbation Platform (GPP) Web Portal (https://portals.broadinstitute.org/gpp/public/). Sequences for selected candidates are reported in Table 9 (forward and reverse oligonucleotides).

Table 9 List of forward and reverse oligonucleotides cloned in pRSI17-U6-sh-HTS6-UbiC-tagRFP-2A Puro Plasmid validation

Gene	Sequence (Forward and Reverse)
IFI6_1	ACCGG**GAGATGGGTTCTCACTATATT**GTTAATATTCATAGC**AATATAGTGAGAACCCATCTC**TTTT CGAAAAAA**GAGATGGGTTCTCACTATATT**GCTATGAATATTAAC**AATATAGTGAGAACCCATCTC**C
IFI6_2	ACCGG**CAACCTCCCAAGTAGGATTAC**GTTAATATTCATAGC**GTAATCCTACTTGGGAGGTTG**TTTT CGAAAAAA**CAACCTCCCAAGTAGGATTAC**GCTATGAATATTAAC**GTAATCCTACTTGGGAGGTTG**C

All the sequences contain two 21 nucleotide sequences specific for the shRNA (in bold, forward, and reverse orientations) separated by a hairpin loop sequence (in red).

The forward and reverse complementary oligonucleotides were diluted to a final concentration of 20µM and mixed in a 1:1 ratio. Phosphorylation and annealing reactions were performed in 20µl of 1X T4 Polynucleotide Kinase Buffer. 10 units of T4 Polynucleotide Kinase were added to the mix and the solution was incubated for 30 minutes at 37°C to allow phosphorylation. Then, the reaction was heated to 95°C for 2 minutes to disrupt secondary structures within oligonucleotides. Ultimately, the mix was cooled down gradually to room temperature to allow sense and antisense strands to anneal.

Annealed oligonucleotides were diluted 1:10 in 1X T4 Polynucleotide Kinase Buffer and ligation was performed in 10µl of 1X T4 DNA Ligase Buffer. 1µl of annealed and diluted oligonucleotides were mixed with 40 units of T4 DNA Ligase and 1µl of pRSI16-U6-sh-HTS6-UbiC-TagRFP-2A-Puro Plasmid. The reaction was stored at room temperature for 4 hours protected from light. After ligation, the reaction was used to transform Stbl3 bacteria by heat shock as previously described. Ultimately, 100µl of cell suspension were plated on selection plate (Agar + 50 mg/L ampicillin) and incubated overnight at 37°C. The day after 3 colonies were picked and grown overnight, to perform DNA extraction. For DNA extraction, we used NucleoBond Xtra Maxi (Macherey-Nagel) kit according to the volume of growth and the manufacturer's instructions.

Plasmids were Sanger-sequenced to check the quality of both ligation and sequence. Then, the plasmids were used to produce lentiviral particles as previously described. As a control for all the experiments, a pRSI17-U6-sh-HTS6-UbiC-TagRFP-2A-Puro Plasmid containing the following scrambled sequence was used.

Gene	Sequence (Forward and Reverse)
Scrambled	ACCGG**GCCGTCGTAAATTGTCGTGGC**GTTAATATTCATAGC**GCCGCGACAATTTGCGACGGC**TTT CGAAAAAA**GCCGTCGTAAATTGTCGTGGC**GCTATGAATATTAAC**GCCGCGACAATTTGCGACGGC**CC

Finally, we infected AMLIEO20 and AML9 cells with a gene-targeting construct or with the scrambled construct. Infected cells underwent puromycin selection for 72 hours and were grown for additional 4 days to allow a stable knock-down. We extracted the RNA with the Quick-RNATM Miniprep Kit (Zymo Research) and generated complementary cDNA with the ImProm-IITM Reverse Transcription System (Promega) according to manufacturer instructions. The extent of knock-down was assessed by qPCR, by comparing the cells expressing the shRNA against the target gene with the cells expressing the scrambled sequence.

2.8.1 RNA reverse-transcription and pPCR

Total RNA was subjected to reverse transcription as follows: 1µg of total RNA in 29 µl of H2O was mixed with 1.25 µl of Random hexamers (500 ng/µl) and incubated at 70°C for 5 min in the thermocycler. Then the reverse transcription mixture was added according to the Table 10 and the following program was used: 25 °C 5 min, 42°C 60 min, 72°C 15 min.

Table 10 Components of the retro-transcription reaction

Component	Amount per reaction, µl
ImProm-II™ 5X Reaction Buffer (Promega)	10
$MgCl_2$, 25 mM	5
dNTPs, 10 mM	2,5
RNAse inhibitor	1,25
ImProm-II™ Reverse Transcriptase (Promega)	1

For gene expression analysis, qPCR was performed using ~20 ng of cDNA in a 96-well plate as described in Table 11.

Table 11 Components of qPCR reactions

Component	**Amount, µl**
2X FAST SYBR™ Green Master Mix	10
Primer mix (Forward + Reverse), 10 µM	0,6
Template cDNA	5
Nuclease-free water	to 20

Fluorescence accumulation during qPCR was detected on Viia7 Real-Time PCR System machine (Thermofisher). Relative mRNA quantification was performed by the comparative ΔΔCt method using Gusb for normalization. Primers used are listed in Table 12.

Table 12 qPCR primers used to check gene silencing

Primer name	**Sequence**
IFI6 forward	GATGAGCTGGTCTGCGATCC
IFI6 reverse	TCGAGATACTTGTGGGTGGC
GUSB forward	CAACTTAAGGTGCCAGGTGTC
GUSB reverse	GTGACGTCTGTGCAGTCAGC

2.8.2 Target validation in mouse

AMLIEO20 and AML9 blasts were infected with pRSI17-U6-sh-HTS6-UbiC-TagRFP-2A-Puro Plasmid cloned with the gene of interest or with the scrambled sequence. Cells underwent puromycin selection for 72 hours to allow a stable knock-down of the gene of interest. Per each mouse, 1,000,000 AMLIEO20 and AML9 blasts were resuspended in 250 µl of PBS and injected in the lateral caudal vein of 8-12 week old NSG recipient mice. Tumor growth was weekly monitored by peripheral blood FACS analysis (as described above). Per each cohort of mice, a part of them were non chemo treated and a part were treated with chemotherapy as described above. Mice were scarified (CO2 inhalation) when reaching more then 80% of PB engraftment. Bone marrow and spleen were processed and analyzed as described above.

Prior to the transplantation (after the 72 hours of puromycin selection) infected blasts were analyzed at FACS to assess RFP positivity (around 90%) and the knock down efficacy were assessed by RT-qPCR.

2.8.3 Target validation in AML cell lines

GDM1 and U937 cell lines were infected with pRSI17-U6-sh-HTS6-UbiC-TagRFP-2A-Puro Plasmid cloned with the gene of interest or with the scrambled sequence. Cells underwent puromycin selection for 72 hours to allow a stable knock-down of the gene of interest. Infected blasts were counted after puromycin selection, analyzed at FACS to assess RFP positivity and RNA extracted to asses knock down efficacy by RT-qPCR. GDM1 cells were maintained in RPMI medium supplemented with 20% FBS, 100 U/ml penicillin/streptomycin; U937 cells were maintained in RPMI medium supplemented with 10% FBS, 100 U/ml penicillin/streptomycin. GDM1 and U937 cells were cultured at 37°C in a 5% CO_2 controlled atmosphere.

2.8.4 Immunofluorescence of AML cell lines

Untreated cells were seeded on coverslips using Corning® Cell-Tak™ reagent protocol (Catalog No. 354240, 354241). After seeding cells were washed in PBS and fixed in 2% PFA in PBS for 15 minutes at room temperature (RT). After 3 washes in PBS, they were permeabilized using PBS 0,1% saponin, for 1 hour at RT. Cells were then stained with primary antibodies over-night at 4°C. After 3 washes in PBS 0,1% saponin cells were stained with the appropriate secondary antibodies and DAPI (1:5000) for 1 hour at RT. After 2 washes in PBS 0,1% saponin and 1 wash in ddH2O, cells were mounted on microscope slides using Mowiol as mounting medium. Then slides were acquired using ….

2.9 Whole exome sequencing

DNA was extracted as described in section 2.6.2 from BM samples of non-chemo, chemo treated and relapse mice. 500ng of extracted DNA were sonicated following Agilent SureSelect^{XT} Low Input Target Enrichment System V7 kit instructions. 200 bp average size of fragmented DNA was checked and assessed by Agilent Bioanalyzer. 50-200 ng of DNA was sequenced. The bioinformatics analysis was performed using the Illumina DRAGEN Bio-IT Platform (version 4.3.6). For Whole Exome Sequencing (WES), DRAGEN was

utilized to produce variant calls, Copy Number Variations (CNVs), and Structural Variants (SVs) in Variant Call Format (VCF) version 4.2. Additionally, DRAGEN estimated Microsatellite Instability (MSI), Homologous Recombination Deficiency (HRD), and Tumor Mutational Burden (TMB) for each tumor sample paired with its matched normal sample.

Subsequently, variants were annotated and prioritized using an open-source software tool (Variantalker version 1.4), which integrates CancerVar, InterVar, Annovar, and RENoVO (version 1.0). The annotation was based on the following public databases

Databases for Germline Samples:

Funcotator 4.5.0.0 | Gencode 43 CANONICAL | ACMGLMMLof 1 | ACMG_recommendation v3.2 | ClinVar_VCF 20231104 | Gencode_XHGNC 110_38 | Gencode_XRefSeq 110_38 | HGNC Nov082023 | LMMKnown 20180618 | dbSNP b156 | gnomAD_exome 2.1

Annovar database_names = refGene, esp6500siv2_all, 1000g2015aug, gnomad_genome, dbscsnv11, rmsk, ensGene, knownGene, avsnp150, dbnsfp42c, clinvar_20231109

Databases for Somatic (Tumor) Samples:

Funcotator 4.5.0.0 | Gencode 43 CANONICAL | Achilles 110303 | CGC full_2012_03-15 | ClinVar_VCF 20231104 | Cosmic v98 | CosmicFusion v98 | CosmicTissue v98 | DNARepairGenes 20230628T135455 | Familial_Cancer_Genes 20110905 | Gencode_XHGNC 110_38 | Gencode_XRefSeq 110_38 | HGNC Nov082023 | Oreganno 20160119 | Simple_Uniprot 2014_12 | dbSNP b156 | gnomAD_exome 2.1

Annovar database_names = refGene, ensGene, knownGene, esp6500siv2_all, 1000g2015aug, exac03, dbscsnv11, dbnsfp31a_interpro, gnomad_genome, avsnp150, dbnsfp42c, icgc28, cosmic98, clinvar_20231109

2.10 Statistical analysis

Data are represented as average ± standard deviation. All statistical tests are reported in the legend of each figure and the corresponding p-values are reported in the legend of each figure or on the figure itself.

Shannon Entropy was used to calculate the complexity of a clonal population. For any given sample j, the formula for Shannon Entropy is:

$$SH_j = -\sum_{i=1}^{N} p_i \cdot \log(p_i)$$

where pi is the frequency of the observation i in a sample composed of N observations. Expansion index was calculated as (1 – Shannon Equitability). Shannon Equitability represents the value of Shannon Entropy (for a given sample) divided by the maximum value that Shannon Entropy can have. Expansion index was used to compute the clonality of a given sample. In particular, for any given sample j, the formula for the expansion index is:

$$Expansion\ index_j = 1 - \frac{-\sum_{i=1}^{N} p_i \cdot \log(p_i)}{logN}$$

where N is the number of observations in the sample j. This index ranges from 0 to 1, where 1 corresponds to a purely monoclonal sample (i.e., N = 1 and pi = 1) and 0 corresponds to a sample composed of N observations with uniform frequency.

To understand which clusters are expanded/depleted in different samples (e.g. before and after chemotherapy), we divided the relative fraction of the cluster in the sample of interest by the relative fraction of the cluster in the baseline sample. Following that log2 fold change (LOG2FC) was calculated from these values. Clusters with positive LOG2FC values were considered as enriched, while clusters with negative LOG2FC values were considered as depleted in the sample of interest.

3 RESULTS

3.1 Generation of two human PDX models of chemoresistant AML

3.1.1 The H2B-GFP AML PDX models

To monitor and isolate quiescent blasts during leukemia growth *in vivo* my lab has incorporated a label-retaining (LR) assay into AML PDX mouse-models, which allows cell-division tracking and is based on the inducible (Tet-Off) expression of the histone 2B (H2B) – green fluorescent protein (GFP). In my experiments, I used two PDX AML PDXs engineered to express the H2B-GFP allele (AML9-H2B-GFP and AMLIEO20-H2B-GFP). After 14 days of *in vivo* chasing of H2B-GFP expression with doxycycline, three cell fractions can be clearly distinguished by FACS analyses, based on the fluorescent GFP signal: GFP^{high} (0 divisions), GFP^{low} (1-8 divisions), and GFP^{neg} (GFP^{neg}, >8 divisions). Mathematical modeling of the H2B- GFP dilution-signal in the BM of AML mice predicted the co-existence of sub-populations with distinct cell cycle properties (Fig. 5): quiescent (non-dividing), slowly proliferating (63.7±28.9 hrs average division interval) and fast proliferating (63.7±28.9 hrs. average division interval) and fast proliferating (41.1±14.3 h average division interval) [136] [137] These populations can be isolated by FACS according to H2B-GFP signal intensity.

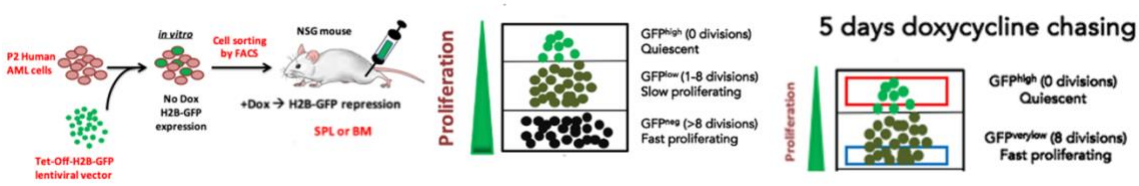

Figure 5. The H2B-GFP AML PDX model system (modified from Vlachou et al. (paper in preparation))

Left panel, Schematic representation of the generation of AML-PDXs expressing H2B-GFP. Center panel. H2B-GFP signal dilution after 2 weeks of doxycycline chasing. Population gating is represented (GFP^{high}- quiescent cells, GFP^{low}- slow proliferating cells (cells which proliferated 1-8 times in 2 weeks), GFP^{neg}- fast proliferating cells (cells which proliferated more than 8 times in 2 weeks). Right panel, 5 days of chasing H2B-GFP dilution in which two principal sub-population can be identified since cells are still not GFP^{neg}: GFP^{high} uniformly quiescent cells and $GFP^{verylow}$ rapidly dividing cells.

3.1.2 Diverse Responses to standard chemotherapy in the two AML Models: From Primary Resistance to Relapse

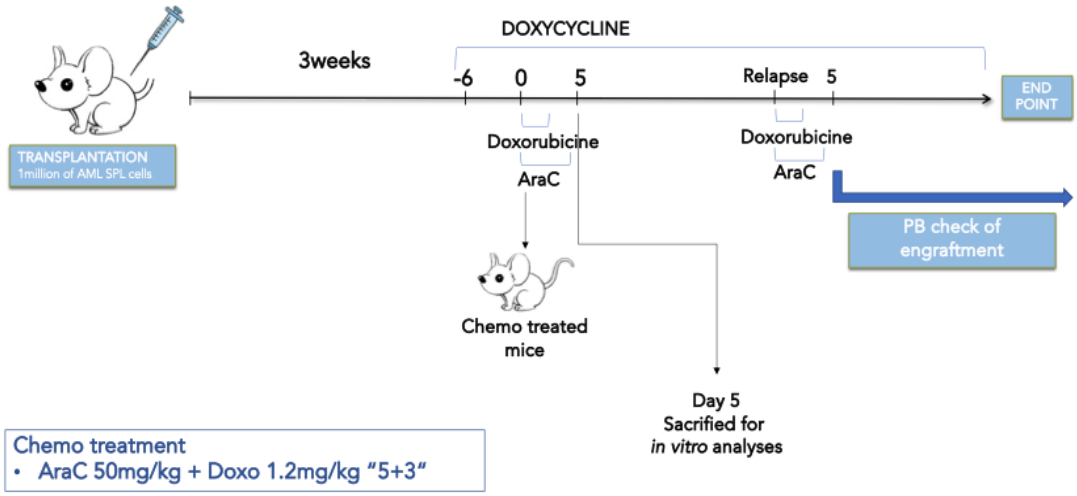

Figure 6 Experimental scheme of chemotherapy treatment for the generation of PDX model of chemoresistance

NSG mice are transplanted with PDX models (AML9 and AMLIEO20 blasts) and upon engraftment in PB (15-20% for AMLIEO20, 2-5% for AML9) doxycycline chasing started. After 5 days of chasing "5+3" chemotherapy regimen was introduced and mice monitored and sacrificed as shown. Sample were collected at different time points (day 0, day 5, relapse). Upon relapse, mice were retreated with the same chemotherapy regimen and followed up by weekly PB withdrawal. Samples for IC50 analysis were collected after the first round of chemotherapy.

To investigate chemosensitivity, I treated the AML9 and AMLIEO20 H2B-GFP AML mouse-lines with a chemotherapy scheme that recapitulates the "*7+3*" AraC + Doxorubicin induction-chemotherapy regimen used in clinics (Figure 6). NSG mice were transplanted with $1x10^6$ million blasts by tail IV injection, placed on doxycycline upon early engraftment detection (to induce H2B chasing) and treated with the *"5+3"* chemotherapy regimen*:* 50 mg/kg AraC intraperitoneally (IP) or intravenously (IV) for 5 consecutive days plus 1.2 mg/kg doxorubicin IP or IV for 3 consecutive days.

The two models showed slightly different latencies of disease appearance: 39 and 35 days to reach 50% engraftment in the PB for the AML9 and AML20, respectively (Figs. 5 and 6). For the AMLIEO20 mice, chemotherapy was started when engraftment reached around 30% CD45+ cells in the PB (Fig. 10) (anti-CD45 antibodies were used to mark human cells). For the AML9 mice, instead, I started treatment with 2-5% engraftment, since I noticed that chemotherapy administration with 30-40% blasts in the PB is highly toxic, with consistent death of mice within the first week after chemotherapy treatment (13 out of 18; 8 out of 9; two independent experiments) (Fig. 7).

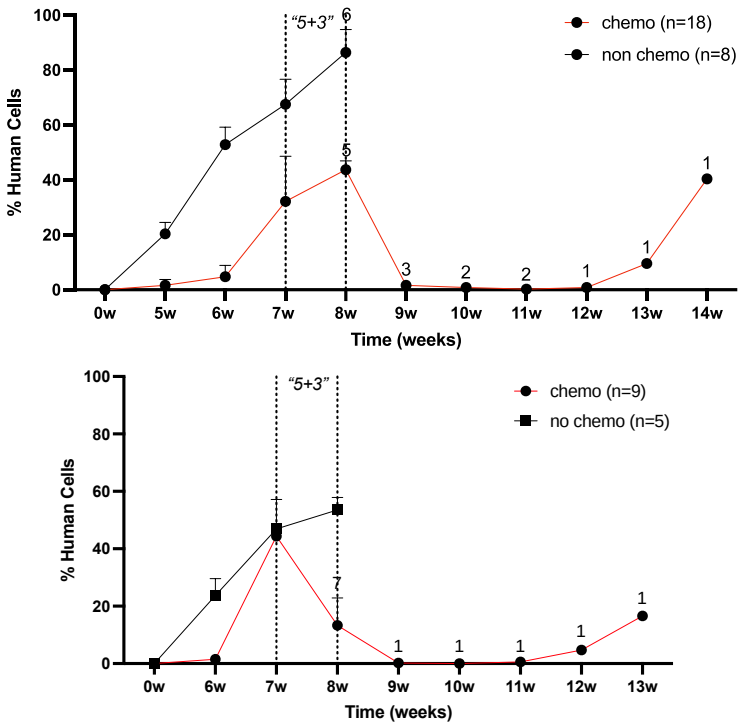

Figure 7 Starting chemotherapy late in PB engraftment leads to consistent death of mice in AML9 PDX model

Average engraftment levels in PB (FACS analysis of CD45 positive cells) of transplanted mice is shown for chemo treated (red line) and non-chemo treated (black line) mice. Dotted lines indicate start and end of chemotherapy treatment. Two independent experiments.

Notably, with 2-5% blasts in the PB (2-5%), the BM is already compromised and heavily infiltrated by human blasts (around 80%) (Fig. 8).

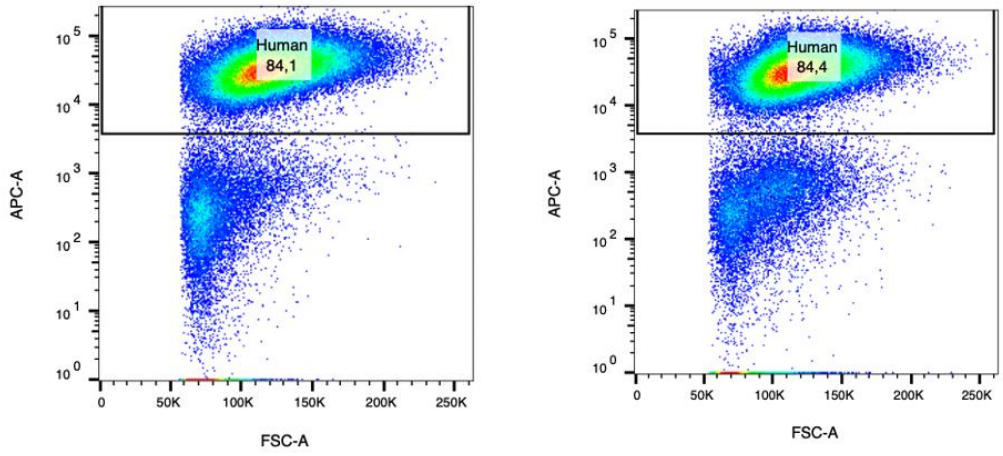

Figure 8 AML9 BMs FACS-analysis of early PB engrafted mice

FACS-analysis of the BM engraftment of two different mice transplanted with AML9 blasts, which had a PB blasts percentage of 2 to 4 % (human anti-CD45-APC antibodies were used to stain BM blasts).

AML9 PDX mice were treated following three different drug schedules of the "5+3" chemotherapy regimen: IV, using standard dose, IV with half of the standard dose and IP with the standard dose. The kinetics of response to therapy were similar across all three treatment schedules: a significant reduction in the percentage of human blasts in the PB (from 2-5% to 0,1%), which remained stable for approximately 2 weeks, followed by a progressive re-expansion of blast numbers starting from the third week after treatment (5-10%), and a frank relapse with >50% blasts around the fifth week after treatment (Fig. 9). Notably, no mortality was observed during the induction phase. In subsequent experiments with this model I used standard chemotherapy dose and IP injection (Fig. 9).

AMLIEO20 PDXs were also treated with the "5+3" regimen, following the standard dose and IP injection schedule, as described above. The kinetics of response to treatment were significantly different compared to the AML9 model (Fig. 10). Indeed, the number of PB human blasts did not change significantly during the 5-day treatment period, and only slightly decreased in the following week (from 70% to 40%), before rapidly re-expanding in the subsequent week to levels comparable to those observed in the untreated animals.

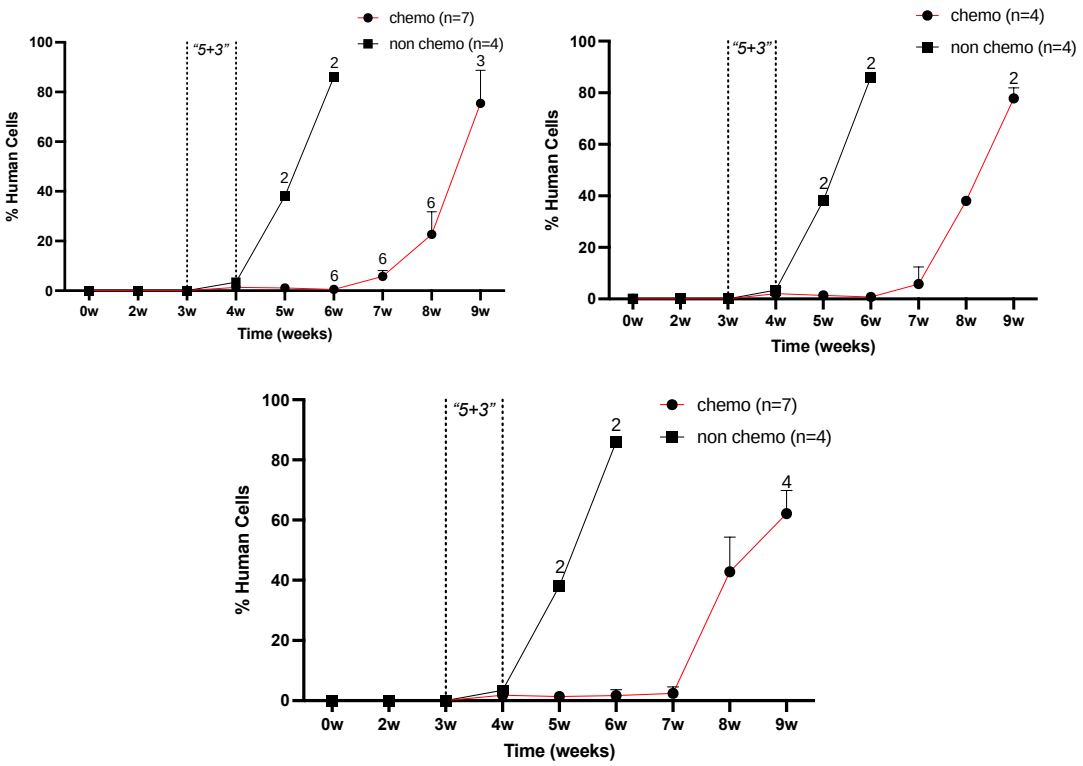

Figure 9 AML9 PDX model of chemoresistance

Average engraftment levels in PB (FACS analysis of CD45 positive cells) of transplanted mice is shown for chemo treated (red line) and non-chemo treated (black line) mice. Dotted lines indicate start and end of chemotherapy treatment. Top left IP standard dose, top right IV standard dose, bottom IV half dose.

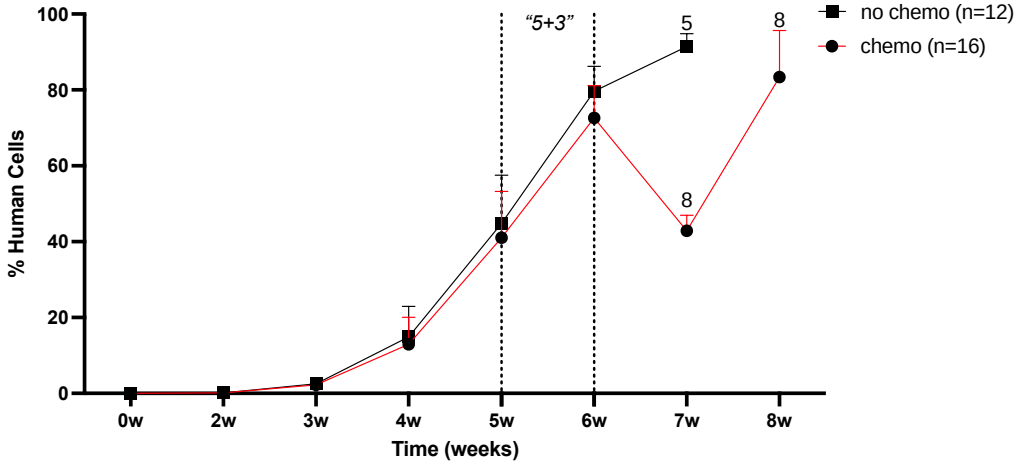

Figure 10 AMLIEO20 PDX model of chemoresistance

Average engraftment levels in PB (FACS analysis of CD45 positive cells) of transplanted mice is shown for chemo treated (red line) and non-chemo treated (black line) mice. Dotted lines indicate start and end of chemotherapy treatment.

I then investigated the levels of blast infiltration in cell suspensions from BM and SPL collected at day 5 (i.e., at the immediate end of the "5+3" chemotherapy regimen), by FACS analysis of CD45-positive cells. In the AML9 model, I observed a dramatic reduction in blast infiltration in both the bone marrow (from >90% to 25%; 4-fold reduction) and the spleen (from 80% to 25%; 3-fold reduction). Consistently, spleen weight decreased from 0.4 to 0.1 g (4-fold reduction) (Fig. 11). The reduction in infiltration was less pronounced in the AMLIEO20 model: from 80% to 60% (1,5-fold decrease) in the BM and from 60% to 40% (1,5-fold reduction) in the spleen, despite a more pronounced reduction in spleen size (from 0.7 g to 0.2 g; 3,5-fold reduction) (Figure 12). Together, these data confirm the observation made by analyzing blast frequencies in the PB; that is, unlike AML9 leukemia, the AMLIEO20 leukemia is partially resistant to chemotherapy.

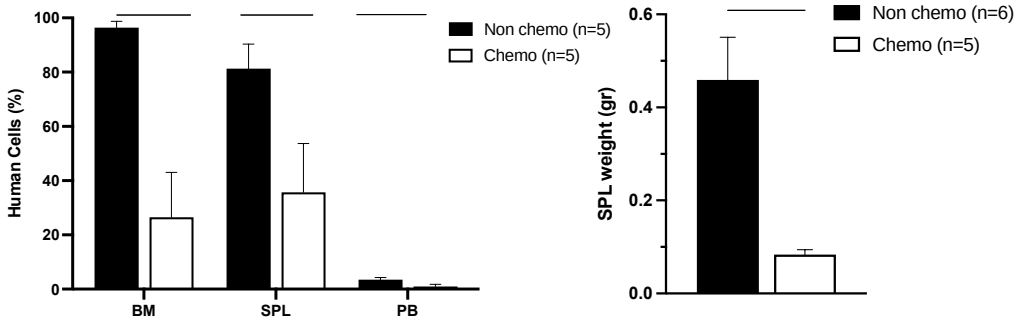

Figure 11. AML9 chemotherapy treated tissue analysis

Average engraftment levels in BM, SPL and PB at the end of chemotherapy (day 5) and SPL weight at day 5 for chemo (light blue) and non-chemotherapy (black) treated mice. Human cells are gated on FACS analysis based on CD45 positive cells. (∗ P < 0.05, and ∗∗ P < 0.01 by Mann-Whitney test). SPL weight is expressed in grams (gr).

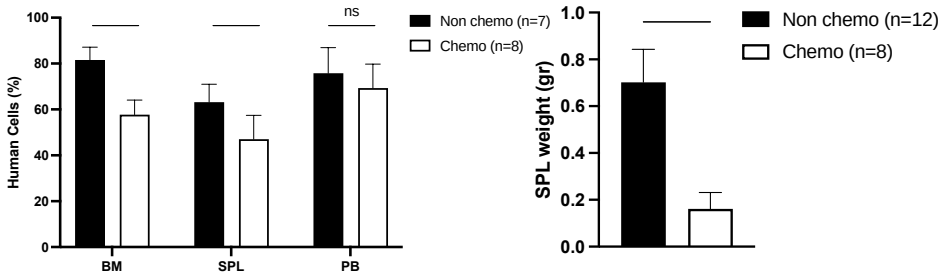

Figure 12 AMLIEO20 chemotherapy treated tissue analysis

Average engraftment levels in BM, SPL and PB at the end of chemotherapy (day 5) and SPL weight at day 5 for chemo (light blue) and non-chemotherapy (black) treated mice. Human cells are gated on FACS analysis based on CD45 positive cells. (ns, not significant, ∗ P < 0.05, ∗∗ P < 0.01, ∗∗∗∗ P < 0.0001 by Mann-Whitney test). SPL weight is expressed in grams (gr).

3.1.3 Treatment with Venetoclax does not affect chemoresistance phenotype

In order to assess whether or not the addition of BH3-mimetics could overcome and interfere with the chemoresistance phenotype in our AML model systems, we also performed an *in vivo* experiment using AMLIEO20 PDX and treating mice with *"5+3"* and Venetoclax.

NSG mice were transplanted with AMLIEO20 blasts and their engraftment in PB was weekly monitored by FACS analyses of CD45 + blasts. Once PB engraftment reached 20-30% CD45+ cells, mice were randomized into 8 treatment groups: control (n=3), *"5+3"* (n=4), *"5+3"* + Venetoclax 25mg/kg (n=4), Venetoclax 25mg/kg only (n=4), *"5+3"* + Venetoclax 50mg/kg (n=4), Venetoclax 50mg/kg only (n=4), *"5+3"* + Venetoclax 75mg/kg (n=4), Venetoclax 75mg/kg only (n=4). Venetoclax was administered intravenously for 5 consecutive days followed by two days of treatment discontinuation, for 3 weeks, resulting in a total of 15 days of treatment regimen. Mice were monitored weekly for frequency of PB blasts.

As expected, *"5+3"* chemotherapy regimen induced a temporary reduction in PB blasts, followed by a frank re-expansion of the disease with similar kinetics to untreated leukemia. Venetoclax treatment alone or in combination with the *"5+3",* resulted a similar response compared to *"5+3"* only, regardless of the tested doses (Figure 13 top panels). The highest tested dose of Venetoclax treatment (75mg/kg) in combination with *"5+3",* resulted in a consistent death of mice, due to toxicity induced by the drug combination (Figure 13 bottom panel).

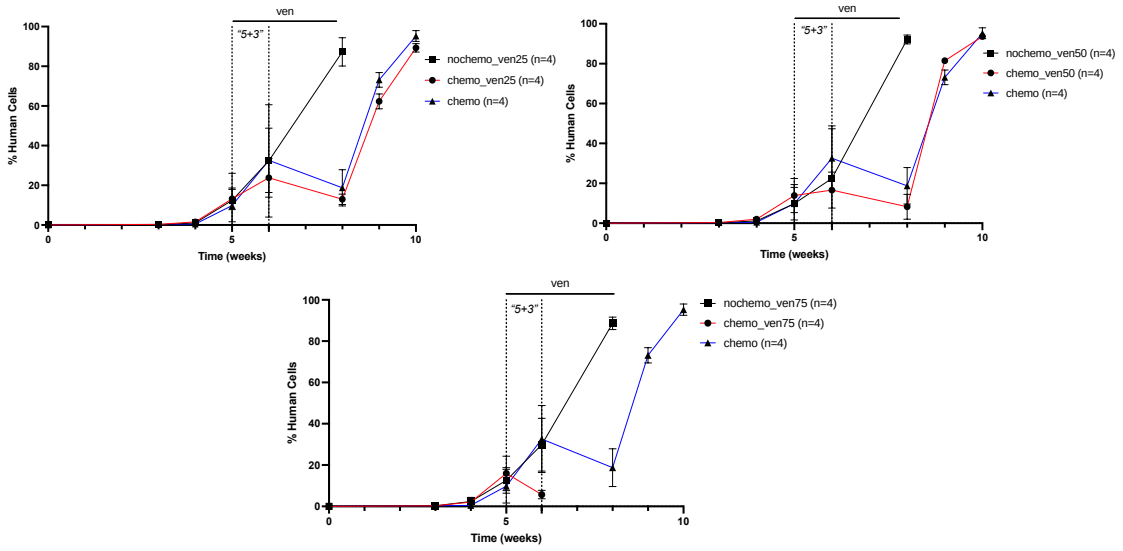

Figure 13 Venetoclax treatment does not modify chemoresistance phenotype in AMLIEO20

Average weekly PB engraftment based in FACS analyses (human CD45 antibody). Black lines, control mice; red lines chemotherapy treated mice; blue lines chemo + Venetoclax (25mg/kg top left, 50mg/kg top right, 75mg/kg bottom), treated mice. Dotted lines indicate start and end of chemotherapy treatment, Venetoclax treatment (IV) 5 consecutive days plus two day of discontinuation for 3 weeks (for a total of 15 days of treatment).

These findings suggest that the addition of a BH3-mimetic, such as Venetoclax, to the *"5+3"* chemotherapy regimen, does not alter the chemoresistance phenotype *("5+3")* and does not modify leukemia growth.

3.1.4 In both AML models the relapsed leukemias are clinically chemoresistant

The primary cause of mortality in AML remains the failure of salvage therapies in refractory AMLs and in AMLs that relapse after the initial clinical remission induced by chemotherapy, usually the 3+7 regimen. Clinical evidence suggests that disease relapsing after chemotherapy is chemoresistant. For instance, in a recent study conducted on a large cohort of AML patients, it was observed that complete remission rates decreased from 14% after first salvage therapy to 9% after second salvage therapy and 3% after third salvage therapy [138]. Notably, a large fraction of these patients had been treated with chemotherapy regimens containing high doses of Ara-C. I have therefore analyzed whether the clinical relapse in my two mouse models of refractory/relapsing AML was clinically chemoresistant.

To evaluate the sensitivity/resistance of relapsing blasts *in vivo*, I re-treated mice with a second round of *"5+3"* chemotherapy regimen at relapse (at week 7 or 8 for AML9 and AMLIEO20, respectively) and monitored the frequency of human blasts in the PB, by FACS-analyses using the anti-CD45 antibody. In AMLIEO20 PDX model, after the second round of *"5+3"* chemotherapy treatment, I observed no significant reduction of CD45+ blasts in the PB (Fig. 14; upper panel). In particular, 2 mouse out of 3 were completely refractory to treatment, while 1 showed slight reduction of PB blasts. All mice died at approximately the same time (17-20 days post chemotherapy) and showed massive splenomegaly and organ infiltration at necroscopy (data not shown).

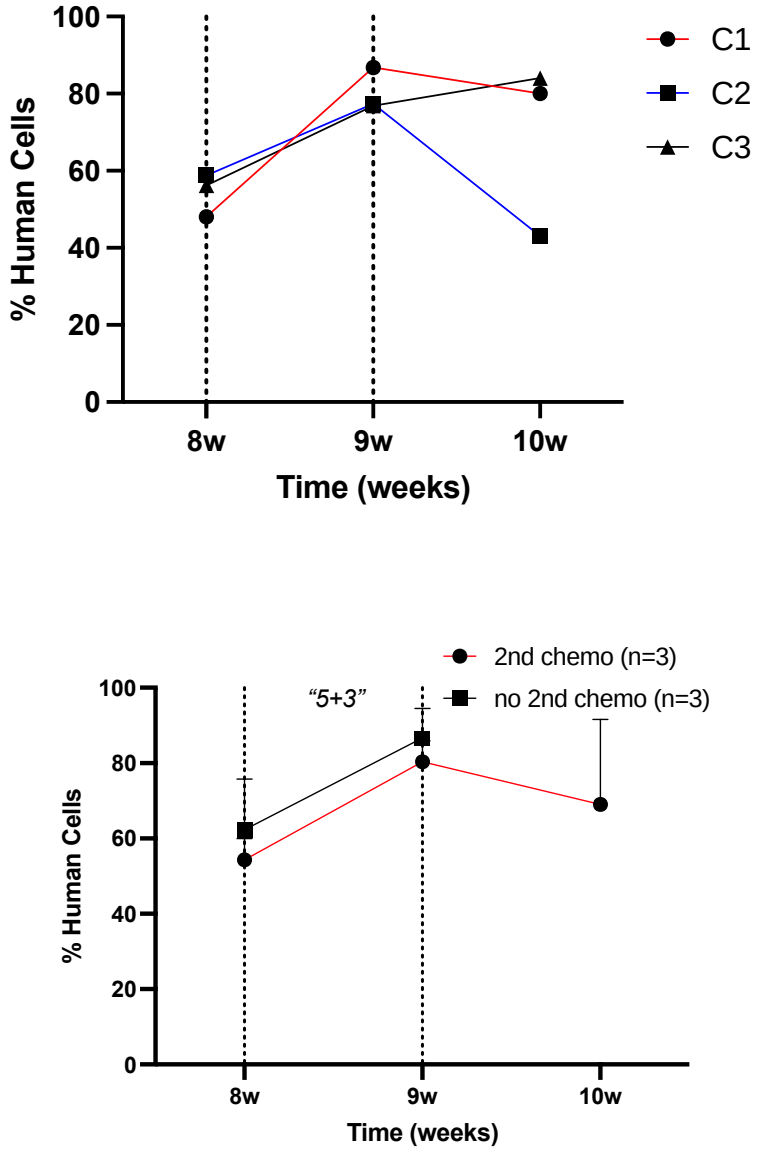

Figure 14 AMLIEO20 relapsed leukemias are chemoresistant in vivo

Upper Panel: average engraftment levels in PB of AMLIEO20 mice after a second round of "5+3" chemotherapy treatment. Mice harbor a relapsed leukemia after an initial cycle of 5+3 chemotherapy. Engraftment was measured by FACS-analyses of PB mononuclear cells using the anti-CD45 antibody (% Human cells) at the indicated time-points (w: weeks). Chemo-retreaded mice are shown in red, non-chemo-retreated mice are shown in black. Dotted lines indicate start and end of chemotherapy retreatment, left. Lower Panel: PB engraftment of single retreated mouse (C1, C2, C3) from the same experiment of the Upper Panel.

AML9 relapsed leukemias were also re-treated with the *"5+3"* regimen, following three different schedules (IV, using standard dose, IV with half of the standard dose and IP with the standard dose). As shown in Fig. 15, relapsed leukemias were completely refractory to chemotherapy, regardless of the treatment schedule, and all died within 1-4 weeks after treatment. To verify the stability of the chemoresistant phenotype, AMLIEO20 leukemias were collected at relapse after the first cycle of chemotherapy and transplanted into recipient

NSG mice. When engraftment reached approximately 20% in the peripheral blood (PB), mice were treated with the *"5+3"* chemotherapy regimen. Strikingly, no effect on the frequency of PB blasts was observed in any of the treated mice. All mice died within 7 weeks from treatment and showed signs of infiltrating disease at necropsy (data not shown). In conclusion, in both AML models, relapsed leukemia after one cycle of chemotherapy is clinically resistant to re-treatment with the same therapy.

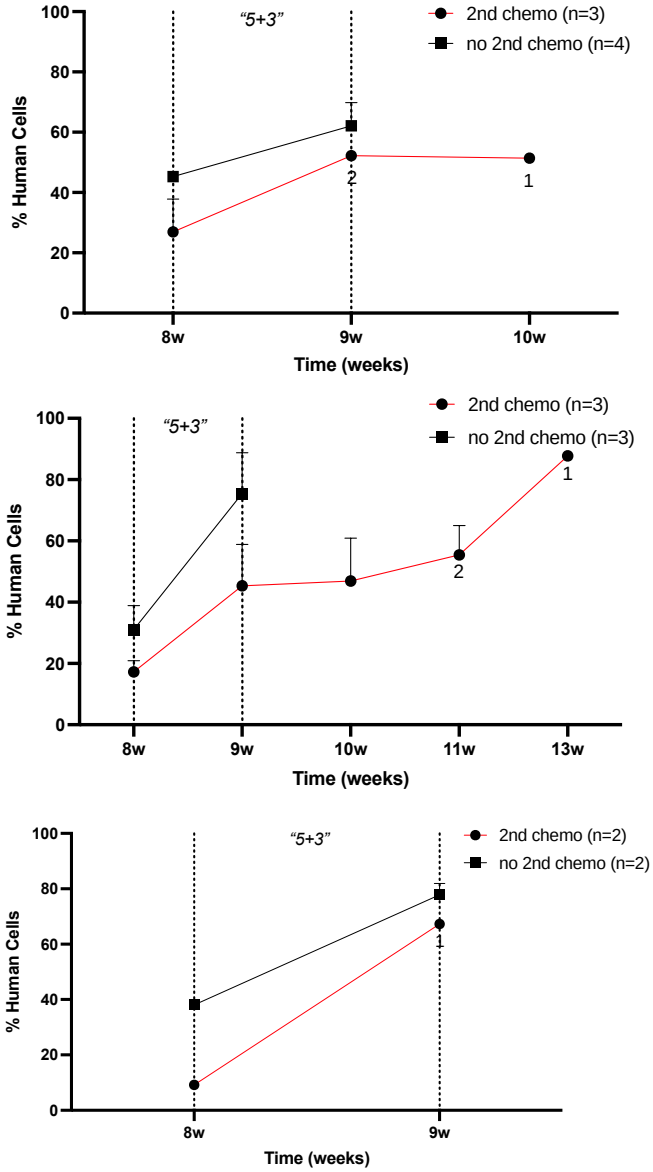

Figure 15 AML9 relapsed leukemias are chemoresistant in vivo

Average engraftment levels in PB of AML9 mice after a second round of "5+3" chemotherapy treatment. Mice harbor a relapsed leukemia after an initial cycle of 5+3 chemotherapy. Mice were treated with different schedules of the "5+3" regimen: IV, using standard dose (Upper Panel), IV with half of the standard dose (Middle Panel) and IP with the standard dose (Lower Panel). Engraftment was measured by FACS-analyses of PB mononuclear cells using the anti-CD44 antibody (% Human cells) at the indicated time-points (w: weeks). Chemo-retreaded mice are shown in red, non-chemo-retreated mice are shown in black. Dotted lines indicate start and end of chemotherapy retreatment.

3.1.5 Chemoresistance in the relapsing leukemias is not associated with the appearance of de novo DNA mutations

Several independent groups have analyzed the genomes of paired pre-therapy and relapsed AMLs, showing that acquired resistance emerges without new non-synonymous coding mutations in up to 40% of patients within some cohorts [139] [140] [141]. Our group recently

analyzed 30 AML patient pairs (at diagnosis and at relapse after chemotherapy) and observed no selection of genetic clones in 30% of cases, and selection of non-dominant clones in the remaining 70% (not published). Most notably, all cases showed persistence of multiple genetic clones, and in no case did we observe the emergence of a single genetic clone, suggesting that chemoresistance is not associated with the emergence of specific DNA mutations.

To investigate whether chemoresistance is associated with the emergence of specific DNA mutations in the two models of relapsing AML, I performed Whole Exome Sequencing (WES) of BM samples collected prior to chemotherapy, immediately after chemotherapy (at day 5 from the chemotherapy start; Persistent Blasts) and at relapse. DNA mutations were called according to established bioinformatic pipelines (see Methods) by comparing tumor samples with the corresponding germline DNA, obtained from the remission PBL of the AML patient who donated the BM for PDX establishment. Results of this analyses, including missense and non-sense mutations, frame-shift insertion or deletions, frameshift deletions and splice-site mutations are reported for each PDX in the Table of Fig. 16 and 17, respectively.

The non-treated AMLIEO20 leukemia presented 32 DNA mutations of various types, with a variant allele frequency (VAF) ranging from 55% to 13%. Notably, 28 of these mutations were also detectable in chemo-persistent blast and relapsed leukemia, though at slightly different VAFs. Two mutations with relatively low VAF (H2BC11 and POU6F2; 33% and 13%, respectively) were present in the untreated sample and in the Persistent Blasts, but absent in the relapsed leukemia.

The three datasets were subjected to PyClone analysis, a Bayesian clustering method used to reconstruct putative clonal clusters from their cellular prevalences (see Methods). Results showed the presence of two major clones in the untreated leukemia, one of which was characterized by the presence of the KRAS-G12V putative driver mutation. Importantly, we did not observe the disappearance of clones or the emergence of new clones in Persistent Blast or relapsed leukemia (Figure 16, lower panel). Together, these data suggest that the mutational landscape of AMLIEO20 leukemia is maintained in chemoresistant relapse.

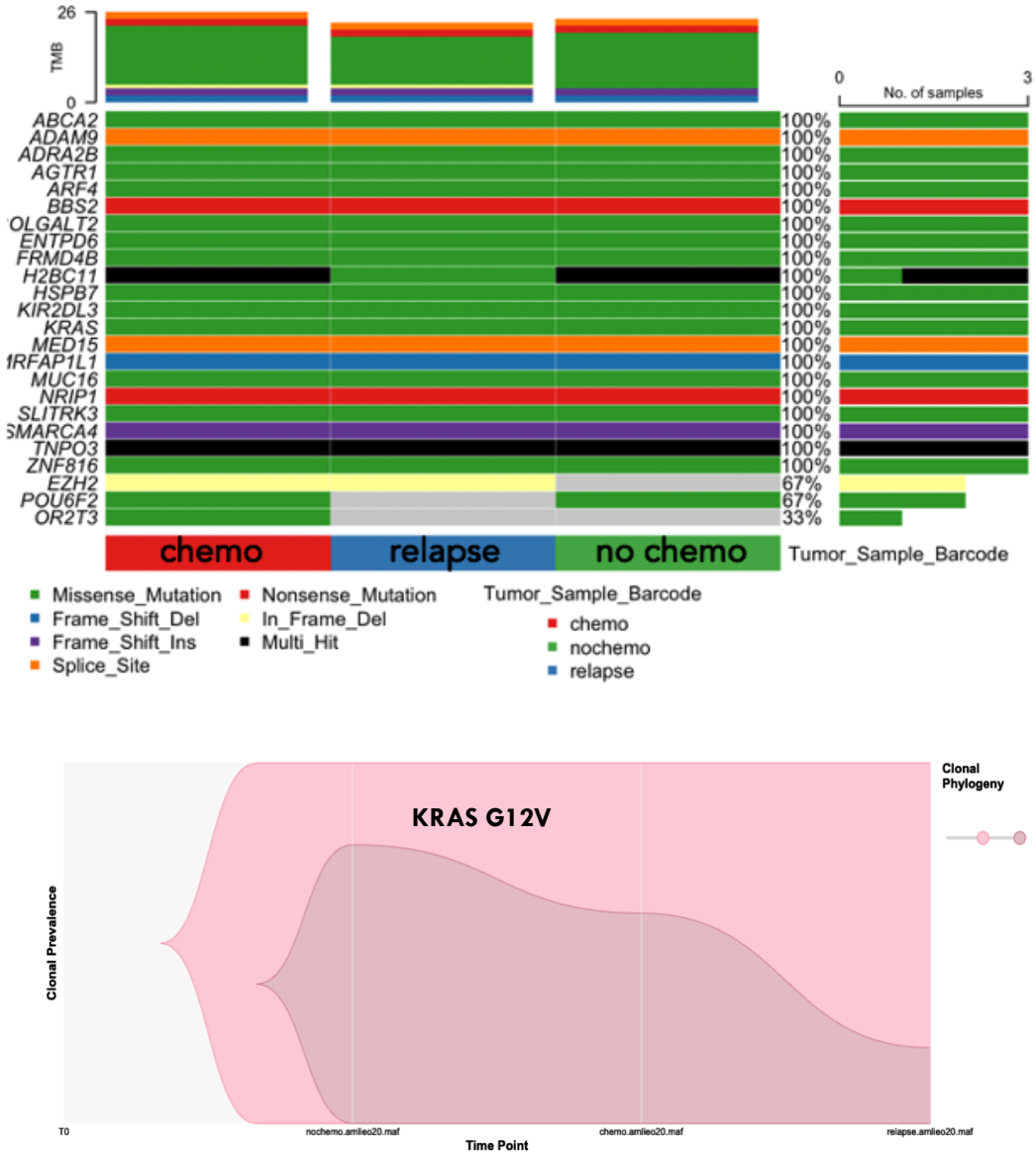

Figure 16 AMLIEO20 WES analysis, no selection of genetic clones

Top, onco-plot of the top 25 mutations found in no chemo (green box), chemo-persistent (red box) and relapse (blue box) BM samples; Tumor mutation burden (TMB) is reported for all conditions and color-coded sub-type of mutation are described in the legend; number of samples indicates the percentage of conditions in which a specific mutation is found. Bottom, Fish-plot of no chemo, chemo-treated and relapse BM samples clonal analysis. Non treated samples (n=2), chemo-treated samples (n=3), relapse samples (n=2).

Similar results were obtained from the analysis of the AML9 mutational datasets. Untreated AML9 leukemia presented 22 mutations, with VAF ranging from 59 to 6%, 14 of which were also present in Persistent Blasts and Relapsed Leukemia, albeit at different VAFs. Most notably, Persistent Blast and Relapsed Leukemias also presented unique mutations (2 and 5 respectively), usually at very low VAF. Many of the mutated genes showed multiple additional mutational spots at either the Persistent Blasts or the Relapsed

Leukemia (Figure 17). Clonal reconstruction analyses showed the presence of 7 putative sub-clones, with highly-variable relative representation. Strikingly, the same 8 clones were predicted in both Persistent Blasts and Relapsed Leukemias, although with different prevalences, while we did not document the disappearance of clones or the acquisition of new ones. Taken together, the results of the analysis of leukemias in both models did not show the emergence or loss of mutations that correlate with the acquisition of chemoresistance, suggesting that both models are representative of non-genetic mechanisms of chemoresistance.

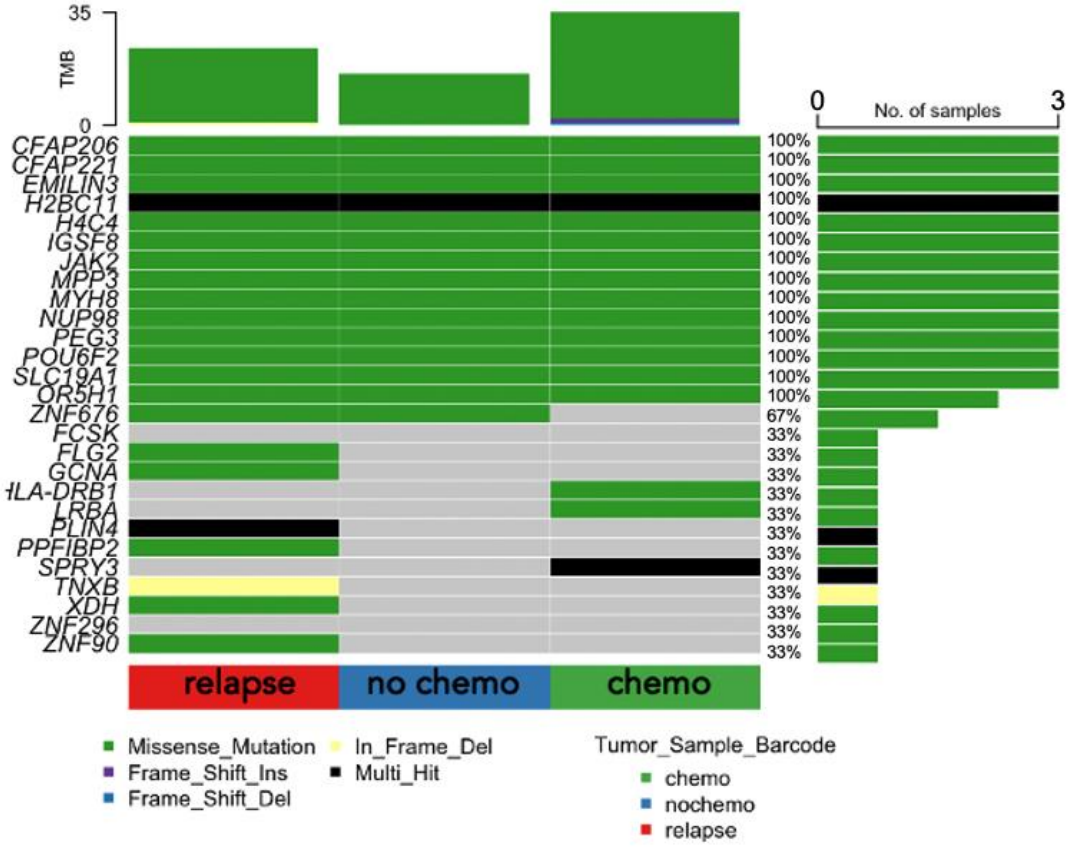

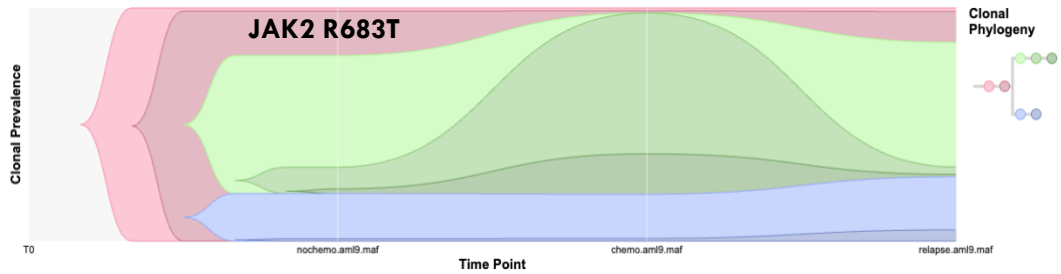

Figure 17 AML9 WES analysis, no selection of genetic clones

Top, onco-plot of the top 25 mutations found in no chemo (blue box), chemo-persistent (green box) and relapse (red box) BM samples; Tumor mutation burden (TMB) is reported for all conditions and color-coded sub-type of mutation are described in the legend; number of samples indicates the percentage of conditions in which a specific mutation is found. Bottom, Fish-plot of no chemo, chemo-treated and relapse BM samples clonal analysis. Non treated samples (n=2), chemo-treated samples (n=4), relapse samples (n=2).

In conclusion, the AML9 and AMLIEO20 models accurately replicate the development of clinical resistance to standard chemotherapy in AML. Specifically, AML9 behaves like a classic relapsed chemoresistant AML (secondary resistance), while AMLIEO20 more closely resembles a refractory AML (primary resistance). Notably, mutational profile analysis suggests that genetic mechanisms are unlikely to be the primary drivers of resistance in these two AML models, as is commonly observed in most, if not all, relapsed AML cases in clinical settings.

3.2 Analyses of chemo-persistent blasts

Emerging evidence suggests that the acquisition of drug resistance in cancer cells is linked to the persistence, after treatment, of rare cells with the ability to mitigate the cytotoxic effects of drugs, so called drug-tolerant persisters (DTPs) cells. One of the main characteristics of these cells is their quiescent state, and indeed, they share many traits in common with other quiescent cell types, such as cancer stem cells, disseminated dormant cells, and senescent cells. Often, the terms persistence, stemness, dormancy, and senescence are used synonymously, and the distinction between these cell types or states remains elusive. Distinctive features of DTPs, however, are that their tolerant phenotype is not supported by genetic alterations, their capacity for genetic evolution, and their significant phenotypic plasticity, which allows them to reversibly enter and exit the DTP state. These characteristics are thought to be crucial for their ability to drive tumor relapse and, eventually, establish a chemoresistant phenotype. Therefore, to investigate cellular and molecular mechanisms underlying the emergence of the chemoresistant phenotype in the two PDX models, I focused on those cells that survive chemotherapy, studying persistent blasts right after the end of the drug treatment, specifically at day 5 (24 hours after the end of chemotherapy).

Available experimental models, however, showed that chemotherapy persistent cells are not chemoresistant and maintain the same chemosensitivity after subsequent cycles of chemotherapy.

3.2.1 *In vitro* chemoresistance of AML Persistent Blasts

I first investigated whether persistent leukemic blasts from our two AML PDX models are chemotherapy resistant, by measuring drug sensitivity at cell level. To this end, I collected SPL blasts from non-treated leukemias and immediately after treatment, at day 5 from the start of the first round of chemotherapy (Persistent Blasts), and measured *in vitro* drug-sensitivity by evaluating the concentration of compound(s) where percent inhibition is equal to 50 (IC50 analysis). Leukemic blasts were treated with AraC and Doxorubicin as single agents. Starting at time-point 0 (before addition of AraC or Doxorubicin), cell viability was analyzed every 24, 48 and 72 hours, by measuring ATP-consumption with a luminescence assay and the Glomax® Plate Reader. Strikingly, AML9 persistent blasts showed complete resistance to AraC treatment at all doses tested (from 10mM to 0.001nM mM), as compared to control blasts, which instead showed an IC50 of 102.8 nM at 72 hrs from treatment start (Fig. 18). The same cell samples were treated with doxorubicin. In this case, AML9 Persistent Blasts showed a significantly higher IC50 (approximately 6-7 fold) compared to control blasts (Figure 18). The drug-sensitivity profiles of AMLIEO20 leukemia samples showed 2-3-fold higher IC50 values of Persistent Blasts for both AraC and doxorubicin, as compared to control blasts (Fig. 19).

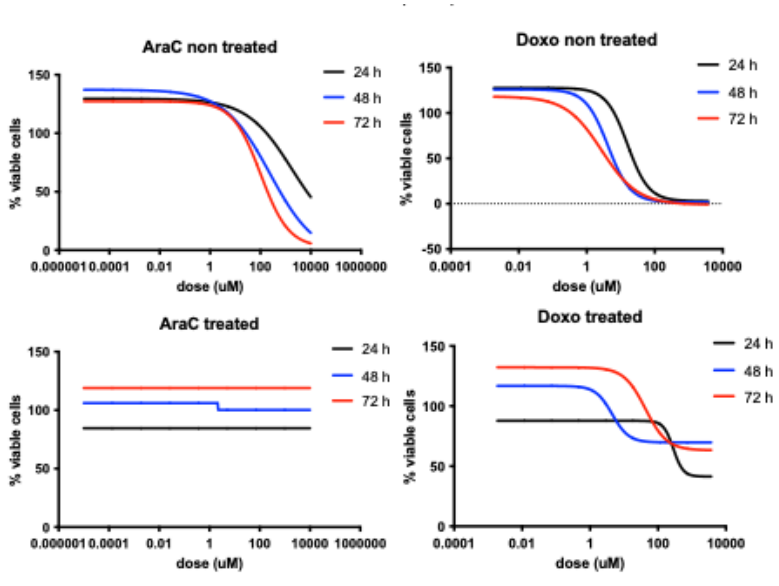

	AraC NT (nM)	AraC T (nM)
24 h	833,9	…
48 h	281,1	…
72 h	102,8	…

	Doxo NT (nM)	Doxo T (nM)
24 h	42,76	283,6
48 h	4,22	23,13
72 h	2,77	42,82

Figure 18 AML9 Chemo-persistent blasts are chemoresistant in vitro

IC50 assays in presence of doxorubicin (Doxo) or cytarabine (AraC) in previously chemotherapy treated versus non-treated control blasts; cell viability is shown with increasing concentrations of AraC and Doxo; values are shown as mean of triplicates for each concentration at 24h, 48h and 72h after the drug was added. Top IC50 graphs, AraC and Doxo treated blasts on non-treated BM samples; bottom IC50 graphs AraC and Doxo treated blasts of treated BM samples.

In conclusion, *in vitro* cultured Persistent Blasts from both PDX models showed IC50 values from 2-3 to 6-7 folds higher than those measured in non-treated blasts, suggesting that chemotherapy induces or selects a stable chemoresistance phenotype.

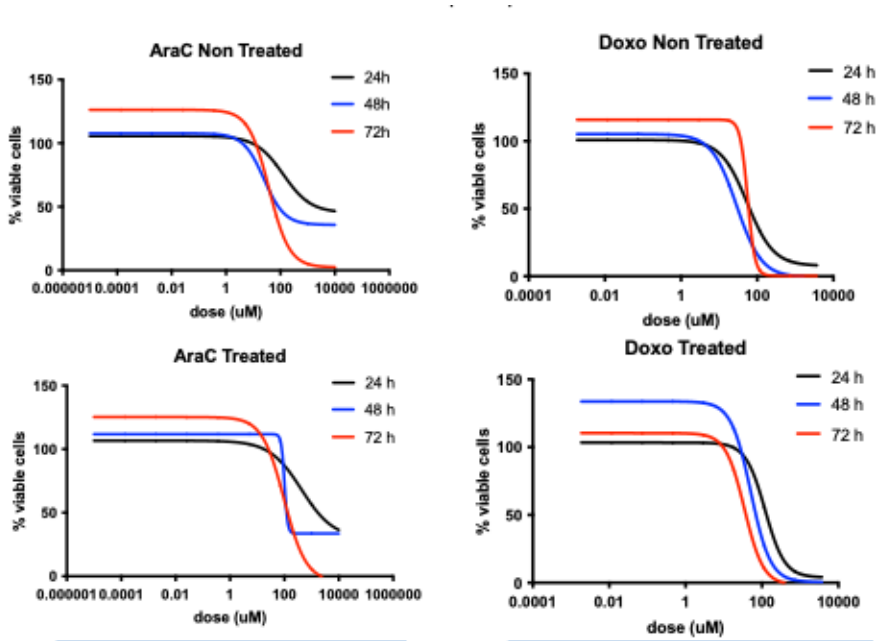

	AraC NT (nM)	AraC T (nM)
24 h	127,60	427,4
48 h	24,89	101,1
72 h	37,96	97,88

	Doxo NT (nM)	Doxo T (nM)
24 h	54,74	121,00
48 h	28,87	50,95
72 h	55,88	34,96

Figure 19 AMLIEO20 Chemo-persistent blasts are chemoresistant in vitro

IC50 assays in presence of doxorubicin (Doxo) or cytarabine (AraC) in previously chemotherapy treated versus non-treated control blasts; cell viability is shown with increasing concentrations of AraC and Doxo; values are shown as mean of triplicates for each concentration at 24h, 48h and 72h after the drug was added. Top IC50 graphs, AraC and Doxo treated blasts on non-treated BM samples; bottom IC50 graphs AraC and Doxo treated blasts of treated BM samples.

3.2.2 Cell cycle dynamics of AML Persistent Blasts

To test if chemotherapy selects cell cycle-restricted AML cells, I performed LR analyses, taking advantage of the previously described Tet-Off H2B-GFP models. NSG mice were transplanted with AML9 or AMLIEO20 blasts and, upon engraftment (15-20% blasts in the PB for AMLIEO20; 2-5% for AML9) doxycycline chasing started. After 5 days of chasing, mice were treated with the "5+3" chemotherapy regimen and data were collected pre-chemo (day0) and immediately post-chemo (day5). Analyses of GFP expression (GFP^{high}, GFP^{low} and GFP^{neg}) was performed on PB, BM and SPL samples, upon gating on the human cell population, using anti human CD45 antibody. The proportion of GFP^{high} cells was significantly increased in chemoresistant blasts in all analyzed samples (BM, Spleen and PB) and in both leukemias (from 2-6% to 20-40% in the AML9 samples; from 2-10% to 25-30% in the AMLIEO20). However, all samples contained large proportions of GFP^{low} and GFP^{neg} subpopulations, at frequencies varying from sample to sample, suggesting that a fraction of persistent blasts had proliferated during treatment (Figure 20).

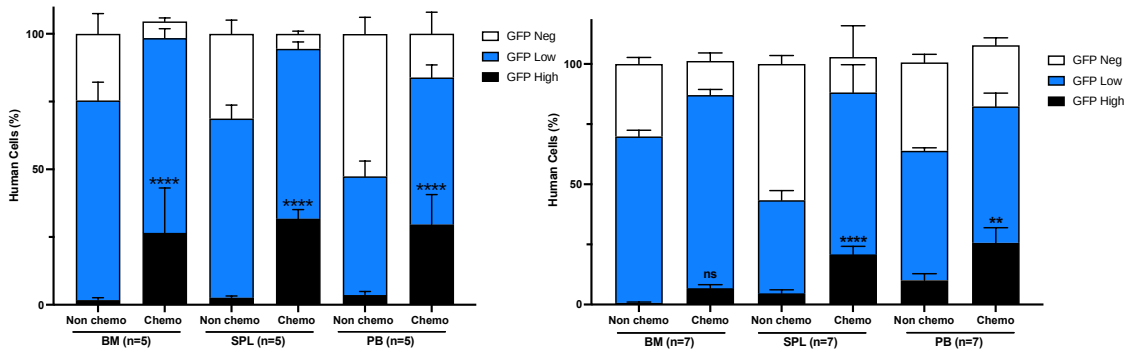

Figure 20 Quiescent H2B-GFP^{high} blasts are enriched after chemotherapy

*GFP levels in BM, SPL and PB human cells is plotted for chemo and non-chemotherapy treated mice at day 5. Left AML9, right AMLIEO20. Mice were transplanted with AML9 or AMLIEO20 blasts and treated with chemotherapy (at a PB engraftment of 2-5% and 20-30% for AML9 and AMLIEO20 respectively). PB, BM and SPL blasts were isolated form non-treated and chemotherapy treated mice. Human Blasts were gated based on CD45 antibody positivity and GFP level were further analyzed dividing human cells according to their GFP signal in GFP^{high}, GFP^{low} and GFP^{neg} (ns, not significant, ** P < 0.01, *** P < 0.001, and **** P < 0.0001 by 2way ANOVA test).*

To investigate cell-cycle kinetics during chemotherapy, I designed another experiment in which doxycycline chasing started at the same time as chemotherapy. NSG mice were transplanted with AMLIEO20. Upon 20-30% engraftment in the PB, doxycycline chasing started simultaneously with chemotherapy administration (*"5+3"* regimen).

PB samples were collected prior to chemotherapy and at the last day of chemotherapy (day 5), stained them with anti-human CD45 and analyzed by flow cytometry. In the non-treated sample, the GFP signal was diluted generating GFP^{low} and GFP^{neg} populations. Instead, in the chemotherapy-treated group I observed a lower extent of GFP signal dilution,

which generated a high-intensity GFP^{low} population (Fig. 21). Non-treated sample showed the expected dilution of GFP signal with establishment of all three leukemic subpopulations (GFP^{high}, GFP^{low}, GFP^{neg}). Instead, in the chemotherapy-treated sample, I observed a modified GFP signal-dilution, with establishment of GFP^{high} and GFP^{low} population, but not GFP^{neg} cells. Proliferation analyses showed that on average approximately 27% of treated cells divided, while approximately 75% of control sample cells went into division in the 5 days of doxycycline chasing (data not shown).

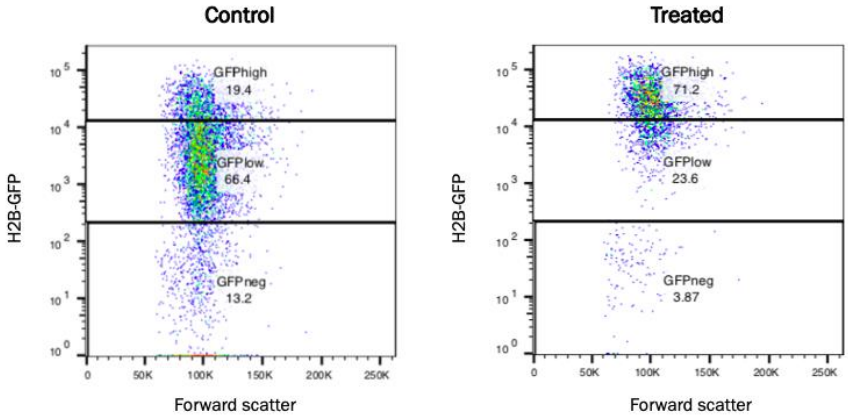

Figure 21 Representative plots of proliferation analysis of PB at day 5 of chemotherapy treated (right) and non-treated mouse (left).

Overall, these results demonstrate that Persistent Blasts are composed of both proliferating and quiescent cells. Quiescent blasts are enriched after chemotherapy, yet quiescence does not appear a specific trait of chemotherapy-persistent blasts. Analyses of cell-proliferation kinetics, indeed, suggest that fast-proliferating cells are eliminated by chemotherapy, but a portion of leukemia cells continue to proliferate during treatment.

3.2.3 Chemo-persistent blasts possess regenerative potential

I then decided to investigate how chemotherapy influences the tumorigenic potential of quiescent versus proliferating chemotherapy-persistent cells. To this end, I measured the frequency of leukemia-initiating cells (LICs) in AMLIEO20 persistent-cells by the limiting dilution transplantation assay. I isolated GFP^{high} and GFP^{verylow} cells from AMLIEO20 PDX model at the end of chemotherapy treatment (day 5). This time-point, in my protocol, corresponds to 11 days of chasing (see Fig. 5). GFP^{high} and GFP^{verylow} cells were transplanted into NSG mice under limiting dilution conditions (from 5,000 to 100 cells) (Figure 22). The calculated LIC frequency was the same in both GFP^{high} and GFP^{verylow} populations (1:3529) (Figure 22, right panel). Notably, the two samples showed similar engraftment progression,

thus confirming the equal tumorigenic potential of GFP^{high} and GFP^{verylow} cells (see Figure 22, left panel, for representative single-mouse engraftment data after injection of 5,000 cells). Altogether these data demonstrate that quiescent Persistent Blasts possess regenerative potential which is equally distributed between quiescent and proliferative blasts. LICs are able to equally and quickly re-enter proliferation.

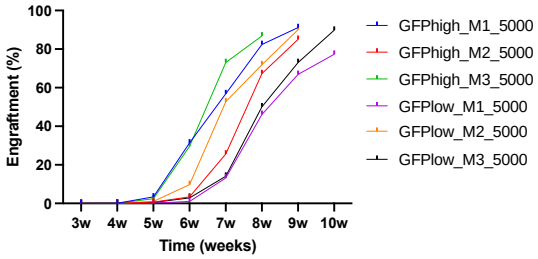

Dose	GFPhigh	GFP very low
5000	3/3	3/3
1000	0/3	0/3
500	0/3	0/3
100	0/3	0/3
LSC	**1:3529**	**1:3529**

Figure 22 GFP^{high} and GFP^{low} chemotherapy persistent blasts show equal regenerative potential

PB engraftment levels in shown as single mice of the highest dose injected in the limiting dilution scheme experiment, left. Limiting dilution scheme and LICs frequency as calculated by ELDA (http://bioinf.wehi.edu.au/software/elda/) in AMLIEO20 chemotherapy persistent blasts, right. In this experiment doxycycline chasing period is 11 days.

However, these data do not allow us to conclude that only quiescent cells possess regenerative capacity. Indeed, a previous PhD student in my laboratory (Sara Milovanovic) demonstrated that proliferating blasts have the ability to exit the cell cycle after multiple rounds of division and re-enter quiescence. In particular, Sara analyzed the cell-cycle properties of AMLIEO20 GFP^{high} vs GFP^{low} cells, using combined KI67-BrdU-DAPI analyses, and demonstrated that after 10 or 14 days of chasing, while >95% of GFP^{high} cells are in G0, the percentage of cells in G1-S-G2M of GFP^{low} cells is only 25-30%, with the remaining cells in G0. Thus, after 10-14 days of chasing, the GFP^{low} population is composed of proliferating cells and cells that have re-entered quiescence. Sara further demonstrated that at shorter chasing times (5 days), the percentage of quiescent blasts (G0) in the GFP^{low} population is negligible, likely due to the fact that the proliferating blasts have not yet re-entered a state of quiescence. Modelling of GFP dilution data showed that at day 5 of doxycycline chasing, GFP^{high} consist of blasts that haven't divided yet (quiescent cells), while GFP^{verylow} contain cells that divided 7-8 times. A schematic representation of the GFP dilution patterns after 10 or 5 days of chasing is shown in Figure 5.

Based on these data, to assess the regenerative capacity of quiescent/slow proliferating versus fast proliferating blasts, I measured the LIC frequency of GFP^{high} vs. GFP^{verylow} populations purified by FACS-sorting from both AML PDX models after 5 days

of chasing. I transplanted GFP^{high} and GFP^{verylow} cells into NSG mice in limiting dilution (from 10000/5000 to 100 cells) and monitored mice for up to 6 months. The calculated frequency of LICs in AML9 was 1:734 vs. 1:5366 in the GFP^{high} vs. GFP^{verylow} populations, respectively. For the AMLIEO20, LIC frequencies in the same two populations were 1:1161 and 1:12793, respectively (Figure 23). Thus, at steady-state, the LIC frequency of the GFP^{high} subpopulation is markedly higher than the GFP^{verylow} counterpart, suggesting the quiescent LICs are the only cell-type endowed with regenerative potential. I am currently replicating these experiments with persistent blasts obtained after chemotherapy and 5 days of chasing. In conclusion, though quiescence is not as specific trait of chemoresistance, yet it appears integral to the relapsing properties of chemo-persistent blasts.

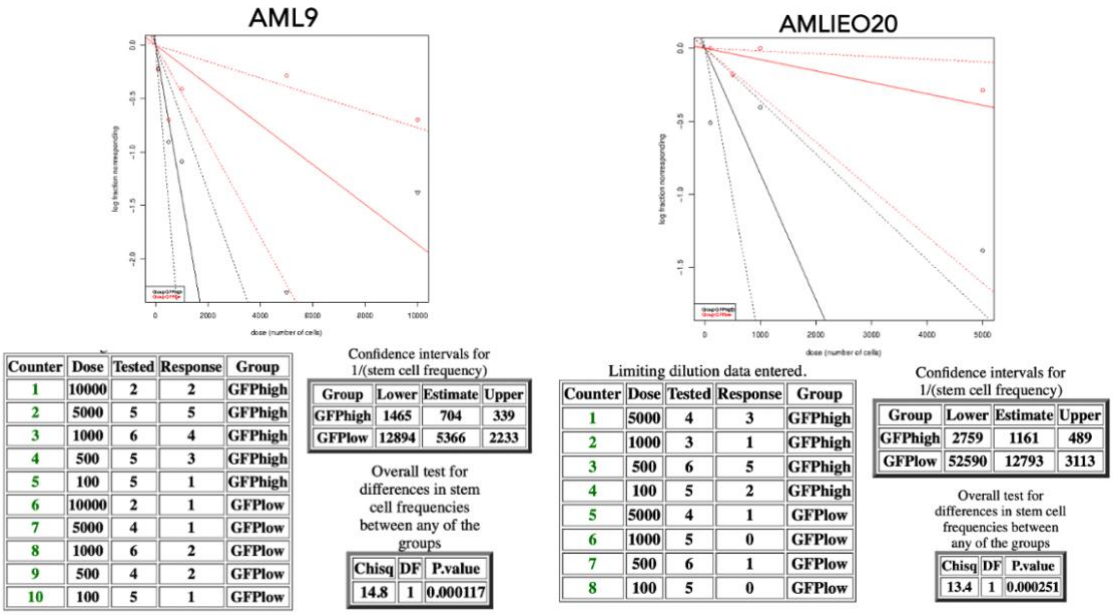

Counter	Dose	Tested	Response	Group
1	10000	2	2	GFPhigh
2	5000	5	5	GFPhigh
3	1000	6	4	GFPhigh
4	500	5	3	GFPhigh
5	100	5	1	GFPhigh
6	10000	2	1	GFPlow
7	5000	4	1	GFPlow
8	1000	6	2	GFPlow
9	500	4	2	GFPlow
10	100	5	1	GFPlow

Confidence intervals for 1/(stem cell frequency)

Group	Lower	Estimate	Upper
GFPhigh	1465	704	339
GFPlow	12894	5366	2233

Overall test for differences in stem cell frequencies between any of the groups

Chisq	DF	P.value
14.8	1	0.000117

Limiting dilution data entered.

Counter	Dose	Tested	Response	Group
1	5000	4	3	GFPhigh
2	1000	3	1	GFPhigh
3	500	6	5	GFPhigh
4	100	5	2	GFPhigh
5	5000	4	1	GFPlow
6	1000	5	0	GFPlow
7	500	6	1	GFPlow
8	100	5	0	GFPlow

Confidence intervals for 1/(stem cell frequency)

Group	Lower	Estimate	Upper
GFPhigh	2759	1161	489
GFPlow	52590	12793	3113

Overall test for differences in stem cell frequencies between any of the groups

Chisq	DF	P.value
13.4	1	0.000251

Figure 23 GFP^{high} blasts are carriers of tumorigenic potential

Limiting dilution scheme and LICs frequency as calculated by ELDA (du.au/software/elda/), left AML9, right AMLIEO20. LICs frequency is calculated at day 5 of doxycycline chasing. Mice were transplanted with serial dilutions (ranging from 10000/5000 to 100) of sorted GFP^{high} and GFP^{low} blasts and followed up to 6 months in their PB engraftment.

3.2.4 Chemotherapy does not select specific lineages

To analyze clonal evolution during chemotherapy, I set up a lineage tracing experiment using a high-complexity lentiviral library of expressed barcodes. I used the 3rd generation lentiviral Perturb-seq Guide Barcodes (GBC) library, which contains unique barcode sequences (18 nucleotides) used for recognition of a mother cell and its progeny, as well as PuroR selection marker and BFP fluorescence reporter.

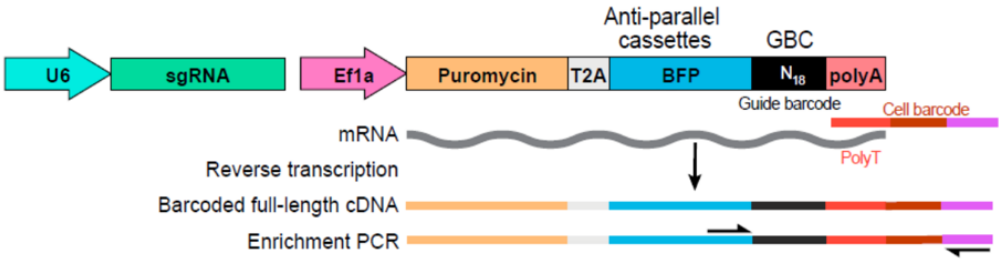

Figure 24 Perturb-seq Guide Barcodes (GBC) library vector structure

3rd generation lentiviral vector contains a random 18-nt GBC between the blue fluorescent protein (BFP) and polyadenylation signal sequences. The vector contains genes that encode for puromycin and ampicillin resistance and the reporter gene TagBFP. Puromycin resistance and TagBFP are constitutively expressed under the control of the EF1α promoter.

The complexity of the library is estimated at 10 x 10^6 unique barcodes. I infected AMLIEO20 cells at a low Multiplicity of Infection (MOI) to obtain a single barcode integrated per cell. After 3 days from infection, I FACS-sorted the BFP+ blasts, which were then injected into NSG mice: mice were monitored weekly for engraftment in the PB, by analyses of the percentage human cells (anti-humanCD45 antibodies) and, within this population, BFP+ barcoded cells (see Figure 24 and Figure 25 for a schematic representation of the experimental approach).

Mice were treated with the *"5+3"* chemotherapy regimen when engraftment was around 20%. Percentages of barcoded BFP+ cells varied significantly across individual mice (1-33%; not shown). I performed two independent experiments of lineage tracing using AMLIEO20 cells, shown in Figures 23 and 24, respectively. In the first experiment (Figure 26), I analyzed, at Day 0, the clonal structure of blasts obtained from the BM of one mouse and blasts obtained from the PB and BM of a second mouse. A third mouse was longitudinally analyzed in the PB blasts at Day 0 and Day 5. The same mouse was then sacrificed at Day 5 and the BM collected to perform the same clonal structure analysis. In a second experiment (Figure 26), I longitudinally analyzed the leukemia in the same mouse, and collected samples according to the same scheme: PB at Day 0 and Day 5, BM at Day 5. In both experiments, I collected and analyzed clonal structure of the leukemias transduced with the barcode library, before mouse injection (3 samples for each of the two experiments).

Human barcoded cells were purified by FACS-sorting of CD45- and BFP-positive cells obtained from PB and BM cell-suspensions. Genomic DNA was extracted from freshly sorted blasts and subjected to NGS sequencing as described in Materials and Method section.

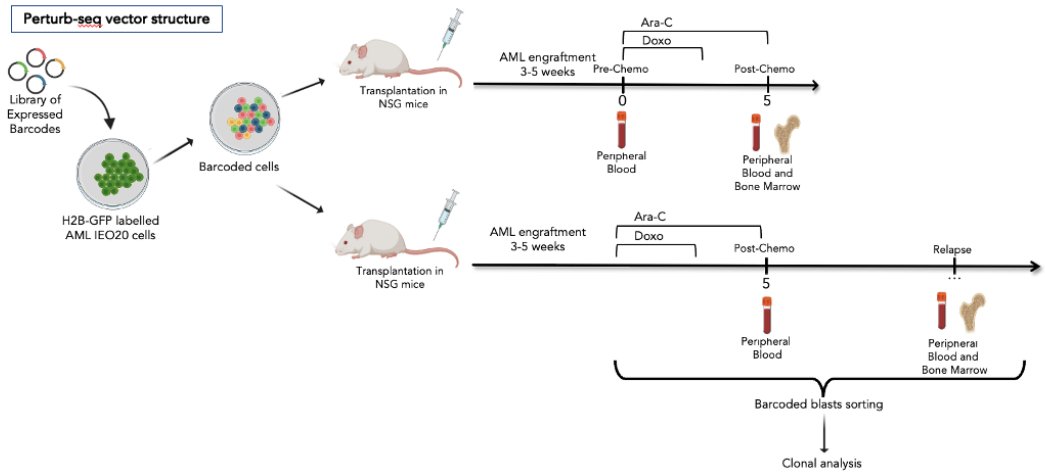

Figure 25 Longitudinal lineage tracing experimental scheme

Experimental scheme for the lineage tracing experiment. NSG mice were transplanted with AMLIEO20 blasts infected with the GBC library at MOI=1. Upon PB engraftment, mice were randomized and treated or not with "5+3" chemotherapy treatment regimen. Peripheral blood samples were isolated pre- and post-chemotherapy and bone marrow samples isolated post-chemotherapy, from longitudinal mice. Mice were sacrificed and PB and BM processed. Blasts were FACS-sorted according to BFP positivity. Sorted blasts were sequenced by scRNAseq. Only the first branch, which described the clonal evolution of AML pre chemotherapy and after chemotherapy treatment (day 0 and day 5 respectively) of the experimental scheme has been performed and described in this thesis.

Clonal complexity was quantified using the expansion index, a direct measure of clonality of a given sample that ranges from 0 to 1, where 1 correspond to a purely monoclonal sample and 0 to a sample with uniform clonal frequency (shown in the Tables of Figures 26 and 27). For each sample, we also report a stack bar of the identified clones (we selected clones with a threshold of 1000 reads per barcode). The Expansion Index of the reference samples was close to 0 for both experiments, suggesting that they were composed of a high number of clones with uniform frequency.

In the first experiment, the expansion Index of the untreated BM samples was instead very high, ranging from 0,7 to 0,8 in the two analyzed mice (Figure 26). In both cases, one clone dominated over the others, reaching a relative frequency of >70%. Clonal composition of the matched PB (PB3_1 and BM3_1 from the same mouse) was similar almost identical (Figure 26), suggesting that PB (which is the only sample accessible for longitudinal studies) can be used instead of BM to assess clonal dynamic and composition of AMLs.

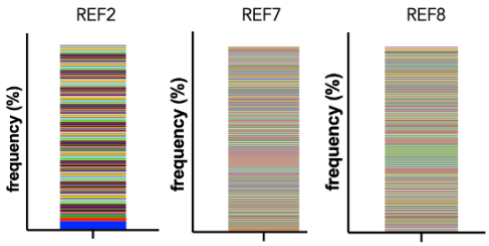

Sample	Total barcodes	Barcode ratio	Shennon entropy	Expansion index
REF2	31618	0,993	4,443	0,013
REF7	10212	0,993	3,970	0,009
REF8	17908	0,993	3,861	0,009

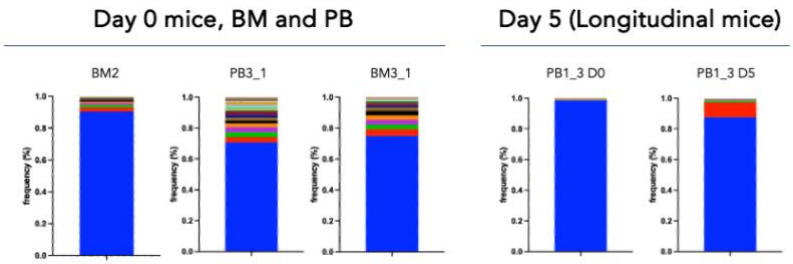

Sample	Total barcodes	Barcode ratio	Shennon entropy	Expansion index
BM 2	27	0,993	0,235	0,836
BM 3_1	117	0,993	0,543	0,737
PB 3_1	71	0,993	0,662	0,642
PB 1_3 D0	15	0,993	0,039	0,966
PB 1_3 D5	15	0,993	0,211	0,821

Figure 26 Clonal dynamics of AML during chemotherapy treatment

Clonal composition and frequencies of clones are shown for the reference samples (REF2, REF7, REF8) and clones are color-coded; total barcodes, barcode ratio, Shannon entropy and Expansion index are shown in the table. Clonal composition and frequencies of clones are shown per sample at day 0 (BM2, PB3_1, BM3_1) (bottom left); clonal composition and frequencies of clones are shown for the longitudinal mouse (PB1_3 Day0, PB1_3Day5) and clones are color-coded; total barcodes, barcode ratio, Shannon entropy and Expansion index are shown in the table.

Longitudinal analysis of clonal composition before and after chemotherapy (PB 1-3 Day=0 vs PB 1-3 Day=5; Figure 26) did not reveal significant differences between the two samples. Notably, the Persistent Blasts exhibited a massive expansion of one clone, molecularly identical to that of the sample prior to chemotherapy. In the Persistent Blasts, I observed the expansion of several minor clones, with the largest expanding from 0.1% on day 0 to 5% on day 5. In conclusion, a single dominant clone is present in the leukemic cells prior to chemotherapy, which maintains the same clonal fitness after chemotherapy, suggesting that chemotherapy does act on leukemia cells by selecting specific lineages.

Same results were obtained in a second experiment using the same AML (AMLIEO20). I observed the same monoclonal composition of PB at day 0, with a single clone that maintained its fitness advantage over the others after chemotherapy. Moreover, I observed a low expansion of a minor clone post-chemotherapy, which passed from 0,1 (day 0) to 5 % (day 5). The clonal structure of blasts from the BM after chemotherapy treatment was even more dramatic/drastic, showing the presence of a single dominant clone (the same observed in PB), with a frequency over the 98% (Figure 27).

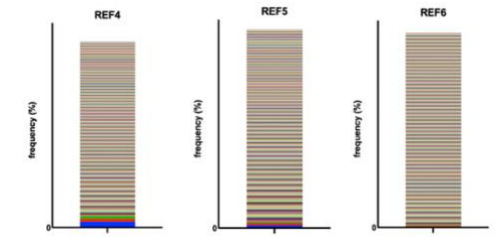

Sample	Total barcodes	Barcode ratio	Shennon entropy	Expansion index
REF4	23767	0,96	4,298044823	0,017808501
REF5	13284	0,98	4,029488	0,022758521
REF6	15412	0,99	3,688641138	0,011977596

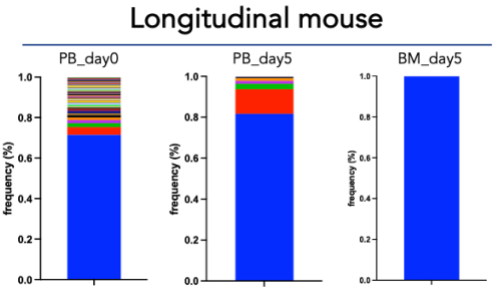

Sample	Total barcodes	Barcode ratio	Shennon entropy	Expansion index
PB day0	52	0,93	0,710720678	0,585827918
PB day5	19	0,81	0,301185191	0,764469722
BM day5	48	0,95	0,004953955	0,997053394

Figure 27 Clonal dynamics of AML during chemotherapy treatment

Clonal composition and frequencies of clones are shown for the reference samples (REF4, REF5, REF6) and clones are color-coded; total barcodes, barcode ratio, Shannon entropy and Expansion index are shown in the table (top). Clonal composition and frequencies of clones are shown per sample for the longitudinal mouse (PB_day0, PB_day5, BM_day5) and clones are color-coded; total barcodes, barcode ratio, Shannon entropy and Expansion index are shown in the table (bottom).

In conclusion, chemotherapy does not select specific cellular clones; the AML clonal structure is not modified by chemotherapy treatment, with the exception of a few clones with low fitness.

3.3 Activation of the Interferon-signalling pathways in chemotherapy-persistent blasts

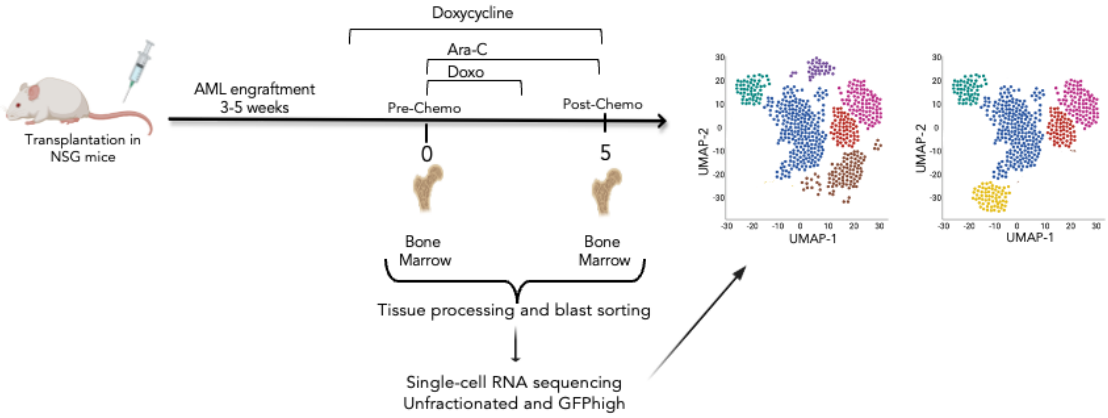

Figure 28 Transcriptional phenotypic properties of chemotherapy persistent blasts.

Experimental scheme for the characterization of persistent blasts. NSG mice were transplanted with AMLIEO20 or AML9 blasts. Upon PB engraftment, mice were randomized and treated or not with "5+3" chemotherapy treatment regimen. Chemo and non-chemotherapy treated mice were sacrificed and BM processed. Blasts were FACS-sorted according to human-CD45 marker positivity and the GFP^{high} subpopulation. Sorted blasts were sequenced by scRNAseq.

To investigate molecular mechanisms of chemoresistance, I performed scRNAseq (Figure 28) analyses of blasts isolated before chemotherapy (day 0) and immediately after (day 5; Persistent Blasts) from either AMLIEO20 or AML9 leukemias. NSG mice were transplanted with AMLIEO20 or AML9 blasts, doxycycline-chased (as described in the generation of the models), and treated or not with the *"5+3"* chemotherapy treatment regimen.

Chemo-treated (day 5; n=2) and control (day 0; n=2) mice were sacrificed, and BM collected and processed. From the BM, I prepared bulk/unfractionated and GFP^{high} samples. GFP^{high} blasts were prepared by FACS-sorting of GFP^{high} cells human-CD45 gating. The 16 samples were submitted for scRNAseq (2 unfractionated and 2 GFP^{high} samples, collected at day 0 or day 5). I will first describe analyses of unfractionated cell populations.

Unsupervised Louvain clustering analysis and UMAP dimensionality reduction identified 8 transcriptional cell clusters for AMLIEO20 and 10 for AML9 (Figure 29 and Figure 30). Analysis of the relative distribution of each cluster revealed marked differences between the two samples, characterized by the expansion or reduction of most clusters. In the AMLIEO20 UMAP (Figure 29), clusters 2, 3, 4, and 6 were strongly expanded (collectively, they increased from 5% in Day 0 samples to 20-25% in Day 5 samples), primarily at the expense of clusters 0 and 1 (from 30-35% to 3-5%). Similarly, in AML9

(Figure 30), clusters 3, 6, 8, and 9 significantly expanded in Day 5 samples (from 5% to 15-25%), at the expense of clusters 0, 1, 2, and 4 (from 20% to 5%).

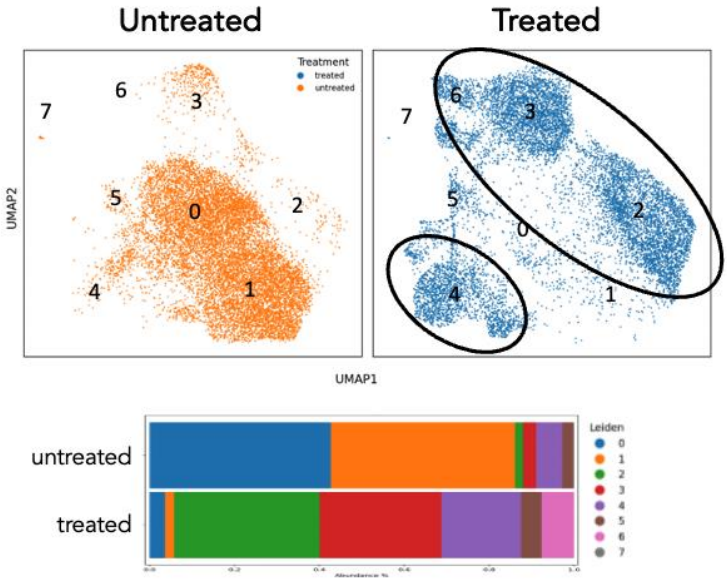

Figure 29 AMLIEO20 Chemotherapy persistent blasts showed expansion of specific clusters

UMAP visualization of BM samples treated (day 5) and untreated (day 0) with chemotherapy (top); cluster composition of analyzed samples (bottom), shown in % for treated and untreated BM samples.

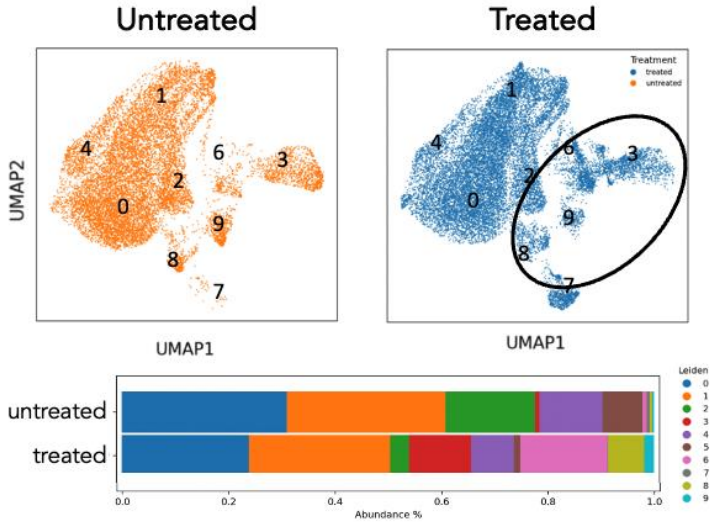

Figure 30 AML9 Chemotherapy persistent blasts showed expansion of specific clusters

UMAP visualization of BM samples treated (day 5) and untreated (day 0) with chemotherapy (top); cluster composition of analyzed samples (bottom), shown in % for untreated and treated BM samples.

Then, I focused on the phenotypic characterization of chemotherapy persistent blasts (day 5) by analyzing the clusters enriched/expanded post-chemotherapy of both the AML PDX models. Remarkably, I observer expansion of specific cluster post-chemotherapy which were common between bulk and GFP^{high} samples (3, 6, 8, 9 for AML9 and 2, 3, 4, 6 for AMLIEO20). Form published signatures form Van Galen et al., 2019, I performed cell imputation on my dataset and showed that expanded clusters post-chemotherapy were characterized by undifferentiated/immature phenotype (GMP-like, Promono-like, cDC-like, HSC-like/Progenitor-like) (Figure 31).

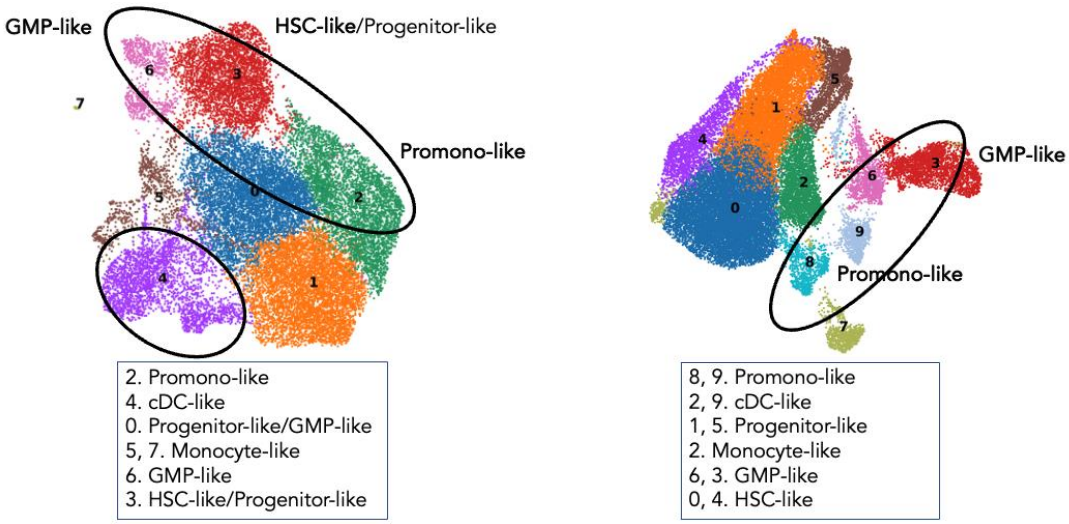

Figure 31 Expanded clusters are characterized by undifferentiated/immature phenotype

Cell imputation of signatures of hematopoietic states from Van Galen et al. 2019, are showed in the UMAP of AMLIEO20 right, and AML9, left.

3.3.1 Transcriptional characterization of chemotherapy-resistant quiescent blasts

To investigate whether the expanded clusters post-chemotherapy acquired unique transcriptional features, I characterized these clusters by analyzing their marker genes. Strikingly, for each expanded cluster, Gene Set Enrichment Analysis (GSEA) revealed a strong enrichment of genes involved in the Interferon signaling pathway (Type I Interferon signaling pathway, Interferon-gamma mediated signaling pathway, cellular response to type I interferon, etc.) (see Figure 32 and Figure 33 for AMLIEO20 and AML9 respectively). The acquisition of upregulated interferon signaling appears to be a predominant feature of cells that survive chemotherapy. Indeed, GSEA analysis of DEGs between Day 5 versus Day 0 samples (analyzed on the bulk cell populations) clearly revealed significant upregulation of IFN pathway genes (e.g., Interferon Alpha Response, Interferon Gamma Response, Type I Interferon Signaling Pathway, Cellular response to type I interferon, Interferon-gamma

mediated signaling pathway) (Figure 34 and Figure 35 bar plots). Analysis of the expression of the top 50 DEGs confirmed their marked upregulation in Persistent Blasts compared to blasts prior to chemotherapy (Figure 34 and 35, left plot). Thus, cells that survive chemotherapy are characterized by the acquisition of a specific transcriptional state characterized by the upregulation of genes involved in IFN signaling.

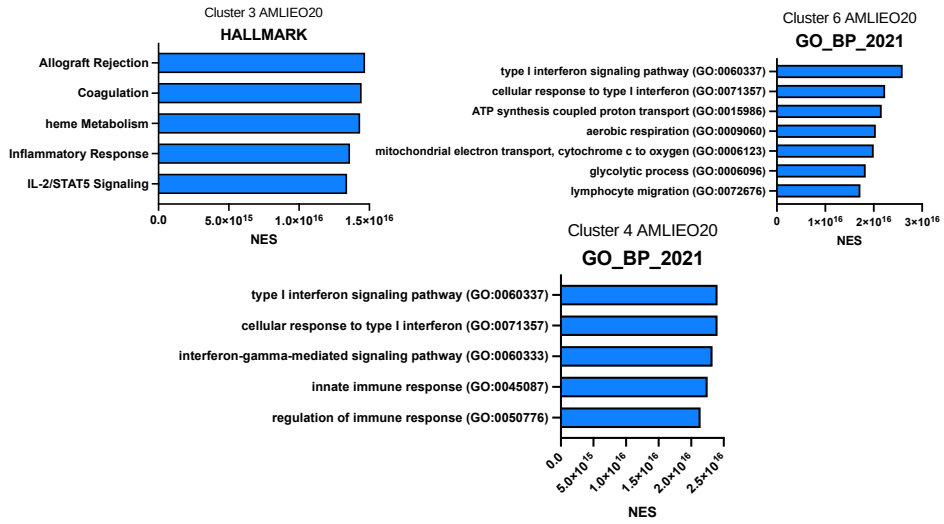

Figure 32 AMLIEO20 expanded clusters are enriched in interferon-signalling pathway

GO_BP_2021 and HALLMARK pathways enriched in day 5 post-chemotherapy expanded clusters of AMLIEO20.

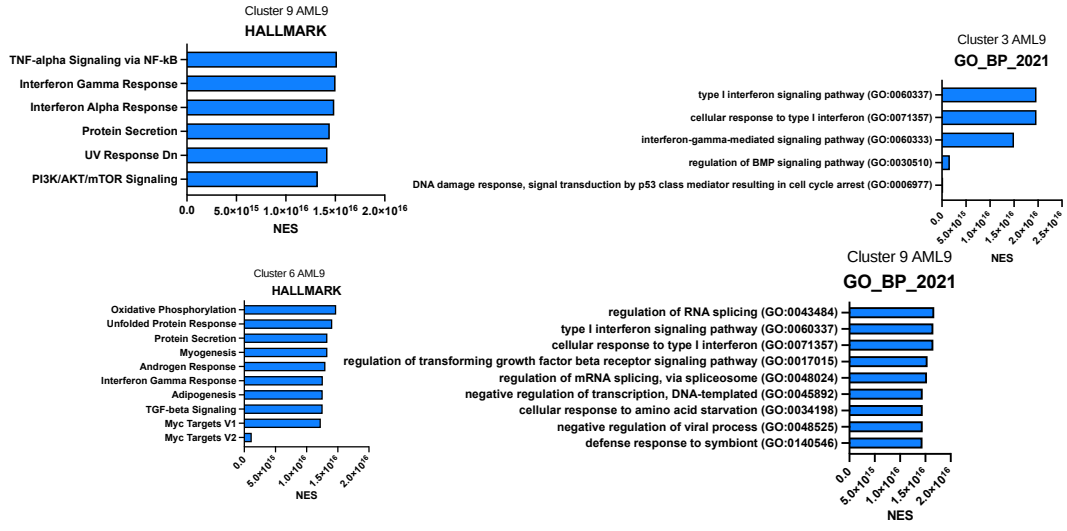

Figure 33 AML9 expanded clusters are enriched in interferon-signalling pathway

GO_BP_2021 and HALLMARK pathways enriched in day 5 post-chemotherapy expanded clusters of AML9.

3.3.2 Interferon-signalling pathways are activated also in the quiescent chemotherapy-Persistent Blasts

I then questioned whether also quiescent Persistent Blasts, which represent a small subset of all Persistent Blasts, exhibited upregulation of interferon signaling genes. To characterize the transcriptional properties of persistent quiescent blasts, I first identified Day 0 versus Day 5 DEGs in the GFP^{high} samples. As with the bulk samples, GSEA analysis clearly revealed significant upregulation of IFN pathways (e.g., Interferon Alpha Response, Interferon Gamma Response, Type I Interferon Signaling Pathway, Cellular response to type I interferon, Interferon-gamma mediated signaling pathway) in the day 5 GFP^{high} cells, as compared to Day 0 GFP^{high} cells (Figure 34 and Figure 35 bar plots). Analysis of the expression of the top 50 DEGs confirmed their upregulation in GFP^{high} Day 5 versus GFP^{high} Day 0 (Figure 34 and 35 right plots). Together, these results suggest that the acquisition of a chemoresistant phenotype correlates with the acquisition of a transcriptional state associated with upregulation of interferon signaling, regardless of the cell-cycle properties of the persistent blasts. Therefore, quiescence does not appear to be a specific state of chemoresistance.

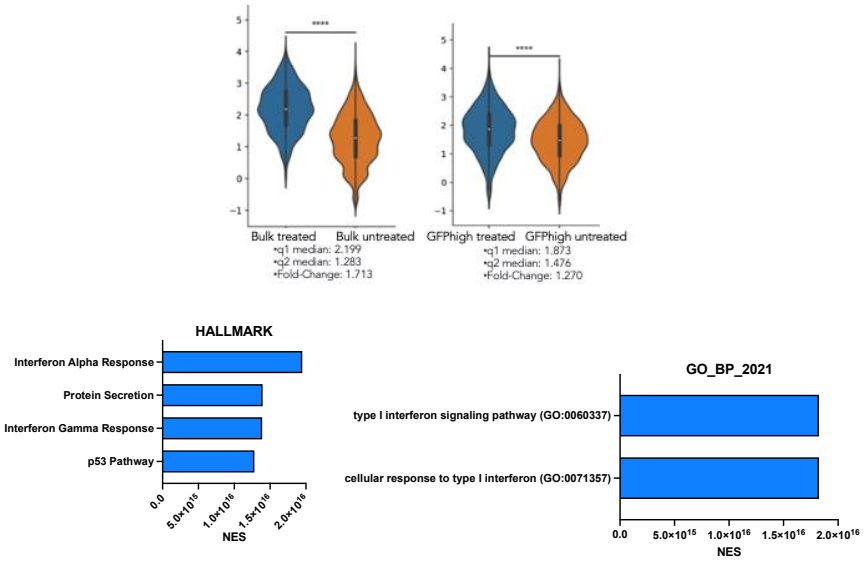

Figure 34 AML9 chemo-persistent blasts express IFN signalling pathway in response to chemotherapy treatment

Analysis of the expression of the first 50 top differentially expressed genes of treated versus untreated samples (bulk top left, and GFP^{high} top right). GSEA analysis of bulk and GFPhigh (HALLMARK bottom left and GO_BP_2021 bottom right).

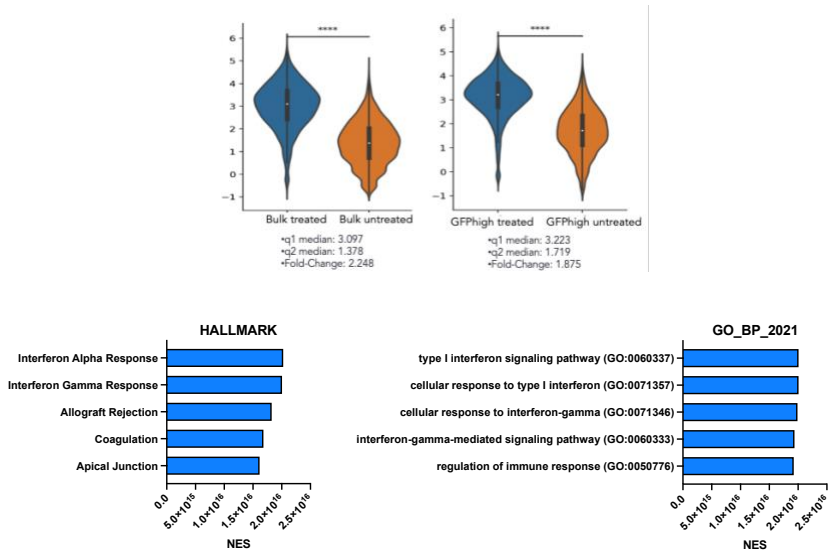

Figure 35 AMLIEO20 chemo-persistent blasts express IFN signalling pathway in response to chemotherapy treatment

Analysis of the expression of the first 50 top differentially expressed genes of treated versus untreated samples (bulk top left, and GFP^{high} top right). GSEA analysis of bulk and GFPhigh (HALLMARK bottom left and GO_BP_2021 bottom right).

3.3.3 Identification of an Interferon-related signature that characterize chemo-persistent blasts

I then focused on the IFN pathway-genes that were upregulated in Chemotherapy-Persistent Blasts. For each AML mouse model, I first created a non-redundant list of the top 50 DEGs obtained from the post- versus pre-chemotherapy comparison for each of the expanded clusters. These genes were then categorized into major biological pathways (e.g., IFN response, DNA damage, DNA repair, cell cycle, inflammation, apoptosis) based on literature studies and manual curation. Focusing on IFN-response genes, I selected those that were common between bulk and GFP^{high} populations for each model. The union of the two resulting lists generated an IFN gene signature of 17 genes (IFI6, LY6E, ISG15, TRIM22, TRIM38, NDUFA13, IRF7, IFI44L, VWCE, GBP1, GBP4, IFI44, MX1, IFIT1, USP18, PARP9, IFITM1), of which 6 were common between the AML9 and AMLIEO20 models (IFI6, ISG15, LY6E, TRIM22, NDUFA13, IFITM1). This gene signature, and the 6 genes in common between the two PDX models, contain genes whose function is well characterized in IFN signalling, such as: ISG15, a ubiquitin-like protein that is conjugated to intracellular target proteins upon activation by interferon-alpha and interferon-beta [142]; IFITM1, IFN-induced gene which controls and regulate antiviral response which plays a key role in the antiproliferative action of IFN-gamma either by inhibiting the ERK activation or

by arresting cell growth in G1 phase in a p53-dependent manner [143]; TRIM22, an IFN-inducible protein that is induced by IFN-alpha and IFN-gamma and has been demonstrated to restrict the replication of many viruses (e.g., HIV-1, HBV, HCV, ZIKV) [144–146]; NDUFA13 which is involved in the interferon/all-trans-retinoic acid (IFN/RA) induced cell death.

I then analyzed expression of the IFN signature in the AML9 and AMLIEO20 samples. The signature was overexpressed in the bulk of Chemotherapy-Persistent Blasts compared to untreated samples in both AML9 and AMLIEO20 leukemias (Figure 36, left upper and lower panels). Figure 36 shows the visualization of IFN-signature expression-levels at the single-cell level in the UMAP of bulk and GFP^{high} samples, before and after chemotherapy, for both models. Strikingly, in both models, the IFN signature was markedly overexpressed in the expanded clusters of Chemotherapy-Persistent Blasts, both bulk and GFP^{high}, compared to the other clusters of the same samples, as well as all the clusters of the pre-chemotherapy samples. These data confirm that upregulation of interferon signaling is closely associated with the emergence of chemoresistance in the two AML models. Notably, the vast majority of Chemotherapy-Persistent Blasts seem to derive from specific clusters in the untreated samples, suggesting that only selected cells within the AML samples have the capacity to up-regulate IFN-signalling and adapt to chemotherapy. I am currently investigating the transcriptional properties of these cells.

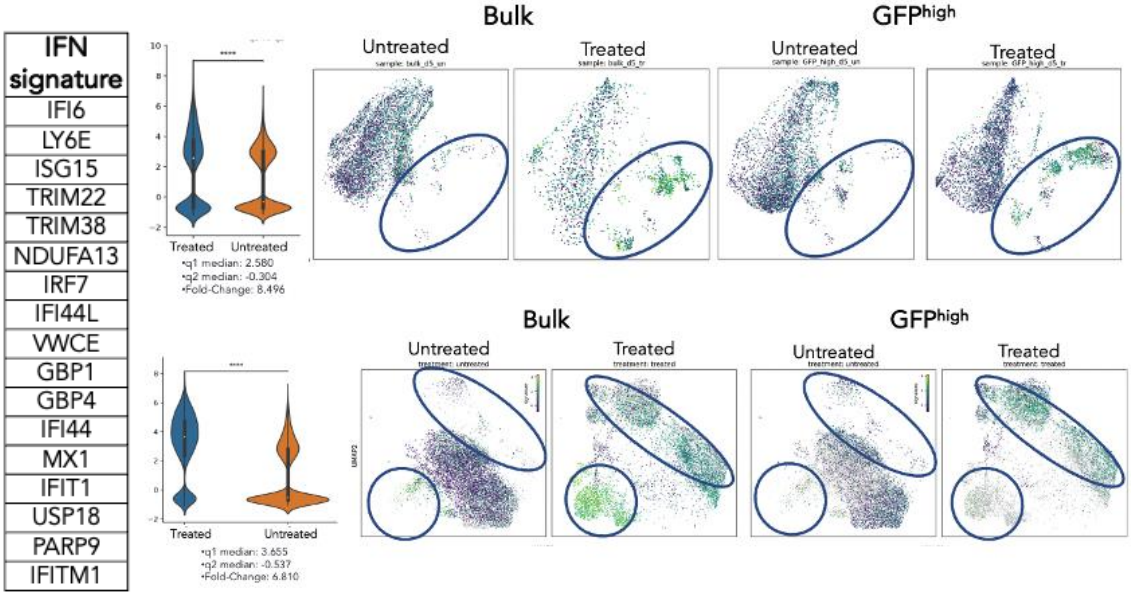

Figure 36 IFN signature is overexpressed in chemo-persistent blasts

Left, IFN chemotherapy persistent blasts signature of 17 genes; violin plot, IFN signature expression in both PDX models; IFN signature expression showed at single cell level in the UMAPs of AML9 and AMLIEO20 PDXs in treated (day 5) versus untreated (day 0) samples. Top AML9, bottom AMLIEO20.

Finally, to preliminarily evaluate the relevance of this signature in a clinical context, I investigated the capacity of the identified IFN signature to predict prognosis in a cohort of 106 TCGA-AML patients treated with the *"7+3"* chemotherapy regimen. As shown in Figure 37, increased expression of the IFN signature significantly correlates with a lower probability of survival of chemotherapy-treated AML patients.

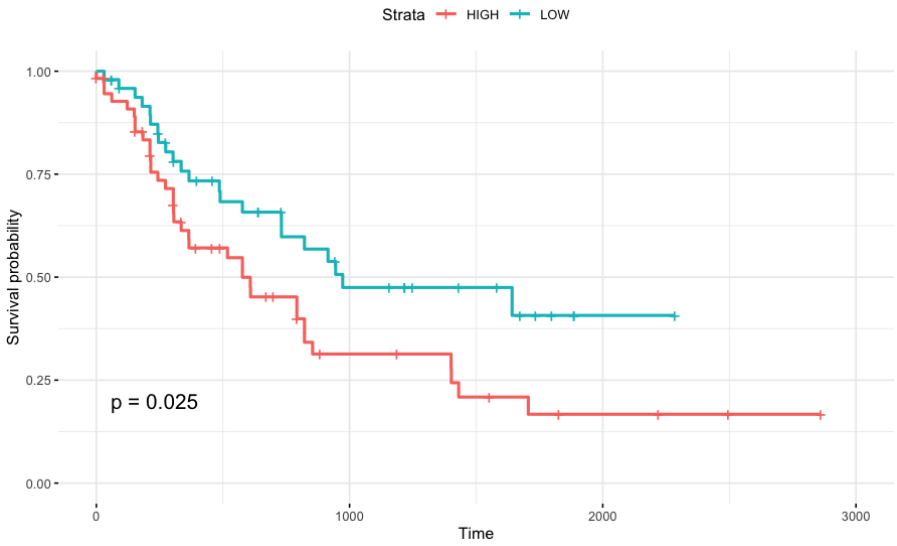

Figure 37 The IFN signature has a prognostic value in AML patients treated with "7+3"

Survival analysis of 106 patients from TGCA_AML database treated with "7+3" chemotherapy regimen, show prognostic value of the signature. High expression (red line) and low expression (light blue line). P-value is indicated (p=0,025).

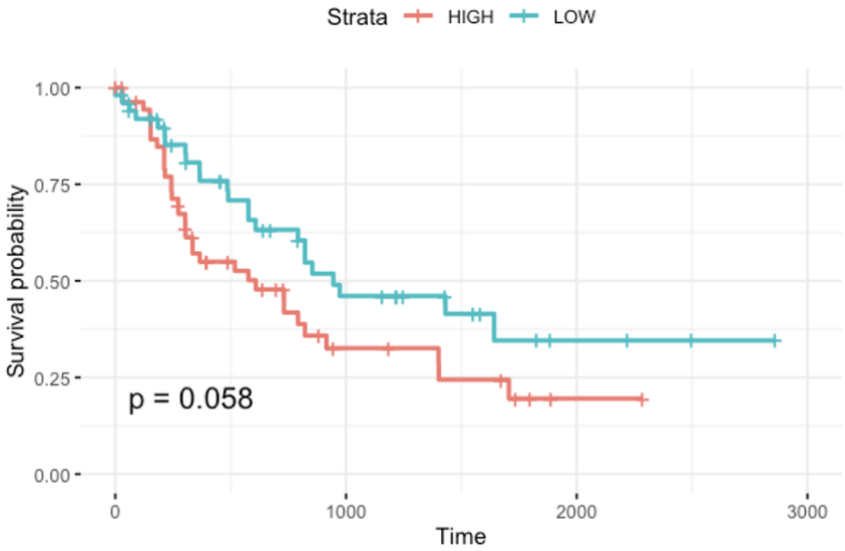

Figure 38 IFI6 has a prognostic value in AML patients treated with "7+3"

Survival analysis of 106 patients from TGCA_AML database treated with "7+3" chemotherapy regimen, show prognostic value of the top differentially expressed gene of the signature (IFI6). High expression (red line) and low expression (light blue line). P-value is indicated (p=0.058).

3.4 Mechanisms of chemoresistance

3.4.1. Selection of the IFI6 IFN-target gene

I then investigated the functional relevance of the IFN-response genes in the establishment of the chemoresistance phenotype. As a first approach, I decided to adopt reverse genetics of the IFI6 gene, an Interferon-target gene that I selected because it is the top upregulated gene in chemo-persistent blasts of both AML PDX models among genes of the IFN signature. Notably, increased expression of IFI6 correlates with a lower probability of survival of chemotherapy-treated AML patients, as observed for the 17-gene IFN signature (Figure 38). Additionally, IFI6 is overexpressed in the bulk of Chemotherapy-Persistent Blasts compared to untreated samples and, at the single-cell level, in the expanded clusters of chemotherapy-Persistent Blasts in both AML9 and AMLIEO20 leukemias (Figure 39). The fold change of IFI6 gene expression between non treated and treated samples is 440861,559 and 340932,751 for AMLIEO20 and AML9, respectively.

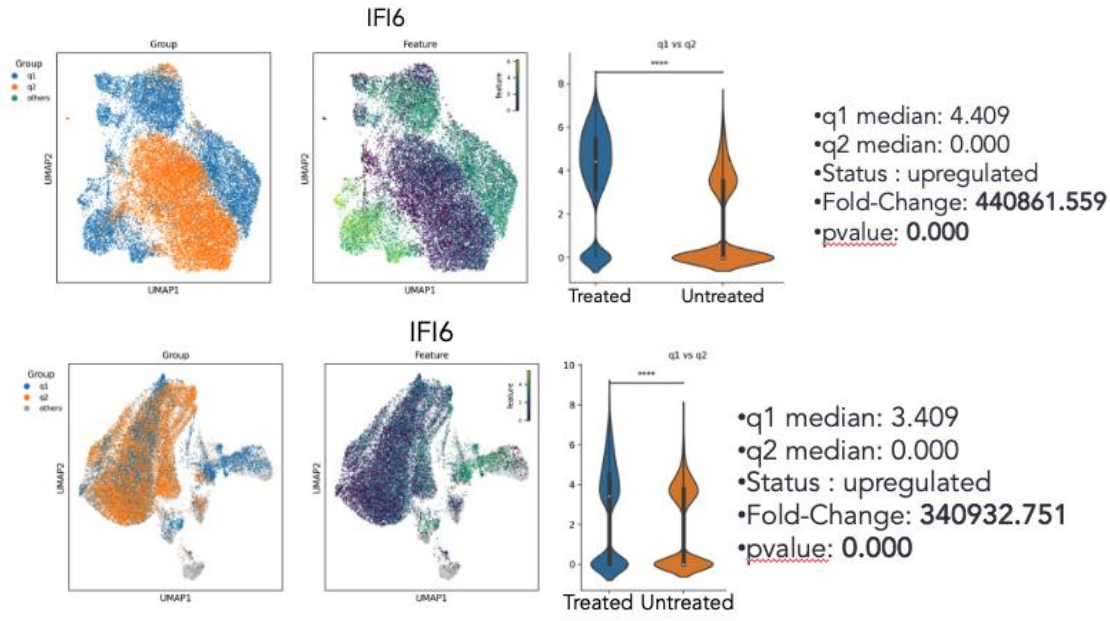

Figure 39 IFI6 is upregulated in day 5 chemo-persistent blasts

UMAP of IFI6 gene expression in AMLIEO20, top, AML9, bottom. Comparison of IFI6 expression levels of chemo-treated versus no chemo-treated BM samples of both AML PDX models. q1 and q2 median indicates normalized median expression of IFI6 gene in both AML PDX models; between the two conditions, chemo treated and non-chemo-treated it is upregulated in the chemo treated samples with a fold change indicated. The p-value is less then 0,0005.

3.4.2. IFI6 silencing does not affect kinetics of leukemia growth *in vivo*

I first assessed the effect of IFI6 silencing on leukemia outgrowth. To this end, I cloned two different shRNAs targeting the IFI6 gene into an RFP-expressing lentiviral plasmid (pRSI16-U6-sh-HTS6-UbiC-TagRFP-2A-Puro), generated viral particles as described in Methods, and infected target cells (AMLIEO20 and AML9 PDX blasts) at an MOI of 5. After 3 days of puromycin selection, 70-80% of cells homogeneously expressed RFP for both shRNAs tested in both AML9 (Figure 40; right panel) and AMLIEO20 (Figure 41; right panel) models. Consistently, real-time qPCR analysis using specific IFI6 primers showed an 80-90% reduction in IFI6 expression in cells expressing either of the two shIFI6 in both models (Figure 40; left panel for AML9; Figure 41; left panel for AMLIEO20).

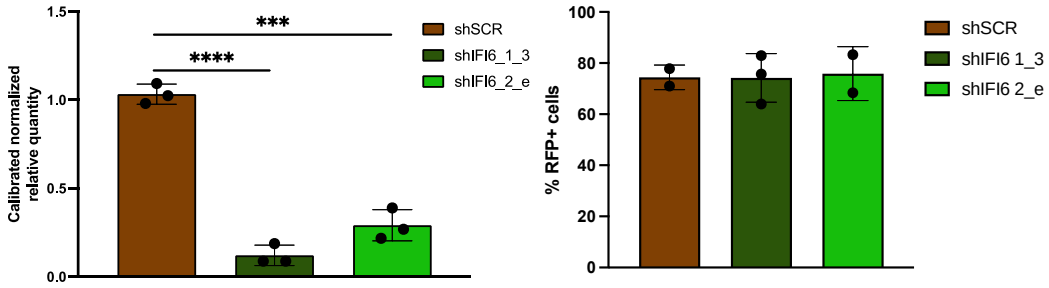

Figure 40. In vitro generation of IFI6-depleted blasts in AML9 PDX model

*Left, Real-time-qPCR analysis of knock-down efficacy of infected blasts, the extent of knock-down was quantified by using the scrambled infected cells as calibrator. (*** P < 0.001, **** P < 0.0001 by Unpaired t-test). Right, FACS analysis of RFP+ infected cells with shSCR and the two different shRNAs against IFI6 after 3 days of puromycin selection, right.*

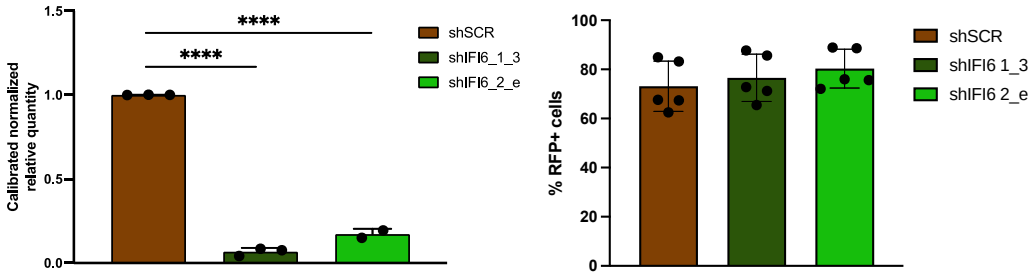

Figure 41 In vitro generation of IFI6-depleted blasts in AMLIEO20 PDX model

*Left, Real-time-qPCR analysis of knock-down efficacy of infected blasts, bottom center, the extent of knock-down was quantified by using the scrambled infected cells as calibrator. (**** P < 0.0001 by Unpaired t-test). Right, FACS analysis of RFP+ infected cells with shSCR and the two different shRNAs against IFI6 after 3 days of puromycin selection, top right.*

Blasts isolated from either PDX models lose viability in culture after extended *in vitro* culture, as expected for primary AML blasts. Therefore, to evaluate the effects of IFI6 silencing on leukemia outgrowth, for each experiment, I generated fresh IFI6-interfered and control scrambled-sh blasts and monitored the effect of silencing by FACS analysis of RFP expression and qPCR analyses of IFI6 expression. In all cases, I obtained results similar to those shown in Figures 40 and 41. A representative experiment is shown in Figure 42, which shows parallel confirmation of IFI6 downregulation also at the protein level by Western blotting analysis using specific anti-IFI6 antibodies (Figure 43). Verification of IFI6 expression levels in all experiments that will be presented in the following sections will not be shown further.

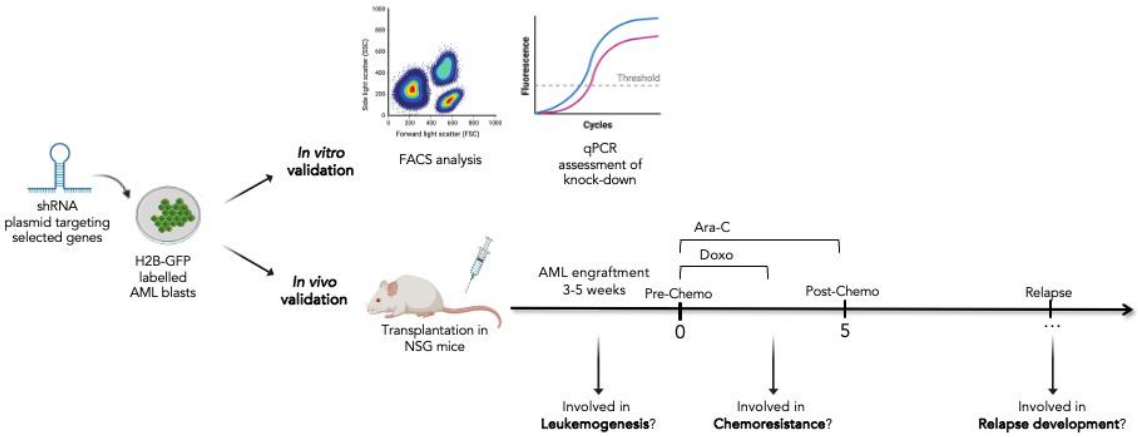

Figure 42 IFI6 in vivo validation experimental scheme

AMLIEO20 and AML9 blasts are infected at MOI=5 with pRSI16-U6-sh-HTS6-UbiC-TagRFP-2A-Puro plasmid cloned with shRNA sequences for IFI6 gene. In vitro the knock down is assessed by FACS analysis of RFP+ blasts and by RT-qPCR analysis after 3 days of puromycin selection. In vivo NSG mice are transplanted with IFI6-expressing blasts after 3 days of puromycin selection. Mice are followed by weekly bleeding to monitor leukemia development. Upon engraftment (around 20% for AMLIEO20 and around 2-5% for AML9) mice are treated with "5+3" chemotherapy regimen.

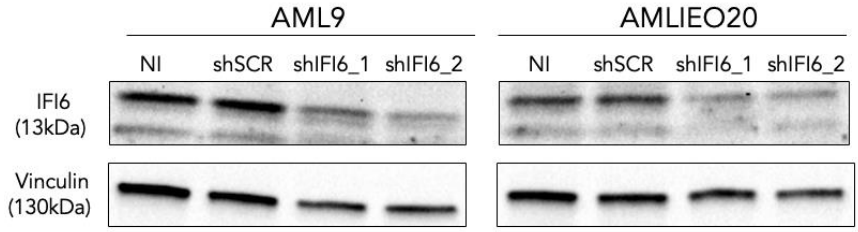

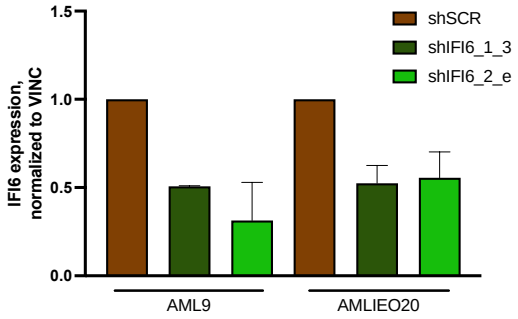

Figure 43 IFI6 protein expression is significantly downregulated in shIFI6-expressing blasts

Western blot analysis of shIFI6-expressing blasts of AML9 and AMLIEO20 PDX models, top. Protein quantification normalized on vinculin housekeeping gene of two different shIFI6-expressing blasts is shown for both AML PDX models, bottom.

A schematic representation of the experimental protocol for the *in vivo* validation of IFI6 silencing is presented in Figure 42. AML9 or AMLIEO20 target cells were infected with the two different IFI6 shRNAs - expressing or control scrambled (shSCR) lentiviruses at an MOI of 5, and, upon confirmation of IFI6 silencing, cells were injected into NSG recipient mice. For each experimental arm, half of the mice were treated with the "3+5" chemotherapy regimen, while the other half was left untreated. Mice were monitored for the frequency of PB human blasts, by FACS analysis of PB CD45+ blasts, until disease relapse.

For AMLIEO20, I transplanted 9 mice with shSCR-infected blasts, 10 with shIFI6_1_3-infected blasts, and 8 mice with shIFI6_2-infected blasts. 6 mice were transplanted with non-infected (NI) blasts. shSCR transduction did not modify latency, growth kinetics, chemotherapy response, or relapse kinetics of the AMLIEO20 leukemia (Figure 44; top panels). The silenced leukemias, instead, showed a significantly reduced frequency of engraftment and delayed latency. Specifically, we observed engraftment in only 1 mouse out of 10 with the shIFI6_1_3 leukemias and 3 out of 8 with the shIFI6_2 leukemias. Latency of leukemia engraftment in the 4 engrafted mice was 24, 11, 15 and 20 weeks (Figure 44, bottom panels), significantly longer than that observed with control AMLIEO20 leukemias (approximately 7 weeks). Notably, once engrafted, the leukemias expanded rapidly, with growth kinetics indistinguishable from those of the control AMLIEO20 leukemias. qPCR analysis of IFI6 expression in the growing blasts confirmed the silencing effect of the IFI6-sh, thus excluding the possibility that the growing leukemia had selected revertants (Figure 45).

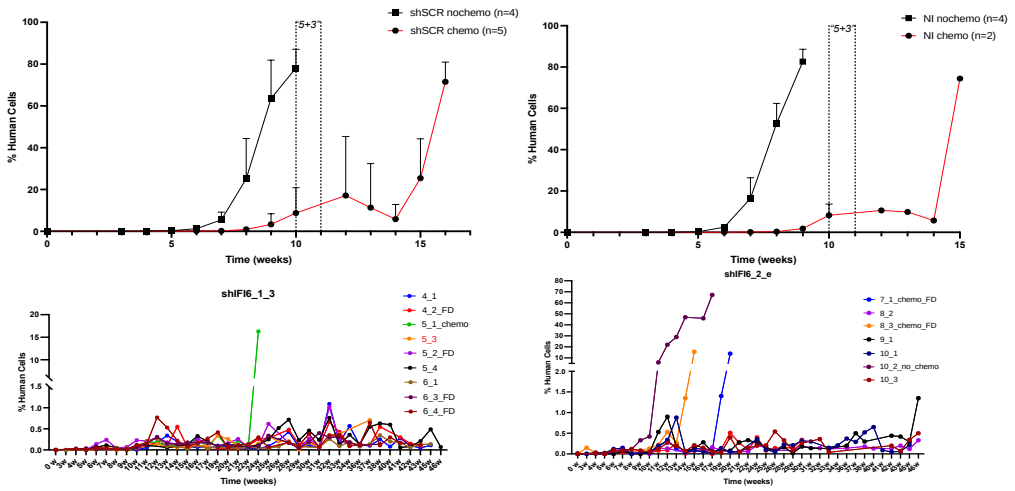

Figure 44 AMLIEO20 IFI6 in vivo validation; increased latency and same kinetic of leukemia growth

Average PB engraftment of shSCR mice, top left; NI mice, top right; black line (non-chemo treated) red line (chemo treated). shIFI6_1_3 mice bottom left; shIFI6_2_e mice bottom right, PB engraftment is shown per single mouse. Dotted lines indicate start and end of chemotherapy treatment. FACS analyses using anti human CD45 antibody.

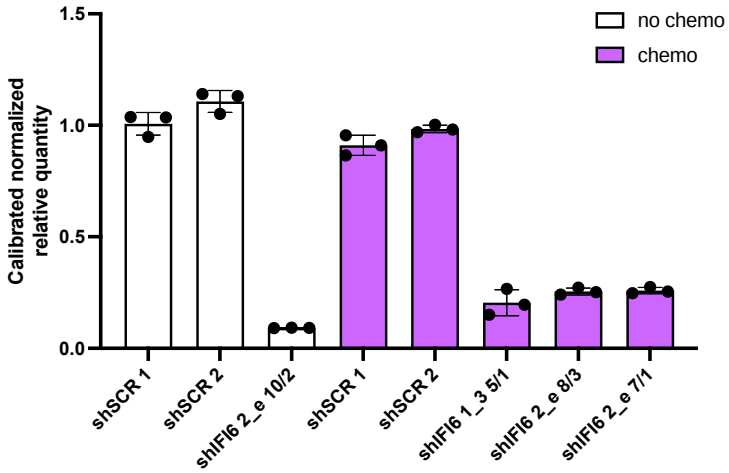

Figure 45 No counter-selection of IFI6-expressing blasts in AMLIEO20

RT-qPCR analysis on BMs of no chemo and chemotherapy treated mice, to assess IFI6 gene knock down. The extent of knock-down was quantified by using the scrambled infected cells as calibrator. Every condition is shown with technical triplicates.

Thus, silencing of IFI6 reduces engraftment efficiency and prolongs the latency of the AMLIEO20 leukemia without interfering with its growth kinetics. To investigate whether this effect of IFI6 silencing on engraftment and latency was due to a decreased number of leukemia-initiating cells (LICs), I designed a limiting dilution transplantation experiment by injecting decreasing numbers of shIFI6-expressing blasts into NSG recipient mice.

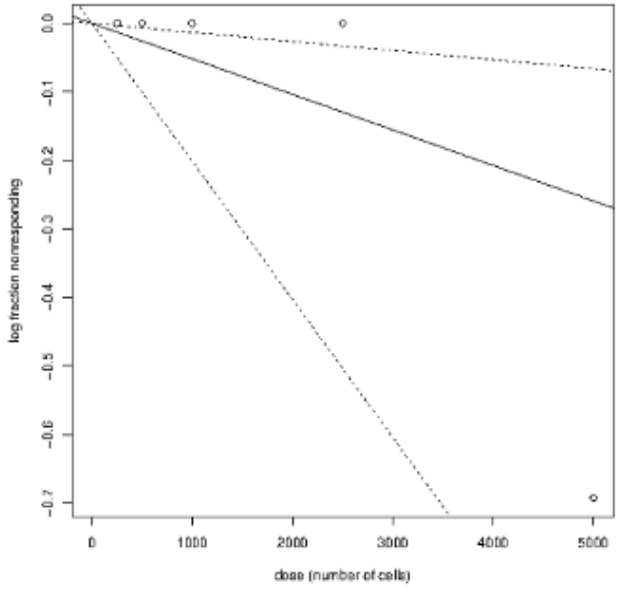

Limiting Dilution Data entered.

Counter	Dose	Tested	Response
1	5000	4	2
2	2500	6	0
3	1000	4	0
4	500	7	0
5	250	5	0

Confidence intervals for 1/(stem cell frequency)

Lower	Estimate	Upper
74887	19267	4958

Figure 46 AMLIEO20 shIFI6 interfered blasts have a reduced LICs frequency

Limiting Dilution Assay results show dramatic reduction of LICs frequency in AMLIEO20 shIFI6 interfered blasts. LICs frequency is calculated by ELDA (http://bioinf.wehi.edu.au/software/elda/).

The calculated LICs frequency in the AMLIEO20 PDX model was previously estimated in my lab to be around 1 in 1,000. Based on these values, I decided to use the following dilution scheme of shIFI6-expressing blasts: 5,000 (4 mice), 2,500 (6 mice), 1,000 (4 mice), 500 (7 mice), and 250 (5 mice). Strikingly, results showed an estimated frequency of LICs in the IFI6-silenced blasts of 1:19,267, significantly lower than that calculated for the control blasts (Figure 46). In conclusion, these data suggest an effect of IFI6 expression on the number of engrafting LICs without affecting the regenerative potential of individual LICs.

For AML9, I transplanted 7 mice with shSCR-infected blasts, 7 with shIFI6_1-infected blasts, and 7 mice with shIFI6_2-infected blasts. As for AMLIEO20, shSCR transduction did not modify latency, growth kinetics, chemotherapy response, or relapse kinetics of the AML9 leukemia (Figure 47, upper panel). For the IFI6sh leukemias, we observed engraftment in 7 mice out of 7 with the shIFI6_1 leukemias and 7 out of 7 with the shIFI6_2 leukemias. Latency of leukemia engraftment in all the engrafted mice was 6-7 weeks (Figure 47, middle and bottom panels), more or less similar to that observed with control AML9 leukemias (approximately 6 weeks). Notably, once engrafted, the leukemias expanded rapidly, with growth kinetics indistinguishable from the control AML9 leukemias.

qPCR analysis of IFI6 expression in the growing blasts confirmed the silencing effect of the IFI6-sh, thus excluding the possibility that the growing leukemia had selected revertants (Figure 48).

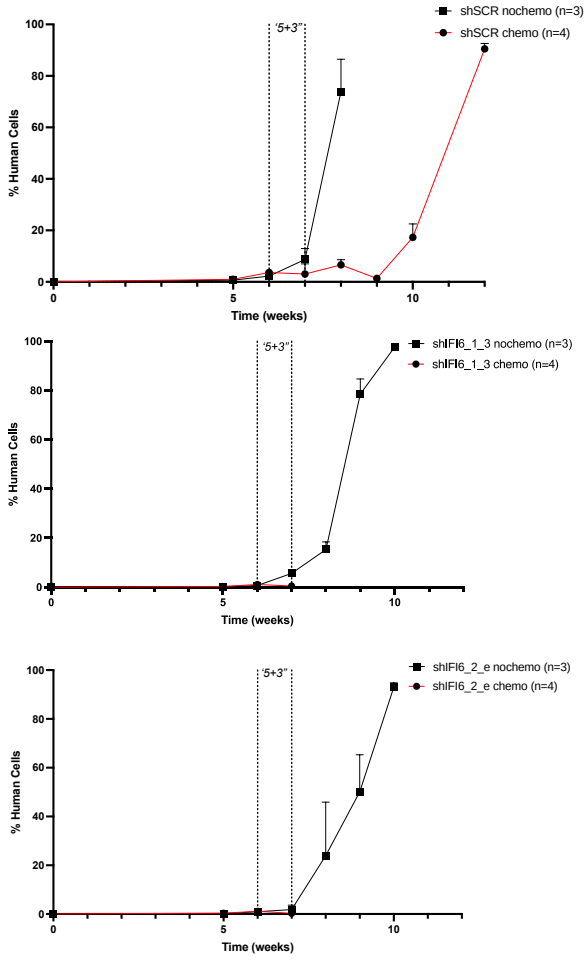

Figure 47 AML9 IFI6 in vivo validation; no effect of the shIFI6 on latency or leukemia growth

Average PB engraftment of shSCR mice, top; NI mice; shIFI6_1_3 mice bottom left; shIFI6_2_e mice bottom right. Dotted lines indicate start and end of chemotherapy treatment. Red lines indicate chemo treated mice and black lines indicate non chemo treated mice. FACS analyses using anti human CD45 antibody.

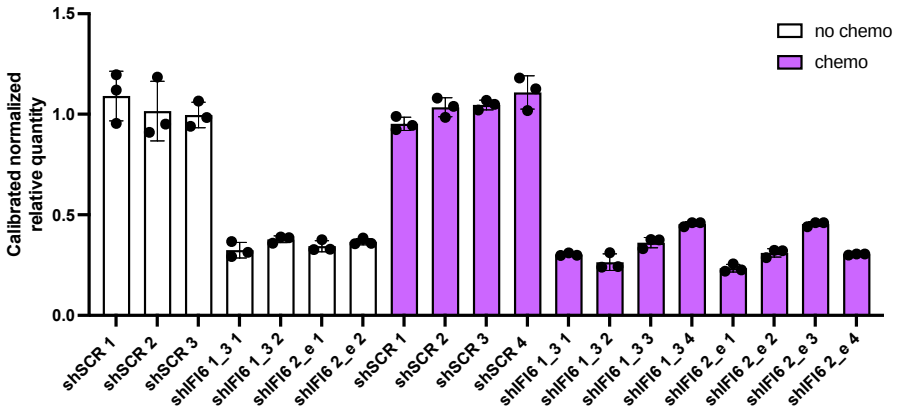

Figure 48 No counter-selection of IFI6-expressing blasts in AML9

RT-qPCR analysis on BMs of no chemo and chemotherapy treated mice, to assess IFI6 gene knock down. The extent of knock-down was quantified by using the scrambled infected cells as calibrator. Every condition is shown in technical triplicates.

Thus, as in the case of AMLIEO20, IFI6 silencing has no effect on the kinetics of leukemia outgrowth. However, unlike AMLIEO20, we did not observe any effect on engraftment efficiency and disease latency. These two properties, however, may depend on the number of LICs in the injected leukemias, which, in the case of AML9, may not be titrated out by IFI6 silencing. To verify this hypothesis, I am currently conducting a limiting dilution transplantation experiment with IFI6-silenced and control AML9 blasts.

3.4.3 IFI6 silencing reverse completely the chemoresistance phenotype of AML9 and AMLIEO20 leukemias

As part of the experiment described above, I waited for the AML9-IFI6sh leukemias (n=8) to reach an engraftment of 2-5% in the PB and the AMLIEO20-IFI6sh leukemias (n=3) to reach an engraftment of 20% before initiating treatment with the *"5+3"* chemotherapy regimen. Surprisingly, all mice harboring the shIFI6-expressing leukemias, in both AML PDX models, died within the week following chemotherapy administration (between 2 to 6 days after the end of the *"5+3"* regimen) (Figure 44 bottom panels and Figure 47 middle and bottom panels). This result is surprising as neither in this experiment nor in other similar experiments conducted to date have we observed early lethality upon chemotherapy. At necropsy, all dead mice showed a normal-sized spleen and no signs of organ infiltration. Strikingly, analyses of the frequency of human blasts (by anti-CD45 FACS analysis) in cell suspensions from the spleen or bone marrow of IFI6sh-expressing leukemias showed the almost complete absence (<1%) of infiltrating human blasts in all mice (3/3 AMLIEO20,

8/8 AML9), compared to control, chemotherapy-untreated mice, which showed instead >80% infiltrating human blasts in all cases (Figure 49). Thus, silencing of IFI6 gene expression completely reverts the chemoresistant phenotype, restoring high sensitivity to chemotherapy.

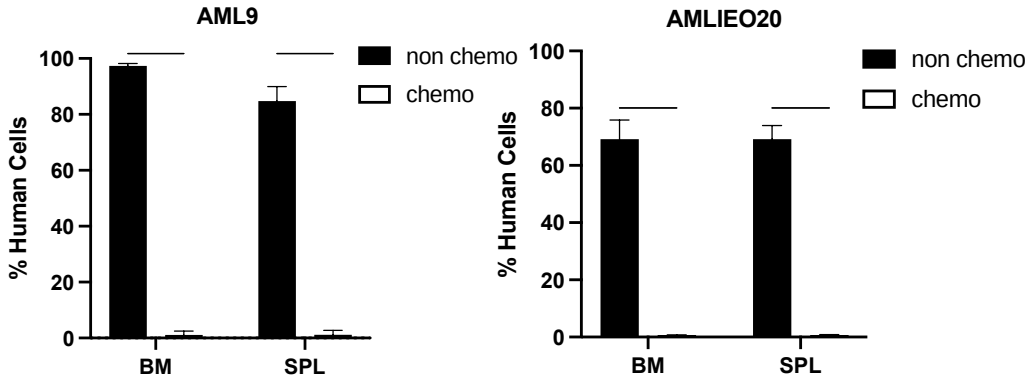

Figure 49 Complete reversion of the chemoresistance phenotype in both AML PDX models

*FACS analysis of BM and SPL blasts (humanCD45 antibody), isolated from shIFI6 non chemo treated and chemo treated NSG mice. (n=3 mice of AMLIEO20, n=8 mice of AML9) (**** P < 0.0001 by 2way ANOVA test).*

The early death of mice during chemotherapy prevented me from documenting the biological effect of chemotherapy on IFI6-silenced blasts. I have initiated an experiment in which a cohort of mice were transplanted with control and IFI6-silenced AMLIEO20 or AML9 leukemias. At engraftment, mice will be treated with the *"5+3"* regimen, sacrificed at day intervals, and cell suspensions from the spleen and bone marrow analyzed for cell viability, apoptosis, and cell cycle.

Regarding the cause of early death in mice with IFI6-silenced and chemotherapy-treated leukemias, I hypothesize that mortality in these mice was due to tumor lysis syndrome. To test this hypothesis, in the same ongoing experiment described above, I will measure changes in uric acid and azotemia levels in the peripheral blood of sacrificed mice. If this hypothesis is confirmed, I will evaluate the effect on early mortality of pretreatment with allopurinol, a well-known therapeutic agent used to reduce uric acid levels associated with critical tumor lysis during treatment in leukemias with hyper-leukocytosis.

3.5. Molecular mechanisms of IFI6-mediated chemoresistance

3.5.1. Identification of myeloid cell lines as model systems to study the effects of IFI6 silencing on chemosensitivity *in vitro*

To investigate whether the effect of IFI6 silencing on chemosensitivity is common to other myeloid leukemias and to identify *in vitro* model systems to study mechanisms of IFI6 chemosensitivity, I analyzed the effects of IFI6 silencing on the sensitivity of established AML cell lines to treatment with Ara-C or Doxorubicin.

To select representative AML cell lines, I first screened the CCLE Broad 2019 RNAseq dataset of hematopoietic cell lines and compiled a list of the top 25 cell lines expressing the IFI6 gene (Figure 50). From this list, I selected the AML cell lines GDM1 and U937 as representative of relatively high and low IFI6 gene expression, respectively. GDM1 and U937 cell lines were then infected with lentiviruses expressing IFI6sh or scrambled sh (shSCR). Three days after puromycin selection, cells were analyzed for RFP and IFI6 expression by FACS analysis and RT-qPCR, respectively. Results, shown in Figure 51, revealed 90% of RFP-positive cells and around 95% reduction of IFI6 expression.

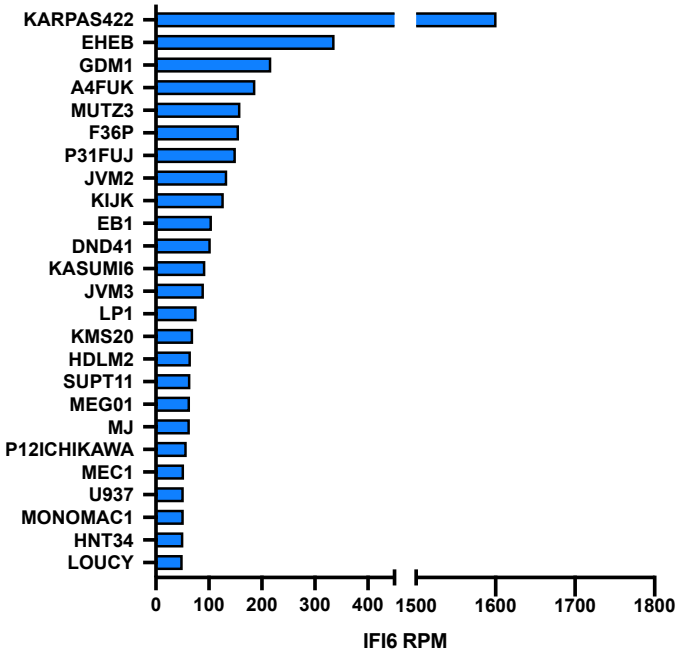

Figure 50 IFI6 expression in hematopoietic cell lines.

List of top 25 IFI6 overexpressing cell line from the ccle_broad_2019 dataset. Cell lines are ranked based on IFI6 mRNA expression expressed as read per million (RPM).

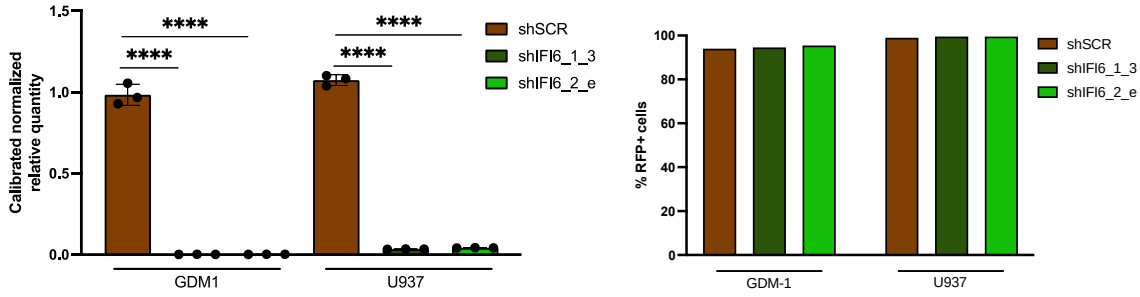

Figure 51 IFI6 knockdown in GDM1 and U937 cells lines

*Left panel, GDM1 and U937 cells are infected with shSCR and the two different shRNAs against IFI6 at MOI=5. RT-qPCR, confirm IFI6 knock-down. The effect of knockdown was quantified by using the scrambled infected cells as calibrator. (**** P < 0.0001 by Unpaired t-test). Right panel FACS analyses for RFP positivity.*

I then analyzed the effects of IFI6 silencing on *in vitro* proliferation by comparing cell proliferation kinetics of cells infected with shIFI6 or shSCR lentiviruses. As shown in Figure 52, no significant difference was observed in proliferation rates in either GDM1 or U937 AML cell lines, indicating that IFI6 knockdown does not impact myeloid-cell proliferation *in vitro*.

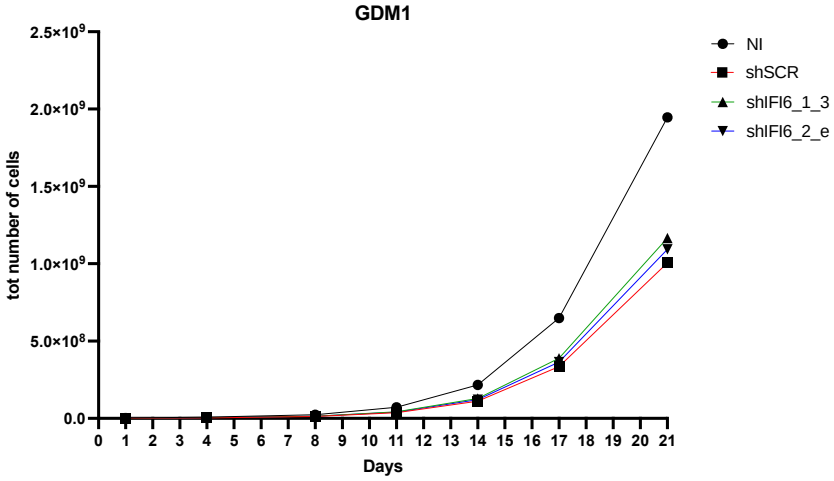

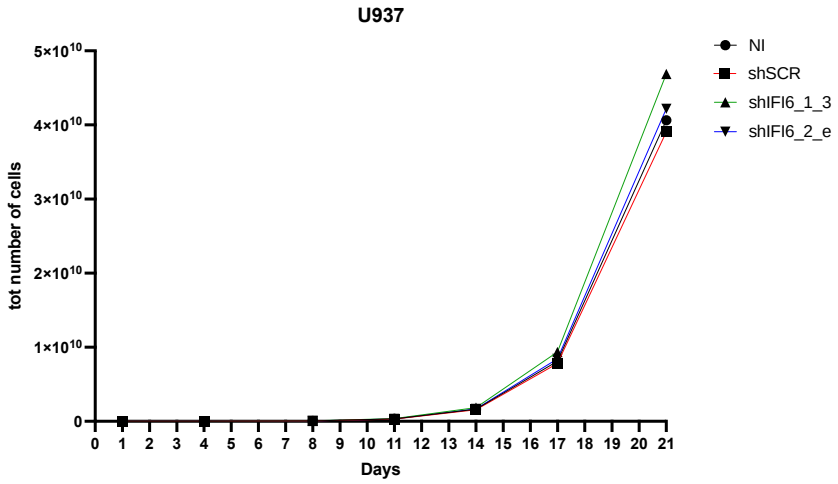

Figure 52 The shIFI6 does not affect proliferation of GDM1 and U937 cell lines

GDM1 and U937 cell are infected with shSCR and the two different shRNAs for IFI6 at MOI=5. Infected cells are counted every 3-4 days and tot number of cells is plotted form day 0, time point of plating.

I then investigated whether IFI6 silencing modifies chemosensitivity of U937 or GDM1 cells, by performing the IC50 drug-sensitivity assays on shIFI6 (two different shIFI6) or shSCR-infected cells treated with Ara-C or Doxorubicin as single agents.

For U937 cells (Figure 53), IC50 values with both the shIFI6 tested decreased significantly at 72 hours of treatment with both Ara-C (0.853 µM and 0.859 µM, respectively, versus 3.520 µM in control cells) and Doxorubicin (shIFI6 0.296 and 0.498 µM; shSCR 1.500 µM). For GDM1 cells (Figure 54), the effect was far less evident, with modestly decreased IC50 values visible at 72 hours with both IFI6sh for Ara-C (shIFI6 6,747 and 12,96 µM; shSCR 10,32 µM), and with only one of the IFI6sh tested for Doxorubicin (shIFI6 2,824 and 5,562 µM; shSCR 6,505 µM).

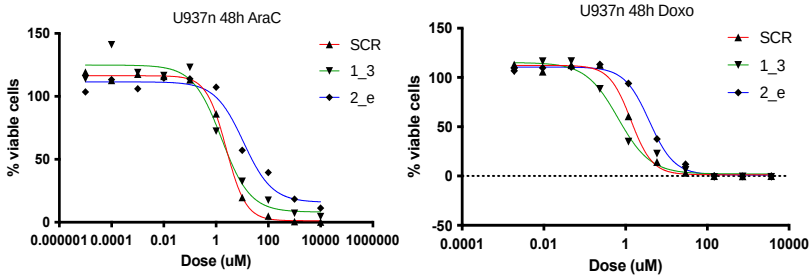

	shSCR	1_3	2_e
48h AraC	2,433	1,621	11,25
72h AraC	3,520	0,853	0,859

	shSCR	1_3	2_e
48h Doxo	1,347	0,655	3,802
72h Doxo	1,500	0,296	0,498

Figure 53 U937 chemotherapy treated cells IC50

IC50 assays in presence of or cytarabine (AraC) doxorubicin (Doxo) in shSCR control and shIFI6 (1_3 and 2_e) infected U937 cells showed in uM; cell viability is shown with increasing concentrations of AraC and Doxo; values are shown as mean of triplicates for each concentration at 48h and 72h after the drug was added.

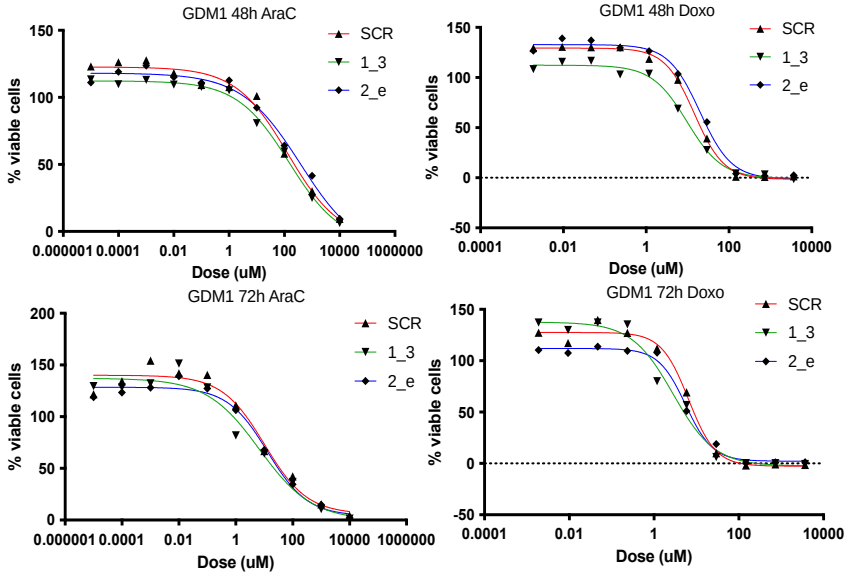

	shSCR	1_3	2_e
48h AraC	133,2	146,6	384,9
72h AraC	10,32	6,747	12,96

	shSCR	1_3	2_e
48h Doxo	14,62	9,709	19,92
72h Doxo	6,505	2,824	5,562

Figure 54 GDM1 chemotherapy treated cells IC50

IC50 assays in presence of or cytarabine (AraC) doxorubicin (Doxo) in shSCR control and shIFI6 (1_3 and 2_e) infected GDM1 cells showed in uM; cell viability is shown with increasing concentrations of AraC and Doxo; values are shown as mean of triplicates for each concentration at 48h and 72h after the drug was added.

In conclusion, these data suggest that IFI6 silencing increases the sensitivity of other myeloid cells to Ara-C and Doxorubicin *in vitro*. Of the two cell lines tested, the effect is more evident in U937 cells compared to GDM1 cells. I am currently expanding the IC50 assay to other myeloid cell lines and characterizing the type of DNA damage response to Ara-C and Doxorubicin in these same cells. Regardless, the availability of at least one myeloid cell line that recapitulates the chemo-sensitizing effect of IFI6 silencing provides a valuable model system for studying the molecular mechanisms underlying the effect of IFI6 silencing.

3.5.2. Mechanisms of IFI6 regulation of chemosensitivity: Working Hypothesis

I hypothesize that IFI6 antagonizes IFN signaling by interacting with and inhibiting cGAS or STING, thereby preventing excessive activation of interferon/cytokines upon chemotherapy-induced DNA damage. This function of IFI6 as an interferon antagonist may serve as a protective mechanism against excessive IFN activation triggered by chemotherapy-induced DNA damage and cGAS-STING activation, which are known to induce senescence or apoptosis of stem and differentiated leukemic cells. Conversely, silencing of IFI6 during chemotherapy might restore the pro-apoptotic/senescence arm of IFN signaling, thus reversing chemoresistance. This hypothesis is based on the following literature data:

IFI6 is an Interferon Stimulated Gene (ISG). IFI6 (IFN alpha inducible protein 6) is a 13-kDa protein with a putative transmembrane domain, mainly localized at the endoplasmic reticulum, transcriptionally activated during the innate immune response to viral infection [147–149].

IFI6 possesses antiviral activity. It inhibits replication of hepatitis B and C virus, and other flaviviruses such as DENV, West Nile Virus or Yellow Fever Virus. Different mechanisms have been proposed for the anti-viral activity of IFI6: i) binding of the chaperone BiP at the ER and prevention of the formation of virus-induced ER membrane invaginations, which are needed for flavivirus replication [150]; ii) inhibition of HCV entry by impairing EGFR mediated CD81/CLDN1 interactions [151]; iii) within the nucleus, reduction of HBV-promoter activity leading to inhibition of viral replication and gene expression [152]; iv) suppression of apoptosis, by regulating the rheostatic balance between bcl-2/bax expression and inhibition of $\Delta\psi(m)$ depolarization during viral infection [153].

IFI6 functions as a negative regulator of innate immune responses. A recent paper [154] has shown that IFI6 is a negative regulator of innate immune responses by modulating RIG-I activation. RIG-1 is a key sensor of dsRNA produced during virus infections; it mediates the transcriptional induction of IFNs and inflammatory proteins. In particular, the authors showed that IFI6: i) down-regulates IFN, ISG, and pro-inflammatory cytokine expression after infections with Influenza A Virus, SARS- CoV-2, and Sendai Virus, or poly(I:C) transfection; ii) binds to poly(I:C) (a dsRNA analog) in cells and *in vitro*; iii) interacts with RIG-I, by co-immunoprecipitation and co-localization experiments; iv) affects modulation of innate immune responses mediated by RIG-I. The authors propose that IFI6 antagonizes viral infections by negatively regulating IFN signalling, through direct interaction with the RIG-1, a sensor of viral-produced dsRNA.

IFI6 is a DNA-damage responsive gene. IFI6 is transcriptionally activated by DNA damage induced by Ionizing Radiation or chemotherapy (mitomycin C, cisplatin) [155].

The cGAS-cGAMP-STING pathway detects cytoplasmic DNA following DNA damage and activates type I IFNs and other cytokines. This immune response can be triggered by various forms of genotoxic stress, including ionizing radiation, chemotherapy, oxidative stress, viral infections, and activation of endogenous retroelements. DNA damage within the nucleus can lead to the accumulation of cytoplasmic DNA in the form of micronuclei or cytoplasmic DNA speckles, which contain both single-stranded (ss) and double-stranded (ds) DNA. Cytoplasmic DNA binds to cGAS in a sequence-independent manner, inducing a conformational change in cGAS's catalytic center. Activated cGAS dimerizes to synthesize cGAMP from GTP and ATP. Damage to mitochondrial can also result in the accumulation of mitochondrial DNA in the cytosol, subsequently activating cGAS. cGAMP acts as a second messenger to activate STING on the endoplasmic reticulum (ER) surface. STING then translocate to the ERGIC compartment and activates the transcription factors IRF3 and NF-κB through the kinases TBK1 and IKK, respectively. IRF3 and NF-κB translocate to the nucleus to induce the expression of IFNs and other cytokines. A schematic view of the STING signaling pathway and our working hypothesis is shown in Figure 55.

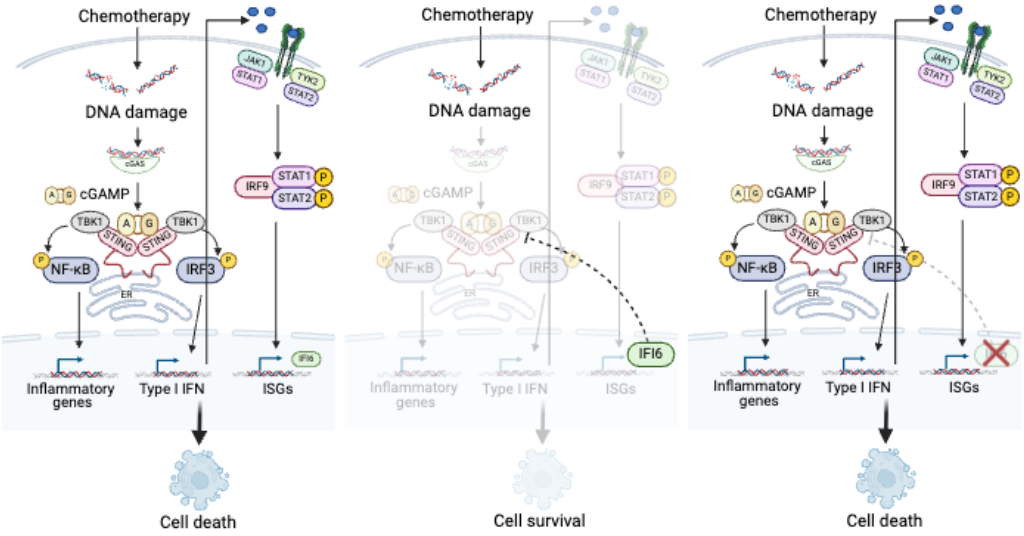

Figure 55 Working Hypothesis

Proposed IFI6 molecular mechanism of AML chemoresistance regulation. left panel: physiological condition; middle panel: IFI6-mediated inhibition of cGAS- STING pathway; right panel: depletion of IFI6 expression by shRNAs.

Working hypothesis. We hypothesize that IFI6 functions as an inhibitor of IFN signaling upon chemotherapy-induced DNA damage. The upregulation of an IFN signaling inhibitor, such as IFI6, could uncouple the pro-inflammatory from the pro-apoptotic or pro-senescence effects of IFN, thereby promoting the emergence of pro-survival pathways that could contribute to the establishment of a chemoresistant phenotype. We hypothesize that the inhibition of IFN signaling by IFI6 may occur at the level of cGAS or STING, based on the findings that IFI6, cGAS, and STING are all activated by DNA damage, and that cGAS-STING are the main mediators of IFN signaling activation upon DNA damage.

3.5.3 Treatment with STING agonists increases chemosensitivity of AML *in vivo*

As a first indirect approach to test my working hypothesis, I investigated the connection between STING pathway-activation and chemosensitivity. Specifically, I aimed to determine if optimal activation of the STING pathway could influence the chemoresistance phenotype of chemoresistant AMLs. Various compounds have been tested in the literature as direct STING agonists, including, among others, Cyclic Dinucleotides (CDNs), such as cyclic di-GMP (c-di-GMP), cyclic di-AMP (c-di-AMP), synthetic forms like 2',2'-cGAMP; 3',2'-cGAMP, identified in Drosophila melanogaster; and the same 2',3'-

cGAMP, (2'3' cyclic GMP-AMP), which is generated intracellularly by mammalian cGAS and shows affinity for hSTING variants.

I have therefore tested whether systemic treatment with cGAMP (2',3'-cGAMP) influences the emergence of chemoresistance of the AMLIEO20 leukemia *in vivo*. NSG mice were transplanted with AMLIEO20 blasts and. once PB engraftment reached 20-30% CD45+ cells, randomized into four treatment groups: control (n=5), cGAMP only (n=5), *"5+3"* chemotherapy only (n=5), and combination cGAMP + *"5+3"* (n=5). cGAMP treatment began one day before initiating the *"5+3"* regimen, resulting in a total of 6 days of cGAMP administration (50mg/kg intravenous injection). Mice were monitored weekly for the frequency of PB blasts.

As expected, *"5+3"* chemotherapy induced a temporary reduction in PB blasts, followed by regrowth with kinetics similar to untreated leukemia (Figure 6). CGAMP treatment alone resulted in a transient pause in PB blast expansion during the 6-day treatment period, followed by immediate regrowth after cessation. Interestingly, the combined administration of cGAMP and chemotherapy resulted in a more pronounced and sustained reduction in PB blasts compared to either treatment alone (Figure 56). These findings suggest that cGAMP treatment has the potential to enhance chemosensitivity, possibly through activation of the STING pathway.

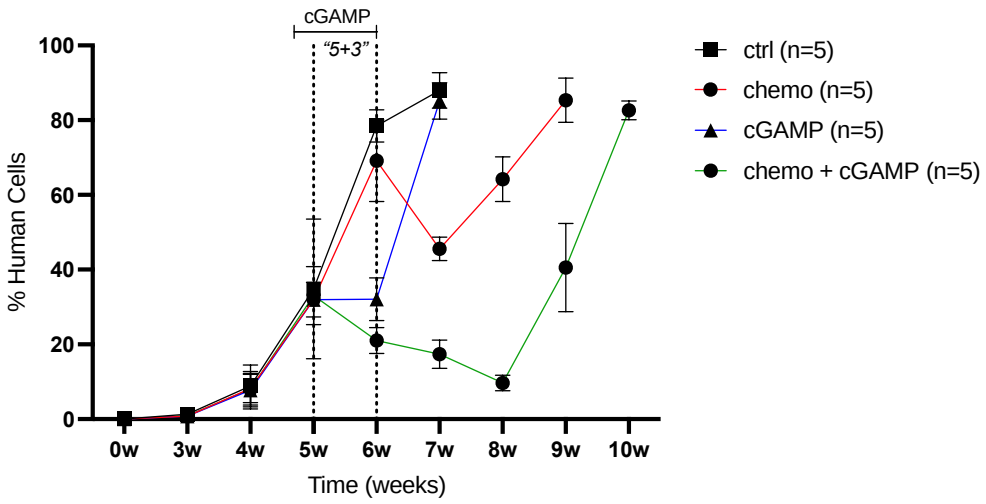

Figure 56 cGAMP treatment increases chemosensitivity in AMLIEO20

Average weekly PB engraftment based in FACS analyses (human CD45 antibody). Black line, control mice; red line chemotherapy treated mice; blue line cGAMP treated mice (50mg/kg); green line cGAMP (50mg/kg) + chemotherapy treated mice. Dotted lines indicate start and end of chemotherapy treatment, cGAMP treatment one day prior to chemotherapy and all the 5 days of chemotherapy treatment (for a toral of 6 days of treatment).

A significant limitation of this experiment is the poor pharmacokinetic profile of cGAMP. Its metabolic instability and membrane impermeability hinder optimal drug

delivery to target cells *in vivo*. Fortunately, newer STING agonists with improved properties are being developed, some of which are currently undergoing clinical trials in various cancers. di-ABZI, for example, is a novel non-nucleotide ligand that potently activates STING and exhibits promising antitumor activity in preclinical models [156]. Based on these findings, I have initiated new *in vivo* chemo-sensitization experiments using di-ABZI.

3.5.4. Partial IFI6-STING co-localization in non-chemo-treated cells

To test the hypothesis that IFI6 antagonizes IFN signaling by inhibiting cGAS or STING, I first investigated whether IFI6 and STING or cGAS colocalize in myeloid cells under steady-state conditions or after chemotherapy treatment. To this end, I established experimental protocols for high-resolution immunofluorescence localization of relevant proteins using the GDM and U937 cell lines and commercially available antibodies against IFI6, components of the STING signaling pathway (STING, cGAS, TBK1), and intracellular markers of the ER (RTN3) and ERGIC (LMAN1). Optimal staining conditions, including antibody concentrations and permeabilization protocols, were determined for each antibody. To balance the host for secondary antibody stainings, all possible combinations of antibodies were tested for colocalization experiments. Extensive optimization experiments, not detailed in this thesis, were performed to achieve optimal antibody staining and colocalization. Images were acquired using confocal microscopy.

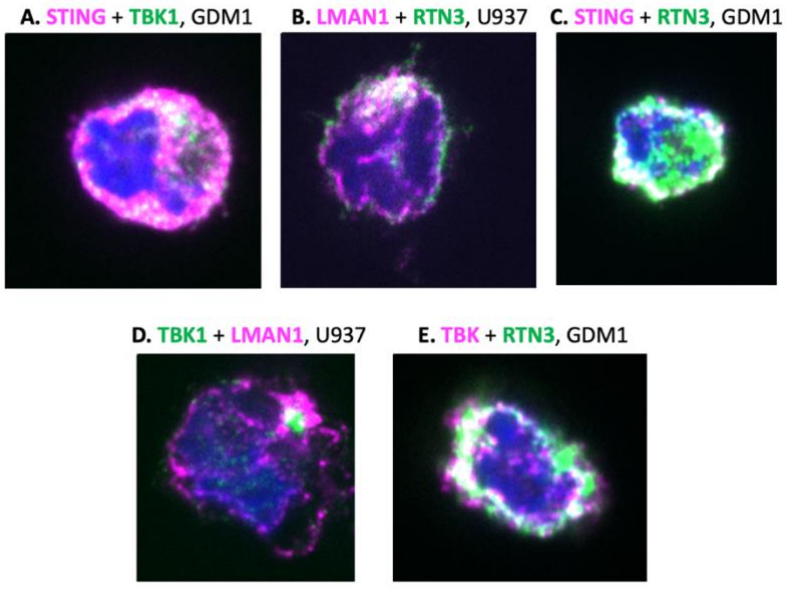

Figure 57 Analysis of localization and co-localization of STING pathway cascade proteins in untreated cells

Multicolor confocal microscopy images showing: A, STING and TBK1 staining in GDM1, B, LMAN1 and RTN3 staining in U937, C, STING and RTN3 staining in GDM1, D, TBK1 and LMAN1 staining in U937, E, TBK1 and RTN3 staining in GDM1. All cells are stained with DAPI.

Initially, I analyzed the localization and colocalization of STING-pathway components with ER and ERGIC compartments under steady-state conditions. As expected, a small degree of colocalization was seen between STING and TBK (Figure 57, panel A). Partial colocalization was observed between LMAN1 (ERGIC marker) and RTN3 (ER marker) (Figure 57, panel B), almost complete colocalization was observed between STING or TBK1 and RTN3 (Figure 57, panels C, E), and partial colocalization was observed between TBK1 and LMAN1 (Figure 57, panel D) (representative images in representative indicated cell lines, GDM1 or U937, are shown in Figure 57).

These observations correlate with the well-established compartmentalization of the STING signaling pathway, with cGAS localized to the plasma membrane, cytosol, and nucleus, and STING and TBK localized to the ER. The modest colocalization of STING and TBK, as well as the modest colocalization of STING or TBK with ERGIC markers, may reflect the existence of a small fraction of STING in an activated state under steady-state conditions in these cells.

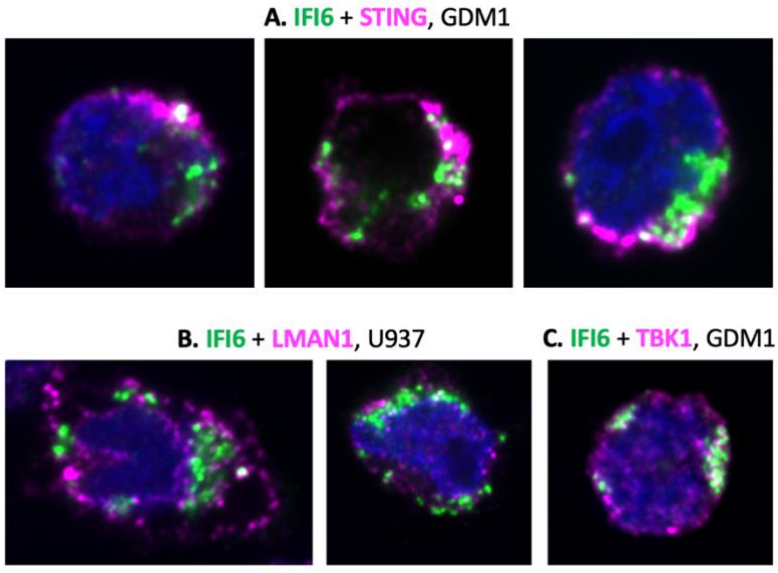

Figure 58 IFI6 partial colocalization with STING in unperturbed conditions

Multicolor confocal microscopy images showing: A, IFI6 and STING (3 representative cells) staining in GDM1, B, IFI6 and LMAN1 staining in U937 (2 representative cells), C, IFI6 and TBK1 staining in GDM1 All cells are stained with DAPI.

Subsequently, I analyzed the intracellular localization of IFI6. Notably, I observed partial colocalization of IFI6 with STING (Figure 58, panel A), TBK (Figure 58, panel C), and the LMAN1 ERGIC marker (Figure 58, panel B) (representative images are shown in Figure 58, in representative indicated GDM1 and U937 cell lines).

Collectively, these experiments established optimal conditions for evaluating the intracellular localization of IFI6 and components of the STING signaling pathway and demonstrated partial colocalization of IFI6 with STING, possibly due to partial activation of the STING pathway under steady-state conditions.

3.5.5. Massive IFI6-STING co-localization in AraC-treated cells

I have then analyzed the effect of Ara-C and Doxorubicin on the intracellular localization of IFI6 and STING, using the antibodies and staining protocols described above. To this end, U937 and GDM1 cells were treated with 4 and 12 uM Ara-C and 2 and 7 uM Doxorubicin, corresponding to relatively high doses within the range used to calculate IC50 values for these cell lines (see Figure 53 and figure 54). Cells were then analyzed at three time points after chemotherapy: 1, 3, and 6 hours.

A detailed analysis of this experiment is still ongoing. However, preliminary analyses of GDM1 cell line have shown that, strikingly, after treatment with Ara-C, nearly all IFI6 protein re-localizes in proximity to STING, with maximal re-localization at 6 hours in both cell lines (representative results for the GDM1 cell line are shown in Figure 59, panel A).

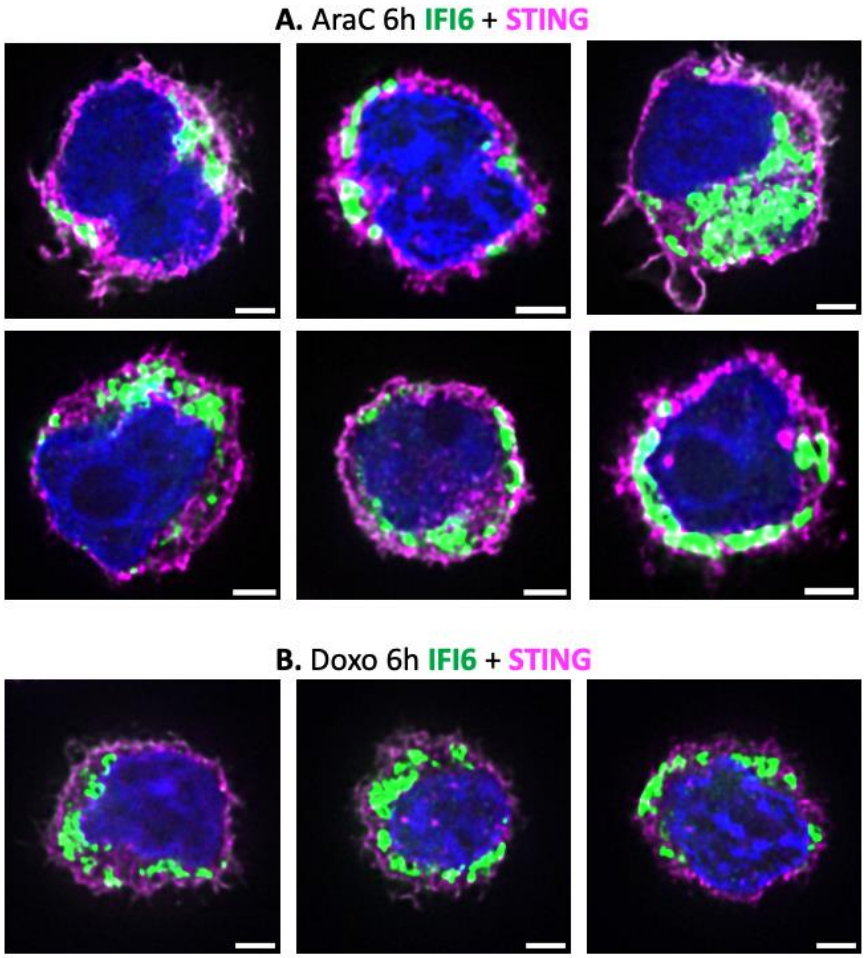

Figure 59 IFI6-STING increased colocalization upon chemotherapy

Multicolor confocal microscopy images showing: A, IFI6 and STING (6 representative cells) staining in GDM1 6hours AraC treated, B, IFI6 and STING (3 representative cells) staining in GDM1 6hours Doxorubicin treated. All cells are stained with DAPI. Scale bar 2um.

However, analyses of the effects of doxorubicin showed a less dramatic effect of this drug on the re-localization of IFI6 in proximity to STING (representative results for the GDM1 cell line are shown in Figure 59, panel B).

In the same experiment, I also observed a marked increase in the anti-IFI6 signal after Ara-C treatment (Figure 60, middle panel), already visible at 2 hours and significantly enhanced at 6 hours. Notably, the STING signal also appeared to be increased following Doxorubicin (Figure 60, bottom panel) treatment, with a seemingly similar kinetics.

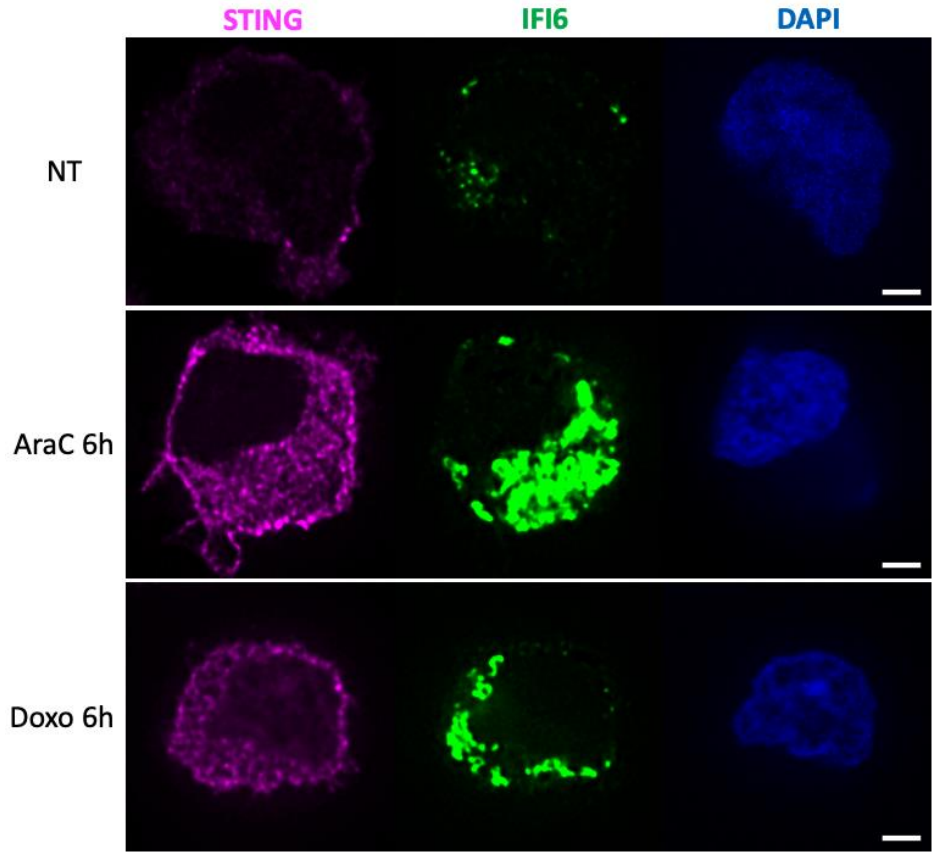

Figure 60 IFI6 and STING upregulation after chemotherapy treatment

Multicolor confocal microscopy images showing: upper panel, non treated (NT) GDM1 cell, IFI6 and STING staining showed separately; middle panel AraC 6 hours treated GDM1 cells IFI6 and STING staining showed separately; bottom panel, Doxorubicin 6 hours treated GDM1cells IFI6 and STING stainings showed separately. All cells are stained with DAPI. Scale bar 2um.

Taken together, these results demonstrate that Ara-C induces increased expression of IFI6 and STING, and massive the re-localization of IFI6 in proximity to STING, suggesting that Ara-C-induced DNA damage causes the recruitment of IFI6 to the sites of STING-TBK activation. The reasons for the less pronounced effect of doxorubicin are unclear. I will conduct further experiments to evaluate the effects on IFI6 localization of different concentrations of doxorubicin (and Ara-C) at later time points, and correlate results with the extent of DNA or mitochondrial DNA damage and IFN signaling activation induced by the two drugs.

4 DISCUSSION

Chemoresistance is recognized as one of the main causes of AML relapse and AML-related deaths. Therefore, understanding causes and mechanisms of chemoresistance would be a big step forward to better characterize AML disease and improving current therapeutic approaches.

Intratumor heterogeneity is a key determinant of tumor progression and a leading cause of failure of current anti-cancer treatments and emergence of drug-resistant disease [157]. Two levels of intratumor heterogeneity are generally recognized: genetic and phenotypic. Cancer genomes contain high numbers of somatic alterations within individual tumors [158]. While some of these are found at high allelic frequencies and are likely to appear early during tumor evolution, others are present at lower frequencies within tumor subclones and are acquired later (sub-clonal genetic heterogeneity). Intratumor phenotypic heterogeneity includes traits that are critical for tumor development/maintenance, such as proliferation, differentiation, dormancy, migration, and senescence. Only rare cancer cells are capable of propagating tumors in model systems, so-called cancer stem cells (CSCs), adding a further level of phenotypic heterogeneity. CSCs retain the ability to divide asymmetrically, suggesting that they contribute to generating phenotypic heterogeneity [159]. Notably, cancer cells can transit from one phenotypic state to another, a phenomenon referred to as cell plasticity (such as de- or trans-differentiation, SC reprogramming, and epithelial-to- mesenchymal transition) [160]. As analyses of clonal relationships between phenotypic states have led to conflicting conclusions, the mechanistic relationship between genetic and phenotypic heterogeneities remains unclear.

The most accepted interpretation of the role of intratumor heterogeneity during tumor progression and drug-resistance, based on concepts of Darwinian evolution, postulates that cancer cells accumulate random genetic mutations that generate phenotypic heterogeneity. The best-fitted phenotypes are then selected by the changing environment (natural selection). A striking example is the selection, during treatment, of DNA mutations that confer drug resistance. Additionally, tumors might follow the laws of neutral genetic drift, leading to the co-existence of biologically equivalent subclones [161]. Alternatively, rare genetic subclones may contribute to tumorigenesis or drug-resistance via non–cell autonomous mechanisms (sub-clonal cooperativity) [162]. For instance, rare subclones in glioblastomas can produce

cytokines that are indispensable for tumor growth, and rare subclones in cetuximab- resistant colorectal cancers can carry drug-resistant mutations.

Intratumoral phenotypic heterogeneity can also be generated without DNA modifications, as cancer cells respond to the changing environment by adopting specific phenotypic states (phenotypic adaptation), which also contribute to tumor progression and drug resistance. Emerging evidence suggests that transmission of transcription factors and/or chromatin changes (epialleles) to daughter cells during mitosis are plausible mechanisms of non-genetic inheritable adaptation [163].

The hypothesis that I tested in my thesis project is that chemotherapy resistance results from the capacity of leukemic cells to dynamically adapt their phenotype to drugs, thus undergoing the so-called phenotypic plasticity. The main questions I wanted to answer in my doctoral work have been: i. which phenotypic states are associated with AML chemoresistance? ii. are they associated with specific cellular state (e.g., quiescence) or specific cellular lineages (e.g., sub-clones)? iii. which are the molecular determinants of the resistant/persistent phenotype? iv. can they be exploited to prevent chemoresistance?

In this context, the first aim has been to generate AML PDX models of chemoresistance, to then investigate cell-cycle and clonal dynamics of AML during chemotherapy treatment, to characterize the transcriptional and phenotypic states of chemotherapy-persistent blasts and establish their role in relapse development, and finally to identify candidate genes responsible of the chemo-resistance and relapse and validate their role in leukemogenesis and chemoresistance.

Generation of AML PDX models stems from the critical need in the field of an *in vivo* model of AML chemoresistance, since true chemoresistant-AML mouse model are not available, and the only available models are characterized by transient drug-resistance[38]. I successfully generated the first two human AML PDX models (AML9 and AMLIEO20) that exhibit non-genetic chemoresistance to standard of care induction chemotherapy. These models are particularly significant as they closely mimic the treatment regimen used in clinical settings, specifically the *"7+3"* induction chemotherapy regimen. In these PDX models, a modified *"5+3"* chemotherapy regimen was applied, which resulted in complete (AML9) or partial (AMLIEO20) disease remission. Despite these differences in remission dynamics, both AML PDXs eventually relapsed, albeit at distinct kinetics. After treatment,

AML9 model responded to chemotherapy and it developed relapse after 3 weeks of remission. AMLIEO20 model responded to chemotherapy in the week after treatment, and I observed a frank re-expansion of the disease in the week right after partial response to chemotherapy. In both models, chemotherapy persistent blasts and relapsing leukemias are chemoresistant. The chemo-resistant phenotype of relapsing leukemias has been demonstrated *in vivo,* by retreating mice with the same chemotherapy regimen at relapse time-point. Interestingly, the acquisition of chemoresistance in both PDX models did not appear to be driven by the selection of specific DNA mutations, indicating and pointing out to a non-genetic mechanism of resistance.

A key observation in the AMLIEO20 PDX model was its manifestation of primary resistance to the *"5+3"* chemotherapy regimen. Following chemotherapy treatment, the model entered a transient remission phase characterized by a PB blast percentage that approximated the baseline percentage at the onset of treatment. However, within one week of entering this remission phase, all mice uniformly developed disease relapse with a re-expansion of the disease. Conversely, the AML9 PDX model exhibited secondary resistance to the *"5+3"* regimen. In particular, following chemotherapy administration, the leukemia achieved a more prolonged remission period of approximately three weeks before all mice uniformly developed relapse.

One important main feature of both AML PDX models of chemoresistance is the incorporation of a label-retaining system which allow the monitoring and the isolation of quiescent cells. In particular, the PDX models are molecularly engineered with a Tet-Off H2B-GFP models. Upon doxycycline chasing I can distinguish three main sub-population of blasts according to their GFP signals: GFP^{high} blasts (0 divisions) are quiescent cells, GFP^{low} blasts (1-8 divisions) are slowly proliferating cells and GFP^{neg} blasts (> 8 divisions) are fast proliferating cells. These models allowed me to characterize the cell cycle properties of chemotherapy-persistent blasts. I characterized the cell cycle properties of chemo-persistent blasts in PB, BM and SPL of non-chemo and chemo-treated mice and I demonstrated that though quiescent blasts (GFP^{high}) are significantly enriched after chemotherapy, the treatment does not select quiescent cells specifically, since both quiescent and proliferating blasts survive chemotherapy.

Then I decided to characterize clonal dynamics of AML during chemotherapy treatment, in order to identify (if any) specific chemo-persistent cellular clones. To do so I

infected target cells with a lentiviral library of around 10 x 10^6 different barcodes (GBC Perturb-Seq library) at a low MOI in order to have a single barcode integration per infected cells. Then, after FACS-sorting of infected cells (using the BFP reporter fluorescence of the library), I transplanted recipient NSG mice and longitudinally followed their clonal dynamics upon chemotherapy treatment. Thus, by lineage tracing experiments, I studied the clonal dynamics of AML pre- and post-chemotherapy, by longitudinally following the PB and BM of chemo and non-chemotherapy treated mice. AMLs were near-monoclonal both in PB and BM in non-chemo-treated mice and the clonal structure of AML was not modified by chemotherapy treatment, with the exception of a few clones with low fitness that slightly expand post-chemotherapy, going from a frequency of 0,1% to around 5%. This suggests that chemotherapy does not select any specific cellular lineage or clones.

Moreover, I demonstrated that chemotherapy-persistent blasts are truly chemoresistant *in vitro* (IC50 analysis of treated and non-treated blasts) and that are capable to regenerate a leukemia (e.g., they contain Leukemia Initiating Cells - LICs). I then tested the tumorigenic potential of quiescent *versus* proliferating cells charactering the GFP^{high} subpopulation of blasts in both AML PDX models. I clearly demonstrated, by limiting dilution transplantation assay, that at steady-state (at early time points after chasing, after 5 days of doxycycline chasing) the frequency of LICs in GFP^{high} blasts is significantly higher compare to GFP^{low} blasts. Thus, quiescent GFP^{high} blasts are probably the only cells, as compared to proliferative cells, endowed with tumorigenic and regenerative properties. The presence of GFP^{high} cells with regenerative potential in the chemotherapy persistent blasts suggest that quiescent cells, though not a specific trait of chemoresistance, are integral for the ensuing chemoresistance relapse.

The rise of drug resistance poses a significant obstacle to the success of anticancer therapies. Drug-persistent cells in various types of cancer have been recognized only in the last two decades, yet many aspects of their biology remain elusive. Although the term "persisters" is commonly used to describe quiescent, drug-tolerant cells, tumors actually consist of a plethora of cell states and phenotypes, including dormant, senescent, and stem-like cells. It's widely accepted that during drug exposure (e.g., chemotherapy), tumor cells can activate transcriptomic and epigenetic pathways associated with drug tolerance, temporarily/transiently increasing alternative survival strategies and resistance genes, which contributes to a drug-resistant or chemo-persistent state [164]. In this study I explored the molecular mechanisms and characteristics of persistent blasts in AML following induction

chemotherapy treatment, aiming to clarify their transcriptomic profiles and identify key molecular and biological targets involved in chemoresistance.

To study the transcriptomic properties of chemotherapy-persistent blasts, I characterized the AML PDX models by performing scRNAseq. I analyzed BM samples pre-chemotherapy (day 0) and immediately after chemotherapy (day 5) of unfractionated/bulk human (FACS sorted based on CD45 positivity) and among them the quiescent GFP^{high} population.

I showed that chemo-persistent blasts are characterized by specific transcriptional features: undifferentiated phenotype and up-regulation of the interferon signalling pathway. Furthermore, the chemoresistance-associated phenotype is shared by both persistent-proliferating and persistent-quiescent blasts, thus reinforcing that quiescence is not a specific trait of chemoresistance. As mentioned, quiescent cells are the only endowed with regenerative potential, suggesting that they are critical for the relapsing properties of chemo-persistent blasts.

I showed that activation of the interferon signalling pathway is a distinguishing feature of cells that survive chemotherapy treatment and that cells with activated Interferon signalling are present at low frequency at steady-state, prior to chemotherapy. Levels of FN pathway activation in cells prior to chemotherapy are however significantly lower than in the persistent blasts, suggesting that chemotherapy induces further adaptive responses, rather than simply selecting a pre-existing phenotype.

I generated a signature of interferon chemoresistance, by performing differential expression analysis of treated (day 5) versus non treated (day 0) expanded transcriptional-clusters. I then took the top 50 DEGs *per* cluster and manually curated all the genes in common between AML9 and AMLIEO20 models and common between bulk/unfractionated and GFP^{high}. The signature is characterized by 17 genes all belonging to interferon signalling pathway (IFI6, LY6E, ISG15, TRIM22, TRIM38, NDUFA13, IRF7, IFI44L, VWCE, GBP1, GBP4, IFI44, MX1, IFIT1, USP18, PARP9, IFITM1). This signature stratifies prognosis of AML patients in a cohort of 106 patients treated with *"7+3"* induction chemotherapy from the TGCA_AML dataset.

Overall, activation of interferon signalling is a distinguishing feature of cells that survive chemotherapy and the interferon transcriptional-signature have a prognostic value in AML patients treated with induction chemotherapy. Yet, the contribution of activated IFN signalling in establishing chemoresistance in AMLs is unknown.

To address this question, I investigated the role of the top interferon-signalling candidate gene IFI6 in AML leukemogenesis, chemoresistance and relapse development. Notably, IFI6 showed a prognostic value in overall survival of AML patients treated with *"7+3"* induction chemotherapy.

I cloned two different shRNAs against IFI6 and infected AML PDXs target cells. I assessed gene knock down *in vitro* by qRT-PCR and by FACS analysis (using the RFP reporter positivity) and showed infection efficacy of 90% and a gene knock down of around 95%. Then, I performed *in vivo* experiments and I transplanted shIFI6-expressing blasts in recipient NSG mice. I demonstrated that the shSCR expression does not modify the growth and chemoresistance phenotype of AMLIEO20 blasts. Moreover, in the same model, I showed increased latency and reduced frequency of disease engraftment, yet same kinetic of leukemia growth upon IFI6 downregulation. Nevertheless, shIFI6 expressing blasts maintain IFI6 silencing (no counterselection of shIFI6-expressing blasts).

I hypothesized that the observed increase latency of leukemia development observed in shIFI6-transplanted mice, together with the same kinetic of leukemia outgrowth, could be attributed to a decreased number of leukemia initiating cells (LICs) population. I tested this hypothesis by performing limiting dilution assay transplanting serial dilutions of shIFI6-expressing blasts in different cohorts of NSG recipient mice. Previous data obtained in our lab, demonstrated the AMLIEO20 LICs frequency to be approximately 1:1000. I demonstrated that upon IFI6 silencing, the LICs frequency of AMLIEO20 is estimated to be 1:19000, suggesting a significant impact of shIFI6 expression on the proliferative and self-renewal capabilities of leukemia-initiating cells. I did not observe any effect of IFI6-silencing neither on latency nor on the kinetics of leukemia outgrowth, with no counter-selection of IFI6-expressing blasts. I am currently investigating the effect of IFI6 on AML9 LICs under limiting conditions of leukemia engraftment.

Strikingly, I also demonstrated that chemotherapy completely eradicates AML in all IFI6-silenced mice treated with the *"5+3"* regimen, thus reverting the chemoresistance phenotype in both BM and SPL of chemo-treated mice. Notably, all shIFI6-expressing mice, treated with *"5+3"* chemotherapy regimen, in both AML PDX models, died in the week following chemotherapy administration (specifically between 2 to 6 days after *"5+3"* regimen). I postulated that this observed mortality is due to a blast lysis syndrome [165], characterized by hyperuricemia, hyperkalemia, hyperphosphatemia, hypocalcemia and acute

renal failure, thus/ultimately leading to mouse death. In order to test this hypothesis, I plan to perform *in vivo* time course experiments, to monitor shIFI6-expressing blasts cell-death post-chemotherapy treatment and to measure changes in ureic acid and azotemia levels in the PB of mice which will be sacrificed each day during *"5+3"* chemotherapy regimen. Altogether these data clearly showed that IFI6 gene is dispensable for leukemia growth and critical to the establishment of the chemoresistance phenotype in AMLs.

Interferon-alpha inducible protein 6 (IFI6) was first identified as a pivotal interferon-stimulated gene (ISG) more than two decades ago, is located on chromosome 1, comprise 812bp that encodes three splice variants of 130-138 amino acids with a molecular weight of approximately 13KDa [166 167]. The protein structure of IFI6 is sequentially composed of signal peptides in the N-terminus, a hydrophilic region, a transmembrane region, a connecting region, a transmembrane region, and a hydrophilic region [167]. It is primarily localized at the endoplasmic reticulum (ER), and is a key player in the intricate interplay between antiviral defense and regulation of the immune response [168 169].

IFI6 exhibits potent antiviral activity against Hepatitis B/C viruses and flaviviruses (DENV, West Nile, Yellow Fever) by potentially disrupting virus-induced ER membrane invaginations crucial for replication [170]. Several studies have also shown that IFI6 is highly expressed various malignant tumors, including esophageal squamous cell carcinoma (ESCC) patients and ESCC cell lines. High expression of IFI6 in ESCC cells exerts an oncogenic effect while knockdown of IFI6 expression increases the accumulation of reactive oxygen species, which leads to inhibition of the proliferation of cancer cells and induction of apoptosis[169]. Mechanistically, it has been reported that the anti-viral and tumor-promoting functions of IFI6 are supported by its capacity to antagonize intrinsic apoptosis by IFNs and tumor necrosis factor-related apoptosis-inducing ligand [171 172], or blocking the mitochondrial release of cytochrome c [172] and stabilizing mitochondrial membrane potential [173].

Recent work has shown that IFI6 functions as a negative regulator of innate immunity[174]. During infections with Influenza A virus, SARS-CoV-2, Sendai virus, or poly(I:C) transfection, IFI6 downregulates the expression of interferon (IFN), interferon-stimulated genes (ISGs), and pro-inflammatory cytokines, possibly through interaction with RIG-I, a sensor of viral infection, and modulation of its RNA binding activity [174]. Interestingly, IFI6 is transcriptionally activated by X-rays and other DNA-damaging agents, including chemotherapy [175 176].

Our working hypothesis proposes that IFI6 activation by DNA damage is a protective response to chemotherapy. Chemotherapy-induced DNA damage leads to the accumulation of cytoplasmic DNA fragments (micronuclei and ds/ssDNA) that activate cGAS, a cytosolic DNA sensor. Activated cGAS synthesize cGAMP from GTP and ATP, which acts as a second messenger to activate a signaling cascade involving STING, TBK1 kinase, and transcription factors IRF3 and NF-κB, ultimately leading to IFN and cytokine expression [177].

IFI6 might prevent excessive activation of interferon/cytokine production upon chemotherapy, which is detrimental for stem and differentiated cells. It is demonstrated that the DNA-damage-response-induced IFNbeta promotes cell senescence/apoptosis of differentiated cells and that IFN per se contributes to stem cell decline and premature aging. We hypothesize that IFI6 positioned at the ER, might antagonize this IFN signaling pathway by directly interacting with and inhibiting cGAS or STING, thereby preventing excessive interferon/cytokine activation detrimental to both stem and differentiated cells. This function of IFI6 as an interferon antagonist might be a protective mechanism against senescence or apoptosis triggered by DNA damage-induced IFN-β, as IFN has been shown to contribute to stem cell decline and premature aging [178]. Therefore, genetic targeting of IFI6 by shRNAs could potentially "restore" the excessive activation of the cGAS-STING pathway, NF-κB, and IFN/cytokine expression in blasts during chemotherapy, promoting cell death of both differentiated and stem cells.

To preliminarily test this hypothesis, I tested whether therapeutic activation of the interferon signaling pathway (using cGAMP) might prevent the occurrence of chemoresistance and offer a strategy to prevent the emergence of chemoresistance upon standard treatments in AMLs. Preliminary data (obtained in AMLIEO20) confirmed this hypothesis. Indeed, the double treatment with cGAMP plus *"5+3"* chemotherapy regimen increased chemo-sensitivity of AML blasts. In the three weeks post-therapy, the PB % of human blasts continued to significantly decrease compared to the non-treated controls and to the single cGAMP treatment and *"5+3"* only experimental groups.

To identify an *in vitro* model system to study mechanisms of IFI6 chemo-sensitization, I investigated whether silencing of IFI6 impact the chemosensitivity of established myeloid cell lines to treatment with AraC or Doxorubicin. I conducted *in vitro* experiments, using AML cell lines that have a high IFI6 mRNA expression level (namely U937 and GDM1). I demonstrated by IC50 experiments, that the downregulation of IFI6 significantly enhance chemosensitivity to AraC and Doxorubicin of shIFI6-expressing cells

compared to the shSCR infected controls. Moreover, the knockdown of IFI6 expression in both cell lines does not affect cell proliferation and growth.

Using these cell lines, I performed high-resolution immunofluorescence experiments, setting up the conditions of antibody staining to visualize IFI6 in situ, prior and after chemotherapy, as well as components of the STING pathways. Preliminary results showed that, prior to chemotherapy, both IFI6 and STING partially co-localize at the ER. However, upon chemotherapy treatment, we observed a significant upregulation of both proteins. Moreover, a striking shift in IFI6 localization occurred, with the majority of the protein redistributing in close proximity to STING to the ERGIC compartment, where STING activation takes place [179–182]. This experiment is still under detailed analyses.

In conclusion, I have obtained preliminary results suggesting that IFI6 is a chemotherapy target in AMLs and may be involved in the establishment of therapy resistance by interfering with STING activation. I have recently initiated a series of experiments to further validate this hypothesis. Specifically: i) I have generated scRNAseq and bulk-RNAseq datasets of AML cells expressing or not shIFI6 (using cell lines *in vitro* and my PDX AMLs *in vivo*), treated or not with chemotherapy, to investigate if and to what extent IFI6-silencing increases IFN signaling. In the same experiment, I will characterize biologically and transcriptionally the type of cell death induced by IFI6-silencing; ii) I will analyze whether the ability of IFI6-silencing to revert the chemoresistance phenotype is indeed due to STING activation, investigating if STING-antagonists are capable of reverting the phenotype of IFI6-silencing; iii) I will investigate the type of interaction(s) between IFI6 and STING. In this regard, I will preliminarily analyze the possibility that STING and IFI6 are part of the same molecular complexes, by analyzing the presence of the two proteins within the same high-molecular weight intracellular complexes, using size-exclusion chromatography gradients and in situ proximity ligation experiments.

To start addressing the working principles of IFI6, we tested the prediction that IFI6 forms complexes with components of the STING/cGAS pathway using the algorithm AlphaFold3 [183] (in collaboration with Dr. Marina Mapelli; IEO). No significative 3D prediction could be obtained between IFI6 and cGAS, in the presence or absence of DNA, indicating that most likely IFI6 does not act at this level. However, IFI6 was predicted to form a complex with monomeric STING with relatively good confidence. Previous data showed that upon binding to cGAMP STING forms a homodimer, in which the cGAMP

ligand fits in a pocket organized at the protomer interface and capped by two symmetrical beta-hairpin. Notably, AlphaFold3 predicts the dimeric arrangement of STING also in the absence of the ligand. IFI6 is an extended 136 residue protein with helical propensity. In the computationally predicted model of the IFI6: STING interaction, the IFI6 helix spanning residues 71-91 faces the STING helices 1-14 and 110-120, which form the cGAMP binding pocket. Thus, in this arrangement, IFI6 would prevent the binding of cGAMP to STING by steric hindrance, in this way interfering with the activation of downstream effectors.

The ultimate goal of my studies is to decipher the mechanisms of chemoresistance in AMLs in order to identify strategies that can prevent the establishment of therapy resistance in this disease. Hopefully, understanding the molecular mechanisms by which IFI6 protects AML cells from chemotherapy-induced IFN activation and cell-death, possibly via inhibiting STING, could provide knowledge for the design of specific therapeutic approaches.

REFERENCES

1. De Kouchkovsky, I. & Abdul-Hay, M. 'Acute myeloid leukemia: a comprehensive review and 2016 update'. *Blood Cancer J* 6, e441–e441 (2016).
2. Ferlay, J. *et al.* Cancer incidence and mortality patterns in Europe: Estimates for 40 countries in 2012. *Eur J Cancer* 49, 1374–1403 (2013).
3. Foreman, K. J. *et al.* Forecasting life expectancy, years of life lost, and all-cause and cause-specific mortality for 250 causes of death: reference and alternative scenarios for 2016–40 for 195 countries and territories. *The Lancet* 392, 2052–2090 (2018).
4. Siegel, R. L., Miller, K. D., Fuchs, H. E. & Jemal, A. Cancer Statistics, 2021. *CA Cancer J Clin* 71, 7–33 (2021).
5. Yi, M. *et al.* The global burden and attributable risk factor analysis of acute myeloid leukemia in 195 countries and territories from 1990 to 2017: estimates based on the global burden of disease study 2017. *J Hematol Oncol* 13, 72 (2020).
6. Thol, F. & Ganser, A. Treatment of Relapsed Acute Myeloid Leukemia. *Curr Treat Options Oncol* 21, 66 (2020).
7. Arber, D. A. *et al.* The 2016 revision to the World Health Organization classification of myeloid neoplasms and acute leukemia. *Blood* 127, 2391–2405 (2016).
8. Arber, D. A. *et al.* International Consensus Classification of Myeloid Neoplasms and Acute Leukemias: integrating morphologic, clinical, and genomic data. *Blood* 140, 1200–1228 (2022).
9. Khoury, J. D. *et al.* The 5th edition of the World Health Organization Classification of Haematolymphoid Tumours: Myeloid and Histiocytic/Dendritic Neoplasms. *Leukemia* 36, 1703–1719 (2022).
10. Döhner, H. *et al.* Diagnosis and management of AML in adults: 2022 recommendations from an international expert panel on behalf of the ELN. *Blood* 140, 1345–1377 (2022).
11. Voso, M. T., De Bellis, E. & Ottone, T. Diagnosis and Classification of AML: WHO 2016. in 23–54 (2021). doi:10.1007/978-3-030-72676-8_2.
12. Döhner, H. *et al.* Diagnosis and management of AML in adults: 2022 recommendations from an international expert panel on behalf of the ELN. *Blood* 140, 1345–1377 (2022).
13. Morita, K. *et al.* Clonal evolution of acute myeloid leukemia revealed by high-throughput single-cell genomics. *Nat Commun* 11, 5327 (2020).
14. Miles, L. A. *et al.* Single-cell mutation analysis of clonal evolution in myeloid malignancies. *Nature* 587, 477–482 (2020).
15. Ding, L. *et al.* Clonal evolution in relapsed acute myeloid leukaemia revealed by whole-genome sequencing. *Nature* 481, 506–510 (2012).
16. Estey, E. & Döhner, H. Acute myeloid leukaemia. *The Lancet* 368, 1894–1907 (2006).
17. Döhner, H., Weisdorf, D. J. & Bloomfield, C. D. Acute Myeloid Leukemia. *New England Journal of Medicine* 373, 1136–1152 (2015).
18. Döhner, H. *et al.* Diagnosis and management of AML in adults: 2017 ELN recommendations from an international expert panel. *Blood* 129, 424–447 (2017).
19. Stone, R. M. *et al.* Midostaurin plus Chemotherapy for Acute Myeloid Leukemia with a FLT3 Mutation. *New England Journal of Medicine* 377, 454–464 (2017).
20. Stein, E. M. *et al.* Updated Survival and Response Analyses from a Phase 1 Study of Ivosidenib or Enasidenib Combined with Induction and Consolidation Chemotherapy in Patients with Newly Diagnosed AML with an IDH1 or IDH2 Mutation. *Blood* 138, 1276–1276 (2021).

21. Lancet, J. E. *et al.* CPX-351 (cytarabine and daunorubicin) Liposome for Injection Versus Conventional Cytarabine Plus Daunorubicin in Older Patients With Newly Diagnosed Secondary Acute Myeloid Leukemia. *Journal of Clinical Oncology* 36, 2684–2692 (2018).
22. van der Velden, V. H. J. *et al.* Targeting of the CD33-calicheamicin immunoconjugate Mylotarg (CMA-676) in acute myeloid leukemia: in vivo and in vitro saturation and internalization by leukemic and normal myeloid cells. *Blood* 97, 3197–3204 (2001).
23. Tallman, M. S. *et al.* Acute Myeloid Leukemia, Version 3.2019, NCCN Clinical Practice Guidelines in Oncology. *Journal of the National Comprehensive Cancer Network* 17, 721–749 (2019).
24. Griffioen, M. S., de Leeuw, D. C., Janssen, J. J. W. M. & Smit, L. Targeting Acute Myeloid Leukemia with Venetoclax; Biomarkers for Sensitivity and Rationale for Venetoclax-Based Combination Therapies. *Cancers (Basel)* 14, (2022).
25. DiNardo, C. D. *et al.* Azacitidine and Venetoclax in Previously Untreated Acute Myeloid Leukemia. *New England Journal of Medicine* 383, 617–629 (2020).
26. MacPherson, L. & Dawson, M. A. Survival of the Fittest: Darwinian Selection Underpins Chemotherapy Resistance in AML. *Cell Stem Cell* 21, 291–292 (2017).
27. Shlush, L. I. *et al.* Tracing the origins of relapse in acute myeloid leukaemia to stem cells. *Nature* 547, 104–108 (2017).
28. Vitale, I., Shema, E., Loi, S. & Galluzzi, L. Intratumoral heterogeneity in cancer progression and response to immunotherapy. *Nat Med* 27, 212–224 (2021).
29. Bonnet, D. & Dick, J. E. Human acute myeloid leukemia is organized as a hierarchy that originates from a primitive hematopoietic cell. *Nat Med* 3, 730–737 (1997).
30. Ishikawa, F. *et al.* Chemotherapy-resistant human AML stem cells home to and engraft within the bone-marrow endosteal region. *Nat Biotechnol* 25, 1315–1321 (2007).
31. Saito, Y. *et al.* Induction of cell cycle entry eliminates human leukemia stem cells in a mouse model of AML. *Nat Biotechnol* 28, 275–280 (2010).
32. Döhner, H. *et al.* Diagnosis and management of acute myeloid leukemia in adults: recommendations from an international expert panel, on behalf of the European LeukemiaNet. *Blood* 115, 453–474 (2010).
33. Bullinger, L., Döhner, K. & Döhner, H. Genomics of Acute Myeloid Leukemia Diagnosis and Pathways. *Journal of Clinical Oncology* 35, 934–946 (2017).
34. Hangauer, M. J. *et al.* Drug-tolerant persister cancer cells are vulnerable to GPX4 inhibition. *Nature* 551, 247–250 (2017).
35. Sharma, V., Dixit, D., Koul, N., Mehta, V. S. & Sen, E. Ras regulates interleukin-1β-induced HIF-1α transcriptional activity in glioblastoma. *J Mol Med* 89, 123–136 (2011).
36. Liau, B. B. *et al.* Adaptive Chromatin Remodeling Drives Glioblastoma Stem Cell Plasticity and Drug Tolerance. *Cell Stem Cell* 20, 233-246.e7 (2017).
37. Boyd, A. L. *et al.* Identification of Chemotherapy-Induced Leukemic-Regenerating Cells Reveals a Transient Vulnerability of Human AML Recurrence. *Cancer Cell* 34, 483-498.e5 (2018).
38. Duy, C. *et al.* Chemotherapy Induces Senescence-Like Resilient Cells Capable of Initiating AML Recurrence. *Cancer Discov* 11, 1542–1561 (2021).
39. Farge, T. *et al.* Chemotherapy-Resistant Human Acute Myeloid Leukemia Cells Are Not Enriched for Leukemic Stem Cells but Require Oxidative Metabolism. *Cancer Discov* 7, 716–735 (2017).
40. Ho, T.-C. *et al.* Evolution of acute myelogenous leukemia stem cell properties after treatment and progression. *Blood* 128, 1671–1678 (2016).

41. Genomic and Epigenomic Landscapes of Adult De Novo Acute Myeloid Leukemia. *New England Journal of Medicine* 368, 2059–2074 (2013).
42. Jan, M. *et al.* Clonal Evolution of Preleukemic Hematopoietic Stem Cells Precedes Human Acute Myeloid Leukemia. *Sci Transl Med* 4, (2012).
43. Krönke, J. *et al.* Clonal evolution in relapsed NPM1-mutated acute myeloid leukemia. *Blood* 122, 100–108 (2013).
44. Shlush, L. I. *et al.* Identification of pre-leukaemic haematopoietic stem cells in acute leukaemia. *Nature* 506, 328–333 (2014).
45. Ding, L. *et al.* Clonal evolution in relapsed acute myeloid leukaemia revealed by whole-genome sequencing. *Nature* 481, 506–510 (2012).
46. Saeed, B. R. *et al.* Analysis of nonleukemic cellular subcompartments reconstructs clonal evolution of acute myeloid leukemia and identifies therapy-resistant preleukemic clones. *Int J Cancer* 148, 2825–2838 (2021).
47. Figueroa, M. E. *et al.* DNA Methylation Signatures Identify Biologically Distinct Subtypes in Acute Myeloid Leukemia. *Cancer Cell* 17, 13–27 (2010).
48. Landau, D. A. *et al.* Locally Disordered Methylation Forms the Basis of Intratumor Methylome Variation in Chronic Lymphocytic Leukemia. *Cancer Cell* 26, 813–825 (2014).
49. Li, S. *et al.* Distinct evolution and dynamics of epigenetic and genetic heterogeneity in acute myeloid leukemia. *Nat Med* 22, 792–799 (2016).
50. Ho, T.-C. *et al.* Evolution of acute myelogenous leukemia stem cell properties after treatment and progression. *Blood* 128, 1671–1678 (2016).
51. Ng, S. W. K. *et al.* A 17-gene stemness score for rapid determination of risk in acute leukaemia. *Nature* 540, 433–437 (2016).
52. van Galen, P. *et al.* Single-Cell RNA-Seq Reveals AML Hierarchies Relevant to Disease Progression and Immunity. *Cell* 176, 1265-1281.e24 (2019).
53. Saito, Y. *et al.* Identification of Therapeutic Targets for Quiescent, Chemotherapy-Resistant Human Leukemia Stem Cells. *Sci Transl Med* 2, (2010).
54. Fujita, S. *et al.* Dual inhibition of EZH1/2 breaks the quiescence of leukemia stem cells in acute myeloid leukemia. *Leukemia* 32, 855–864 (2018).
55. Behbehani, G. K. *et al.* Mass Cytometric Functional Profiling of Acute Myeloid Leukemia Defines Cell-Cycle and Immunophenotypic Properties That Correlate with Known Responses to Therapy. *Cancer Discov* 5, 988–1003 (2015).
56. Wang, W. *et al.* Mesenchymal stromal cells contribute to quiescence of therapy-resistant leukemic cells in acute myeloid leukemia. *Eur J Haematol* 99, 392–398 (2017).
57. Yilmaz, M. *et al.* Late relapse in acute myeloid leukemia (AML): clonal evolution or therapy-related leukemia? *Blood Cancer J* 9, 7 (2019).
58. Ciciarello, M. *et al.* The Yin and Yang of the Bone Marrow Microenvironment: Pros and Cons of Mesenchymal Stromal Cells in Acute Myeloid Leukemia. *Front Oncol* 9, (2019).
59. O'Reilly, E., Zeinabad, H. A. & Szegezdi, E. Hematopoietic versus leukemic stem cell quiescence: Challenges and therapeutic opportunities. *Blood Rev* 50, 100850 (2021).
60. Duarte, D. *et al.* Inhibition of Endosteal Vascular Niche Remodeling Rescues Hematopoietic Stem Cell Loss in AML. *Cell Stem Cell* 22, 64-77.e6 (2018).
61. Cogle, C. R. *et al.* Acute myeloid leukemia in the vascular niche. *Cancer Lett* 380, 552–560 (2016).
62. Guezguez, B. *et al.* Regional Localization within the Bone Marrow Influences the Functional Capacity of Human HSCs. *Cell Stem Cell* 13, 175–189 (2013).
63. Kunisaki, Y. *et al.* Arteriolar niches maintain haematopoietic stem cell quiescence. *Nature* 502, 637–643 (2013).

64. Bhatia, M., Wang, J. C. Y., Kapp, U., Bonnet, D. & Dick, J. E. Purification of primitive human hematopoietic cells capable of repopulating immune-deficient mice. *Proc Natl Acad Sci U S A* 94, 5320–5325 (1997).
65. Bhatia, M., Bonnet, D., Murdoch, B., Gan, O. I. & Dick, J. E. A newly discovered class of human hematopoietic cells with SCID- repopulating activity. *Nat Med* 4, 1038–1045 (1998).
66. Kollet, O. *et al.* β2 microglobulin-deficient (B2m(null)) NOD/SCID mice are excellent recipients for studying human stem cell function. *Blood* 95, 3102–3105 (2000).
67. Glimm, H. *et al.* Previously undetected human hematopoietic cell populations with short-term repopulating activity selectively engraft NOD/SCID-β2 microglobulin-null mice. *Journal of Clinical Investigation* 107, 199–206 (2001).
68. Burnett, A. K. *et al.* Identification of Patients with Acute Myeloblastic Leukemia Who Benefit from the Addition of Gemtuzumab Ozogamicin: Results of the MRC AML15 Trial. *Journal of Clinical Oncology* 29, 369–377 (2011).
69. Yilmaz, M. *et al.* Late relapse in acute myeloid leukemia (AML): clonal evolution or therapy-related leukemia? *Blood Cancer J* 9, 3–8 (2019).
70. Jordan, C. T. & Guzman, M. L. Mechanisms controlling pathogenesis and survival of leukemic stem cells. *Oncogene* 23, 7178–7187 (2004).
71. Thomas, D. & Majeti, R. Biology and relevance of human acute myeloid leukemia stem cells. *Blood* 129, 1577–1585 (2017).
72. Loh, J.-J. & Ma, S. Hallmarks of cancer stemness. *Cell Stem Cell* 31, 617–639 (2024).
73. Bonnet, D. & Dick, J. E. Human acute myeloid leukemia is organized as a hierarchy that originates from a primitive hematopoietic cell. *Nat Med* 3, 730–7 (1997).
74. Lapidot, T. *et al.* A cell initiating human acute myeloid leukaemia after transplantation into SCID mice. *Nature* 367, 645–8 (1994).
75. Dick, J. E. & Bonnet, D. Human Acute Myeloid Leukaemia is organised as a heirarchy that originates from a primitive haematopoetic cell. *Nat Med* 3, 730–737 (1997).
76. Yanagisawa, B., Ghiaur, G., Smith, B. D. & Jones, R. J. Translating leukemia stem cells into the clinical setting: Harmonizing the heterogeneity. *Exp Hematol* 44, 1130–1137 (2016).
77. Ho, T. C. *et al.* Evolution of acute myelogenous leukemia stem cell properties after treatment and progression. *Blood* 128, 1671–1678 (2016).
78. Hackl, H. *et al.* A gene expression profile associated with relapse of cytogenetically normal acute myeloid leukemia is enriched for leukemia stem cell genes. *Leuk Lymphoma* 56, 1126–1128 (2015).
79. Al-Hajj, M., Wicha, M. S., Benito-Hernandez, A., Morrison, S. J. & Clarke, M. F. Prospective identification of tumorigenic breast cancer cells. *Proc Natl Acad Sci U S A* 100, 3983–8 (2003).
80. Singh, S. K. *et al.* Identification of human brain tumour initiating cells. *Nature* 432, 396–401 (2004).
81. O'Brien, C. A., Pollett, A., Gallinger, S. & Dick, J. E. A human colon cancer cell capable of initiating tumour growth in immunodeficient mice. *Nature* 445, 106–10 (2007).
82. Recasens, A. & Munoz, L. Targeting Cancer Cell Dormancy. *Trends Pharmacol Sci* 40, 128–141 (2019).
83. Hangauer, M. J. *et al.* Drug-tolerant persister cancer cells are vulnerable to GPX4 inhibition. *Nature* 551, 247–250 (2017).
84. Liau, B. B. *et al.* Adaptive Chromatin Remodeling Drives Glioblastoma Stem Cell Plasticity and Drug Tolerance. *Cell Stem Cell* 20, 233-246.e7 (2017).

85. Sharma, V., Dixit, D., Koul, N., Mehta, V. S. & Sen, E. Ras regulates interleukin-1β-induced HIF-1α transcriptional activity in glioblastoma. *J Mol Med* 89, 123–136 (2011).
86. Chang, B. D. *et al.* A senescence-like phenotype distinguishes tumor cells that undergo terminal proliferation arrest after exposure to anticancer agents. *Cancer Res* 59, 3761–3767 (1999).
87. te Poele, R. H., Okorokov, A. L., Jardine, L., Cummings, J. & Joel, S. P. DNA damage is able to induce senescence in tumor cells in vitro and in vivo. *Cancer Res* 62, 1876–1883 (2002).
88. Gorgoulis, V. *et al.* Cellular Senescence: Defining a Path Forward. *Cell* 179, 813–827 (2019).
89. Duy, C. *et al.* Chemotherapy induces senescence-like resilient cells capable of initiating aml recurrence. *Cancer Discov* 11, 1542–1561 (2021).
90. Lopes, F. L., Desmarais, J. A. & Murphy, B. D. Embryonic diapause and its regulation. *Reproduction* 128, 669–678 (2004).
91. Fenelon, J. C. & Renfree, M. B. The history of the discovery of embryonic diapause in mammals. *Biol Reprod* 99, 242–251 (2018).
92. Renfree, M. B. & Fenelon, J. C. The enigma of embryonic diapause. *Development (Cambridge)* 144, 3199–3210 (2017).
93. Rehman, S. K. *et al.* Colorectal Cancer Cells Enter a Diapause-like DTP State to Survive Chemotherapy. *Cell* 184, 226-242.e21 (2021).
94. Farge, T. *et al.* HHS Public Access. 7, 716–735 (2018).
95. Yan, H. *et al.* Association of a cytarabine chemosensitivity related gene expression signature with survival in cytogenetically normal acute myeloid leukemia. *Oncotarget* 8, 1529–1540 (2017).
96. Baccelli, I. *et al.* Mubritinib Targets the Electron Transport Chain Complex I and Reveals the Landscape of OXPHOS Dependency in Acute Myeloid Leukemia. *Cancer Cell* 36, 84-99.e8 (2019).
97. Kreitz, J. *et al.* Metabolic Plasticity of Acute Myeloid Leukemia. *Cells* 8, 805 (2019).
98. Stetson, L. C. *et al.* Single cell RNA sequencing of AML initiating cells reveals RNA-based evolution during disease progression. *Leukemia* 35, 2799–2812 (2021).
99. Bonen, A. *et al.* Regulation of fatty acid transport by fatty acid translocase/CD36. *Proceedings of the Nutrition Society* 63, 245–249 (2004).
100. Schweikhard, E. S. & Ziegler, C. M. Amino Acid Secondary Transporters. in 1–28 (2012). doi:10.1016/B978-0-12-394316-3.00001-6.
101. Sabath, D. E. Minimal Residual Disease. *Brenner's Encyclopedia of Genetics: Second Edition* 9, 417–419 (2013).
102. Fathi, N., Rashidi, G., Khodadadi, A., Shahi, S. & Sharifi, S. STAT3 and apoptosis challenges in cancer. *Int J Biol Macromol* 117, 993–1001 (2018).
103. Redell, M. S., Ruiz, M. J., Alonzo, T. A., Gerbing, R. B. & Tweardy, D. J. Stat3 signaling in acute myeloid leukemia: Ligand-dependent and -independent activation and induction of apoptosis by a novel small-molecule Stat3 inhibitor. *Blood* 117, 5701–5709 (2011).
104. Erbani, J., Tay, J., Barbier, V., Levesque, J. P. & Winkler, I. G. Acute Myeloid Leukemia Chemo-Resistance Is Mediated by E-selectin Receptor CD162 in Bone Marrow Niches. *Front Cell Dev Biol* 8, 1–16 (2020).
105. Martini, M. *et al.* IFN-gamma-mediated upmodulation of MHC class I expression activates tumor-specific immune response in a mouse model of prostate cancer. *Vaccine* 28, 3548–57 (2010).
106. Young, H. A. & Hardy, K. J. Role of interferon-gamma in immune cell regulation. *J Leukoc Biol* 58, 373–81 (1995).

107. Bach, E. A., Aguet, M. & Schreiber, R. D. The IFN gamma receptor: a paradigm for cytokine receptor signaling. *Annu Rev Immunol* 15, 563–91 (1997).
108. Vigneron, N. Human Tumor Antigens and Cancer Immunotherapy. *Biomed Res Int* 2015, 1–17 (2015).
109. Chin, Y. E. *et al.* Cell growth arrest and induction of cyclin-dependent kinase inhibitor p21 WAF1/CIP1 mediated by STAT1. *Science* 272, 719–22 (1996).
110. Chawla-Sarkar, M. *et al.* Apoptosis and interferons: role of interferon-stimulated genes as mediators of apoptosis. *Apoptosis* 8, 237–49 (2003).
111. Zaidi, M. R. & Merlino, G. The two faces of interferon-γ in cancer. *Clin Cancer Res* 17, 6118–24 (2011).
112. Maeurer, M. J., Martin, D., Elder, E., Storkus, W. J. & Lotze, M. T. Detection of naturally processed and HLA-A1-presented melanoma T-cell epitopes defined by CD8(+) T-cells' release of granulocyte-macrophage colony-stimulating factor but not by cytolysis. *Clin Cancer Res* 2, 87–95 (1996).
113. Algarra, I., García-Lora, A., Cabrera, T., Ruiz-Cabello, F. & Garrido, F. The selection of tumor variants with altered expression of classical and nonclassical MHC class I molecules: implications for tumor immune escape. *Cancer Immunol Immunother* 53, 904–10 (2004).
114. Beatty, G. L. & Paterson, Y. IFN-gamma can promote tumor evasion of the immune system in vivo by down-regulating cellular levels of an endogenous tumor antigen. *J Immunol* 165, 5502–8 (2000).
115. Le Poole, I. C. *et al.* Interferon-gamma reduces melanosomal antigen expression and recognition of melanoma cells by cytotoxic T cells. *Am J Pathol* 160, 521–8 (2002).
116. Kursunel, M. A. & Esendagli, G. The untold story of IFN-γ in cancer biology. *Cytokine Growth Factor Rev* 31, 73–81 (2016).
117. Mojic, M., Takeda, K. & Hayakawa, Y. The Dark Side of IFN-γ: Its Role in Promoting Cancer Immunoevasion. *Int J Mol Sci* 19, (2017).
118. Aqbi, H. F., Wallace, M., Sappal, S., Payne, K. K. & Manjili, M. H. IFN-γ orchestrates tumor elimination, tumor dormancy, tumor escape, and progression. *J Leukoc Biol* 103, 1219–1223 (2018).
119. Castro, F., Cardoso, A. P., Gonçalves, R. M., Serre, K. & Oliveira, M. J. Interferon-Gamma at the Crossroads of Tumor Immune Surveillance or Evasion. *Front Immunol* 9, 847 (2018).
120. Kosmidis, C. *et al.* Interferon-γ and Colorectal Cancer: an up-to date. *J Cancer* 9, 232–238 (2018).
121. Bonnet, D. & Dick, J. E. Human acute myeloid leukemia is organized as a hierarchy that originates from a primitive hematopoietic cell. *Nat Med* 3, 730–737 (1997).
122. Thomas, D. & Majeti, R. Biology and relevance of human acute myeloid leukemia stem cells. *Blood* 129, 1577–1585 (2017).
123. Jordan, C. T., Guzman, M. L. & Noble, M. Cancer Stem Cells. *New England Journal of Medicine* 355, 1253–1261 (2006).
124. Eppert, K. *et al.* Stem cell gene expression programs influence clinical outcome in human leukemia. *Nat Med* 17, 1086–1093 (2011).
125. Shlush, L. I. *et al.* Tracing the origins of relapse in acute myeloid leukaemia to stem cells. *Nature* 547, 104–108 (2017).
126. Boyd, A. L. *et al.* Identification of Chemotherapy-Induced Leukemic-Regenerating Cells Reveals a Transient Vulnerability of Human AML Recurrence. *Cancer Cell* 34, 483-498.e5 (2018).
127. Farge, T. *et al.* Chemotherapy-Resistant Human Acute Myeloid Leukemia Cells Are Not Enriched for Leukemic Stem Cells but Require Oxidative Metabolism. *Cancer Discov* 7, 716–735 (2017).

128. Duy, C. *et al.* Chemotherapy Induces Senescence-Like Resilient Cells Capable of Initiating AML Recurrence. *Cancer Discov* 11, 1542–1561 (2021).
129. Dhimolea, E. *et al.* An Embryonic Diapause-like Adaptation with Suppressed Myc Activity Enables Tumor Treatment Persistence. *Cancer Cell* 39, 240-256.e11 (2021).
130. Bell, C. C. *et al.* Targeting enhancer switching overcomes non-genetic drug resistance in acute myeloid leukaemia. *Nat Commun* 10, 2723 (2019).
131. Raha, D. *et al.* The Cancer Stem Cell Marker Aldehyde Dehydrogenase Is Required to Maintain a Drug-Tolerant Tumor Cell Subpopulation. *Cancer Res* 74, 3579–3590 (2014).
132. Liau, B. B. *et al.* Adaptive Chromatin Remodeling Drives Glioblastoma Stem Cell Plasticity and Drug Tolerance. *Cell Stem Cell* 20, 233-246.e7 (2017).
133. Oren, Y. *et al.* Cycling cancer persister cells arise from lineages with distinct programs. *Nature* 596, 576–582 (2021).
134. Hangauer, M. J. *et al.* Drug-tolerant persister cancer cells are vulnerable to GPX4 inhibition. *Nature* 551, 247–250 (2017).
135. Uckelmann, H. J., Armstrong, S. A. & Stone, R. M. Location, Location, Location: Mutant NPM1c Cytoplasmic Localization Is Required to Maintain Stem Cell Genes in AML. *Cancer Cell* 34, 355–357 (2018).
136. Vlachou, T., Nobile, M. S., Ronchini, C., Besozzi, D. & Pelicci, P. G. An Experimental and Computational Protocol to Study Cell Proliferation in Human Acute Myeloid Leukemia Xenografts. in 241–258 (2021). doi:10.1007/978-1-0716-0810-4_14.
137. Nobile, M. S. *et al.* Modeling cell proliferation in human acute myeloid leukemia xenografts. *Bioinformatics* 35, 3378–3386 (2019).
138. Ravandi, F. *et al.* Salvage Therapy Outcomes in a Historical Cohort of Patients With Relapsed or Refractory Acute Myeloid Leukemia. *Clin Lymphoma Myeloma Leuk* 20, e871–e882 (2020).
139. Ding, L. *et al.* Clonal evolution in relapsed acute myeloid leukaemia revealed by whole-genome sequencing. *Nature* 481, 506–510 (2012).
140. Garg, M. *et al.* Profiling of somatic mutations in acute myeloid leukemia with FLT3-ITD at diagnosis and relapse. *Blood* 126, 2491–2501 (2015).
141. Li, S. *et al.* Distinct evolution and dynamics of epigenetic and genetic heterogeneity in acute myeloid leukemia. *Nat Med* 22, 792–799 (2016).
142. Chen, L., Li, S. & McGilvray, I. The ISG15/USP18 ubiquitin-like pathway (ISGylation system) in Hepatitis C Virus infection and resistance to interferon therapy. *Int J Biochem Cell Biol* 43, 1427–1431 (2011).
143. Liang, R., Li, X. & Zhu, X. Deciphering the Roles of IFITM1 in Tumors. *Mol Diagn Ther* 24, 433–441 (2020).
144. Yang, C. *et al.* Interferon alpha (IFNα)-induced TRIM22 interrupts HCV replication by ubiquitinating NS5A. *Cell Mol Immunol* 13, 94–102 (2016).
145. Zu, S. *et al.* TRIM22 suppresses Zika virus replication by targeting NS1 and NS3 for proteasomal degradation. *Cell Biosci* 12, 139 (2022).
146. Inoue, A., Watanabe, M., Kondo, T., Hirano, S. & Hatakeyama, S. TRIM22 negatively regulates MHC-II expression. *Biochim Biophys Acta Mol Cell Res* 1869, 119318 (2022).
147. Sajid, M. *et al.* The Functional and Antiviral Activity of Interferon Alpha-Inducible IFI6 Against Hepatitis B Virus Replication and Gene Expression. *Front Immunol* 12, 634937 (2021).
148. Cheriyath, V. *et al.* G1P3, an IFN-induced survival factor, antagonizes TRAIL-induced apoptosis in human myeloma cells. *J Clin Invest* 117, 3107–17 (2007).

149. Parker, N. & Porter, A. C. G. Identification of a novel gene family that includes the interferon-inducible human genes 6-16 and ISG12. *BMC Genomics* 5, 8 (2004).
150. Richardson, R. B. *et al.* A CRISPR screen identifies IFI6 as an ER-resident interferon effector that blocks flavivirus replication. *Nat Microbiol* 3, 1214–1223 (2018).
151. Meyer, K. *et al.* Interferon-α inducible protein 6 impairs EGFR activation by CD81 and inhibits hepatitis C virus infection. *Sci Rep* 5, 9012 (2015).
152. Sajid, M. *et al.* The Functional and Antiviral Activity of Interferon Alpha-Inducible IFI6 Against Hepatitis B Virus Replication and Gene Expression. *Front Immunol* 12, 634937 (2021).
153. Qi, Y. *et al.* IFI6 Inhibits Apoptosis via Mitochondrial-Dependent Pathway in Dengue Virus 2 Infected Vascular Endothelial Cells. *PLoS One* 10, e0132743 (2015).
154. Villamayor, L. *et al.* Interferon alpha inducible protein 6 is a negative regulator of innate immune responses by modulating RIG-I activation. *Front Immunol* 14, 1105309 (2023).
155. Jia, H. *et al.* Interferon-α inducible protein 6 (IFI6) confers protection against ionizing radiation in skin cells. *J Dermatol Sci* 100, 139–147 (2020).
156. Ramanjulu, J. M. *et al.* Design of amidobenzimidazole STING receptor agonists with systemic activity. *Nature* 564, 439–443 (2018).
157. Diaz Jr, L. A. *et al.* The molecular evolution of acquired resistance to targeted EGFR blockade in colorectal cancers. *Nature* 486, 537–540 (2012).
158. Hou, Y. *et al.* Single-Cell Exome Sequencing and Monoclonal Evolution of a JAK2-Negative Myeloproliferative Neoplasm. *Cell* 148, 873–885 (2012).
159. Cicalese, A. *et al.* The Tumor Suppressor p53 Regulates Polarity of Self-Renewing Divisions in Mammary Stem Cells. *Cell* 138, 1083–1095 (2009).
160. Marjanovic, N. D., Weinberg, R. A. & Chaffer, C. L. Cell Plasticity and Heterogeneity in Cancer. *Clin Chem* 59, 168–179 (2013).
161. Nguyen, A., Yoshida, M., Goodarzi, H. & Tavazoie, S. F. Highly variable cancer subpopulations that exhibit enhanced transcriptome variability and metastatic fitness. *Nat Commun* 7, 11246 (2016).
162. McGranahan, N. & Swanton, C. Clonal Heterogeneity and Tumor Evolution: Past, Present, and the Future. *Cell* 168, 613–628 (2017).
163. Feinberg, A. P., Koldobskiy, M. A. & Göndör, A. Epigenetic modulators, modifiers and mediators in cancer aetiology and progression. *Nat Rev Genet* 17, 284–299 (2016).
164. Russo, M. *et al.* Cancer drug-tolerant persister cells: from biological questions to clinical opportunities. *Nat Rev Cancer* 24, 694–717 (2024).
165. Montesinos, P. *et al.* Tumor lysis syndrome in patients with acute myeloid leukemia: identification of risk factors and development of a predictive model. *Haematologica* 93, 67–74 (2008).
166. Parker, N. & Porter, A. C. G. Identification of a novel gene family that includes the interferon-inducible human genes 6-16 and ISG12. *BMC Genomics* 5, 8 (2004).
167. Cheriyath, V., Leaman, D. W. & Borden, E. C. Emerging roles of FAM14 family members (G1P3/ISG 6-16 and ISG12/IFI27) in innate immunity and cancer. *J Interferon Cytokine Res* 31, 173–81 (2011).
168. Wan, L. *et al.* Chicken IFI6 inhibits avian reovirus replication and affects related innate immune signaling pathways. *Front Microbiol* 14, (2023).
169. Liu, Z. *et al.* IFI6 depletion inhibits esophageal squamous cell carcinoma progression through reactive oxygen species accumulation via mitochondrial dysfunction and endoplasmic reticulum stress. *Journal of Experimental & Clinical Cancer Research* 39, 144 (2020).

170. Richardson, R. B. *et al.* A CRISPR screen identifies IFI6 as an ER-resident interferon effector that blocks flavivirus replication. *Nat Microbiol* 3, 1214–1223 (2018).
171. Tahara, E. *et al.* G1P3, an interferon inducible gene 6-16, is expressed in gastric cancers and inhibits mitochondrial-mediated apoptosis in gastric cancer cell line TMK-1 cell. *Cancer Immunol Immunother* 54, 729–40 (2005).
172. Cheriyath, V. *et al.* G1P3, an IFN-induced survival factor, antagonizes TRAIL-induced apoptosis in human myeloma cells. *Journal of Clinical Investigation* 117, 3107–3117 (2007).
173. Qi, Y. *et al.* IFI6 Inhibits Apoptosis via Mitochondrial-Dependent Pathway in Dengue Virus 2 Infected Vascular Endothelial Cells. *PLoS One* 10, e0132743 (2015).
174. Villamayor, L. *et al.* Interferon alpha inducible protein 6 is a negative regulator of innate immune responses by modulating RIG-I activation. *Front Immunol* 14, 1105309 (2023).
175. Lu, L.-Y. *et al.* Current utilization of interferon alpha for the treatment of coronavirus disease 2019: A comprehensive review. *Cytokine Growth Factor Rev* 63, 34–43 (2022).
176. Kim, T. *et al.* Activation of Interferon Regulatory Factor 3 in Response to DNA-damaging Agents. *Journal of Biological Chemistry* 274, 30686–30689 (1999).
177. Decout, A., Katz, J. D., Venkatraman, S. & Ablasser, A. The cGAS–STING pathway as a therapeutic target in inflammatory diseases. *Nat Rev Immunol* 21, 548–569 (2021).
178. Yu, Q. *et al.* DNA-Damage-Induced Type I Interferon Promotes Senescence and Inhibits Stem Cell Function. *Cell Rep* 11, 785–797 (2015).
179. Li, L. Stimulating STING for cancer therapy: Taking the extracellular route. *Cell Chem Biol* 31, 851–861 (2024).
180. Zhang, X., Bai, X. & Chen, Z. J. Structures and Mechanisms in the cGAS-STING Innate Immunity Pathway. *Immunity* 53, 43–53 (2020).
181. Zhou, W. *et al.* Structure of the Human cGAS–DNA Complex Reveals Enhanced Control of Immune Surveillance. *Cell* 174, 300-311.e11 (2018).
182. Patel, D. J., Yu, Y. & Xie, W. cGAMP-activated cGAS–STING signaling: its bacterial origins and evolutionary adaptation by metazoans. *Nat Struct Mol Biol* 30, 245–260 (2023).
183. Abramson, J. *et al.* Accurate structure prediction of biomolecular interactions with AlphaFold 3. *Nature* 630, 493–500 (2024).